RICE UNIVERSITY

Collisional Ionization Studies of Rubidium Atoms and Small Halogenated Molecules near Reaction Thresholds

by

Beike Jia

A THESIS SUBMITTED
IN PARTIAL FULFILLMENT OF THE
REQUIREMENTS FOR THE DEGREE

Doctor of Philosophy

APPROVED, THESIS COMMITTEE:

Philip R. Brooks, Professor of Chemistry
Chair

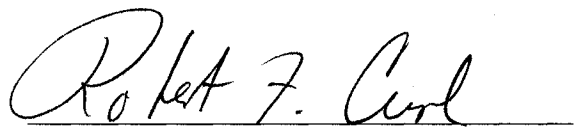

Robert F. Curl, University Professor

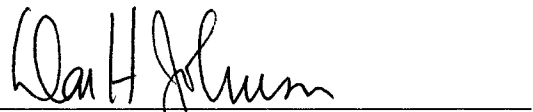

Don H. Johnson, Abercrombie Professor of
Electrical and Computer Engineering

HOUSTON, TEXAS

AUGUST, 2005

Reproduced with permission of the copyright owner. Further reproduction prohibited without permission.

NOTE TO USERS

Page(s) not included in the original manuscript and are unavailable from the author or university. The manuscript was scanned as received.

156

This reproduction is the best copy available.

UMI®

Reproduced with permission of the copyright owner. Further reproduction prohibited without permission.

UMI Number: 3216724

INFORMATION TO USERS

The quality of this reproduction is dependent upon the quality of the copy submitted. Broken or indistinct print, colored or poor quality illustrations and photographs, print bleed-through, substandard margins, and improper alignment can adversely affect reproduction.

In the unlikely event that the author did not send a complete manuscript and there are missing pages, these will be noted. Also, if unauthorized copyright material had to be removed, a note will indicate the deletion.

UMI®

UMI Microform 3216724

Copyright 2006 by ProQuest Information and Learning Company.

All rights reserved. This microform edition is protected against unauthorized copying under Title 17, United States Code.

ProQuest Information and Learning Company
300 North Zeeb Road
P.O. Box 1346
Ann Arbor, MI 48106-1346

Reproduced with permission of the copyright owner. Further reproduction prohibited without permission.

Abstract

Collisional Ionization Studies of Rubidium Atoms and Small Halogenated Molecules near Reaction Thresholds

by

Beike Jia

An atomic supersonic beam of Rb (seeded in H_2) and a gas beam (organic molecules seeded in He or Ar) are crossed to investigate electron transfer reactions close to their energy thresholds, and to measure the electron affinities (EA) of various product negative ions. The ions are collected and identified by coincidence TOF mass spectrometry. The signal from the Rb seeded beam is orders of magnitude higher than that from a Rb charge exchange sources.

Most of the energy comes from the Rb beam. Therefore the speed distribution of this beam is measured by time of flight and the speed of the gas beam estimated from theory. Then the energy distribution for the reaction is calculated.

The coincidence signals of negative ions are analyzed from fundamental kinetic theory with the reaction threshold an unknown parameter in the equation. A computer program fits the experimental data and finds the optimal value of the threshold. The EA's of all negative ions are then calculated by conservation of energy.

C_2F_5Cl, C_2F_5I, C_6F_6, C_2Cl_4, C_2HCl_3, $Cl_2C{=}CH_2$, trans-$C_2H_2Cl_2$ and many other molecules have been explored. The experiments produce various parent negative ions and

Reproduced with permission of the copyright owner. Further reproduction prohibited without permission.

fragments. The initial analysis suggests that C_2F_5 has a surprisingly higher EA than what has been reported in the literature, but we believe this high value is due to the small fraction of Rb dimer. The parent ion of C_2F_5I, which has not been reported previously, is made in this experiment and its EA is determined. For C_6F_6 the parent ion signal and a long tail electron signal are observed, indicating that the electrons are from autodetachment of the parent ions. The smaller EA compared to other work also supports this argument. The chlorine substituted ethene molecules produce Cl^- and parent ions. Analysis shows negative EA's for all the parent ions which suggests they are probably formed in some excited states or the speed of the molecules is over estimated due to the slip between the seed and carrier gas (He).

Reproduced with permission of the copyright owner. Further reproduction prohibited without permission.

Acknowledgements

I first want to express my deep appreciation to my advisor, Professor Philip R. Brooks. He has given me invaluable guidance and advices during the past six years. It was Phil who introduced me to the world of molecular beams. I have learned the basics of gas phase chemical dynamics and lots of technical skills directly from him. He is also a patient and caring person.

I appreciate Professor Robert Curl for his help on all the theoretical questions I had. I learned molecular spectroscopy and group theory from his course and I wish one day I could have some hands on experience in this field. I thank Professor Don Johnson for his time to review my thesis. I would also thank Professor Peter Harland. Peter always brings us good suggestions and interesting stories during his visits. I am thankful to Carter Kittrell, from whom I borrowed many equipment parts and learned all kinds of things. I had a good time working with Jonathan Laib and Crystal Redden. They are very helpful to my research and life.

I am grateful to my friend Yue Fei who helped me to fix my computer and give me instructions on Windows XP. I would also thank my old friend Peng Li in China for his moral support and all the thoughtful discussions we have had during the past 16 years.

I am indebted to my father and sister. They are always supportive through my education and are my constant source of love.

Reproduced with permission of the copyright owner. Further reproduction prohibited without permission.

Table of Contents

Abstract..... ii

Acknowledgements.....iv

List of Figures.....viii

List of Tables..... x

Chapter

1. **Introduction and Background Review**.....1

   1.1 Overview.....1

   1.2 Basic Theory on Gas Phase Electron Transfer.....3

   1.3 Electron Affinity.....12

   1.4 Supersonic Beams.....13

   1.5 Steric Effect in Gas Phase Chemistry.....15

2. **Experimental**.....18

   2.1 Vacuum Chamber.....18

   2.2 Rubidium Source.....21

   2.3 Gas Source.....25

   2.4 Detection of Negative Ions.....26

   2.5 Measurement of the Rb Beam Speed Distribution.....32

   2.6 Wiley-McLaren time-of-flight mass spectrometer.....36

Reproduced with permission of the copyright owner. Further reproduction prohibited without permission.

3. Data Analysis.....40

3.1 Deconvolution of Arrival Time Distribution.....40

3.2 Energy Distribution.....44

3.3 Determination of Reaction Thresholds.....47

4. Results and Discussion.....49

4.1 C_2F_5Cl and C_2F_5I.....49

4.2 Hexafluorobenzene (C_6F_6).....67

4.3 Chlorine Substituted Ethene Series.....76

4.4 Other Molecules.....85

5. Conclusions.....86

Appendix I Program for Deconvolution of the Rb Beam Speed Distribution.....88

Appendix II Program for Determination of Reaction Thresholds.....107

Appendix III Estimation of Slip in the Gas Beam.....131

Appendix IV Reprint of "Evidence for Orbital-Specific Electron Transfer to Oriented Haloform Molecules".....134

References.....158

Reproduced with permission of the copyright owner. Further reproduction prohibited without permission.

List of Figures

1.1 Potential energy curves for the lowest ionic and covalent states of Na-I 5

1.2 Avoided crossing of the potential energy curve for Na-I 6

1.3 Simplified schematic diagram of a collision between a fast alkali atom and stationary halogen atom 8

1.4 Potentials of different types of ground state neutral molecules and negative ions...11

2.1 Crossed beam vacuum chamber 20

2.2 Top view of UHV chamber with TOF mass spectrometers and mini gate valve....21

2.3 Alkali metal oven and nozzle.....22

2.4 Structure of the alkali source nozzle.....23

2.5 Kinematic mount of the alkali beam source 24

2.6 Modified lecture bottle as a sample source 26

2.7 Principle of coincidence time-of-flight mass spectrometry 27

2.8 Coincidence time-of-flight mass spectrum of SF_6 29

2.9 Wiley-McLaren TOF mass spectrometers 30

2.10 Rb beam speed distribution measurement 33

2.11 Normalized gate functions of the chopper wheel 35

2.12 Schematic of a TOF mass spectrometer.....37

2.13 The process of space focusing 39

3.1 Logarithm of the ATD tail signal vs. time 42

3.2 Fit of the ATD by two parameters v_0 and Δv 43

Reproduced with permission of the copyright owner. Further reproduction prohibited without permission.

3.3 Newton diagram for the collision between a Rb atom and a gas molecule 45

4.1 Coincidence time of flight mass spectrum showing negative ions formed by electron transfer to C_2F_5Cl at low energy 50

4.2 Coincidence time of flight mass spectrum showing negative ions formed by electron transfer to C_2F_5Cl at high energy 51

4.3 Coincidence time of flight mass spectrum showing negative ions formed by electron transfer to C_2F_5I 52

4.4 Signal of $C_2F_5^-$ arising from collisions of Rb and C_2F_5Cl at various nominal energy conditions 53

4.5 Relative collision energy distributions calculated from the speed distribution parameters obtained from the arrival time distributions of Rb beam 54

4.6 Experimental signals for Cl^- from C_2F_5Cl and the best fit 55

4.7 Relative energy distributions for the collisions between Rb and C_2F_5Cl to produce Cl^- 56

4.8 Experimental signals for I^- from C_2F_5I and the best fit 57

4.9 Experimental signals for $C_2F_5^-$ from C_2F_5I and the best fit 58

4.10 Experimental signals for $C_2F_5I^-$ from C_2F_5I and the best fit 59

4.11 Relative energy distributions for the collisions between Rb and C_2F_5I 60

4.12 Coincidence mass spectrum of C_6F_6 at low energy 68

4.13 Coincidence mass spectrum of C_6F_6 at medium energy 69

4.14 Coincidence mass spectrum of C_6F_6 at high energy 70

4.15 Relative energy distributions for the collisions between Rb and C_6F_6 71

Reproduced with permission of the copyright owner. Further reproduction prohibited without permission.

4.16(a) Different ion signals produced from the collisions between Rb and C_6F_6 as a function of the backing pressure for Rb beam 72

4.16(b) Ratio of electron to $C_6F_6^-$ signal as a function of Rb beam backing pressure....73

4.17 Electron peak with a long tail from Figure 4.13 74

4.18 Experimental signal of $C_6F_6^-$ and the best fit 75

4.19 Coincidence mass spectrum of C_2Cl_4 78

4.20 Coincidence mass spectrum of C_2HCl_3 79

4.21 Coincidence mass spectrum of $CH_2=CCl_2$ 80

4.22 Coincidence mass spectrum of trans-$C_2H_2Cl_2$ 81

4.23 Relative energy distributions for the collisions between Rb and C_2HCl_3.....82

Reproduced with permission of the copyright owner. Further reproduction prohibited without permission.

List of Tables

2.1 Experimental optimal voltages on mass spectrometers 32

4.1 Measured thresholds 61

4.2 Tests for dimer participation in C_2F_5Cl 65

4.3 Measured thresholds 83

4.4 Thresholds for parent negative ion formation with the estimation of slip 84

Reproduced with permission of the copyright owner. Further reproduction prohibited without permission.

Chapter 1. Introduction and Background Review

1.1 Overview

Negative ions, or anions, are neutral molecules or radicals binding an additional electron. This binding process happens between an electron donor and an electron acceptor and is called electron transfer. Electron transfer usually takes place in solution but also occurs in gas phase collisional processes. In the collisions between atoms and atoms or atoms and molecules, negative ions are formed as part of an intermediate step or as a final product.

Negative ions can be made by bombarding target molecules with electrons. But this usually does not lead to the formation of stable negative parent ions. When the energy of an electron is above a neutral molecule's ionization potential, it knocks off an outer electron from the molecule and produces a positive ion instead of a negative ion. This ionization method is employed in commercial mass spectrometers. Low energy electrons can be very reactive because many molecules are able to capture free electrons resonantly (ALL 89). However, the parent negative ions formed by electron capture are not stable because in single collision there is normally no way to release the energy and become stable parent negative ions. Consequently the temporary negative ion will either autodetach an electron, leaving the neutral molecule in its ground or an excited state, or dissociate into stable fragments, as shown in reactions (1.1) and (1.2). In principle, the temporary negative ion can stabilize itself by emitting a photon, but this process is generally much slower than the competing reactions (1.1) and (1.2).

Reproduced with permission of the copyright owner. Further reproduction prohibited without permission.

$$MX^{-(*)} \rightarrow e^- + MX^{(*)} \quad (1.1)$$

$$MX^{-(*)} \rightarrow M + X^- \quad (1.2)$$

When collision partners are available during the lifetime of the temporary negative ions, however, energy can be transferred to these partners and leave the ions in a thermodynamically stable state. Such a "partner" is introduced by colliding gaseous molecules with alkali atoms in molecular beams and we use this to explore electron transfer and negative ion properties. This method is a powerful tool to investigate the dynamic and thermodynamic properties of negative ions because only individual collisions occur and solvent molecules are not involved. Alkali metals have very low ionization potentials due to their loosely bound *s* electrons and thus are excellent electron donors. The reaction process studied here are

$$Rb + MX \rightarrow Rb^+ + MX^- \quad (1.3)$$

$$\rightarrow Rb^+ + M + X^- \quad (1.4)$$

$$\rightarrow Rb^+ + M^- + X \quad (1.5)$$

The product negative ions can be either the parent ions (1.3) or fragment ions (1.4) and (1.5). The partner here is the Rb^+ ion, which can interact with the temporary negative ions and carry away the excess energy in translation. Solvent molecules in solution function similarly.

For many halogenated molecules, dissociative electron attachment is an extremely effective process with cross sections sometimes considerably greater than 100 $Å^2$. The reaction is driven by the halogen atom's large electron affinity. When the temporary negative ion dissociates, the formation of a thermodynamically stable halogen negative

Reproduced with permission of the copyright owner. Further reproduction prohibited without permission.

ion is energetically favorable. The other reason is that when this dissociative attachment channel is accessible, it will generally strongly compete with autodetachment (OST 89).

In the experiment, reported here, both the alkali atoms and molecules are seeded in separate supersonic beams and are in their ground states. The formation of an ion pair is generally an endoergic process because the electron affinities for most of the molecules are less than the ionization potential of the alkali atoms. As a result, a minimum amount of collisional energy, the reaction threshold, is required to initiate the reaction. From the conservation of energy

$$Th = IP + BDE - EA \tag{1.6}$$

where Th is the reaction threshold, IP is the ionization potential of Rb, BDE is the bond dissociation energy if fragmentation occurs, and EA is the electron affinity of the corresponding negative ion. Since IP and BDE are generally known, the electron affinity can be determined from the threshold.

1.2 Basic Theory on Gas Phase Electron Transfer

The reaction between alkali metal atoms and gas molecules has been studied for decades. It is easier to understand the theory from small systems. Let us start by comparing the interaction of a sodium atom and an iodine atom to that of a sodium ion and an iodine ion. The ionization potential of Na is 5.14 eV and the electron affinity of I is 3.06 eV. Thus if the two particles are infinitely far apart in their ground states, the system Na + I is more stable than the system $Na^+ + I^-$ by 5.14 – 3.06 = 2.08 (eV). If the two ions are not infinitely far apart, they will be stabilized by the Coulombic energy, e^2/R,

Reproduced with permission of the copyright owner. Further reproduction prohibited without permission.

where R is the internuclear distance. When R is measured in angstroms this energy is 14.42/R eV. Accordingly when R is below 6.93 Å the Coulombic stabilization of the ions becomes greater than 2.08 eV and the potential energy of the ion pair becomes smaller than that of the neutral atoms. The neutral atoms do not interact appreciably until R is small enough to form a covalent bond, and the potential energy curve of the neutral system is essentially a constant. Therefore the potential curves of these two systems must cross. In general the intersection distance is determined by matching the ionic and covalent potential at R_c. For large R the van der Waals and induction forces can be neglected and so V_{cov} is zero and V_{ion} is a pure Coulombic potential. With this approximation,

$$R_c = 1/\Delta E \quad \text{or} \quad R_c = 14.42/\Delta E \quad (A) \tag{1.7}$$

where ΔE is the energy difference between the ionic curve and the covalent one at infinite separation, corresponds to

$$\Delta E = IP - EA \tag{1.8}$$

For Na and I at distances less than about 6.93 Å the ionic state is more stable than the covalent state. At very small R the core electron orbitals begin to overlap and cause repulsion, giving a minimum in energy for the ionic curve as illustrated in Figure 1.1.

The ionic and covalent states at the crossing point R_c should have exactly the same energy. However according to von Neumann and Wigner (VON 29,GOO 73) the potential curves of states with the same symmetry do not cross. Here the ionic ground state ($^1\Sigma^+$) and the coupled covalent state ($^1\Sigma^+$) have the same symmetry. This is shown in Figure 1.2. For the more stable B state, Na-I is essentially ionic at small internuclear distances and covalent at large ones. For the less stable A state it is the opposite.

Reproduced with permission of the copyright owner. Further reproduction prohibited without permission.

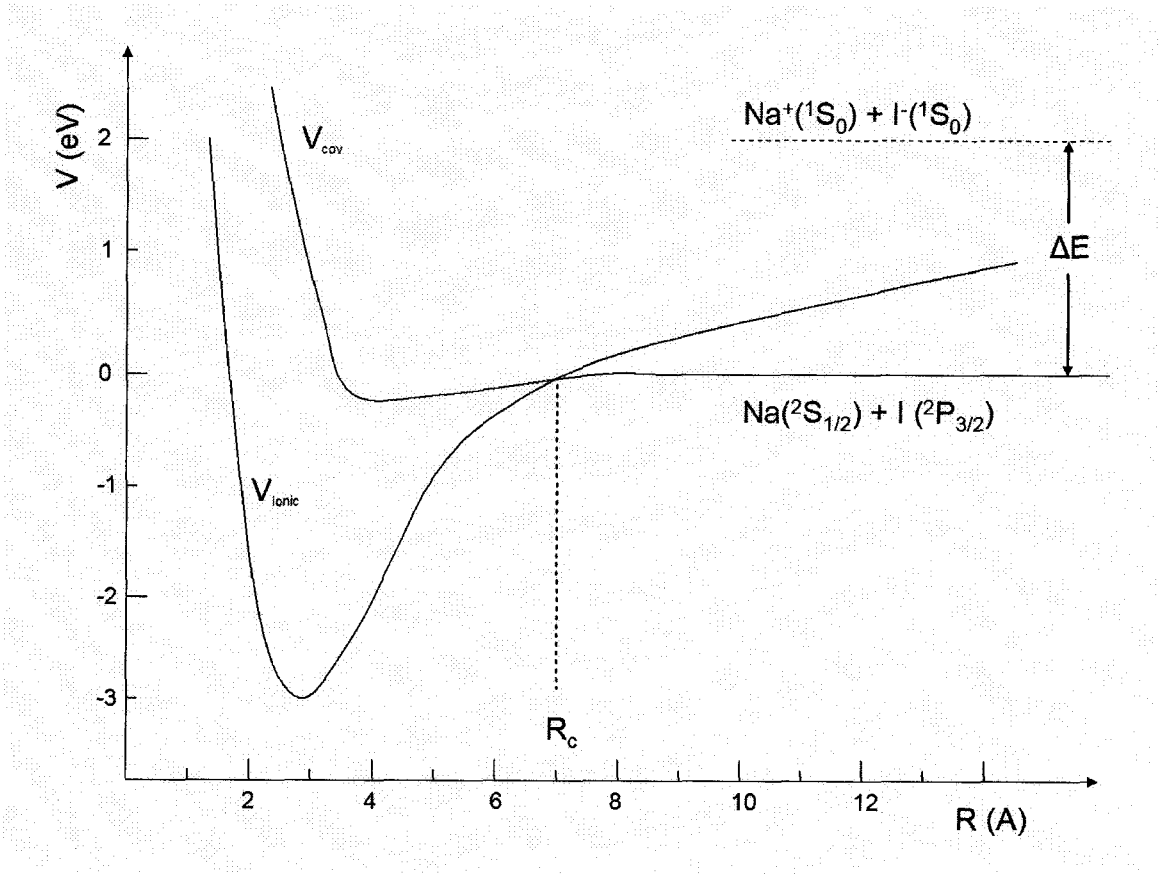

Figure 1.1 Potential energy curves for the lowest ionic and covalent states of Na-I. ΔE is the difference between the ionization potential of Na and the electron affinity of I. R_c is the crossing radius.

Reproduced with permission of the copyright owner. Further reproduction prohibited without permission.

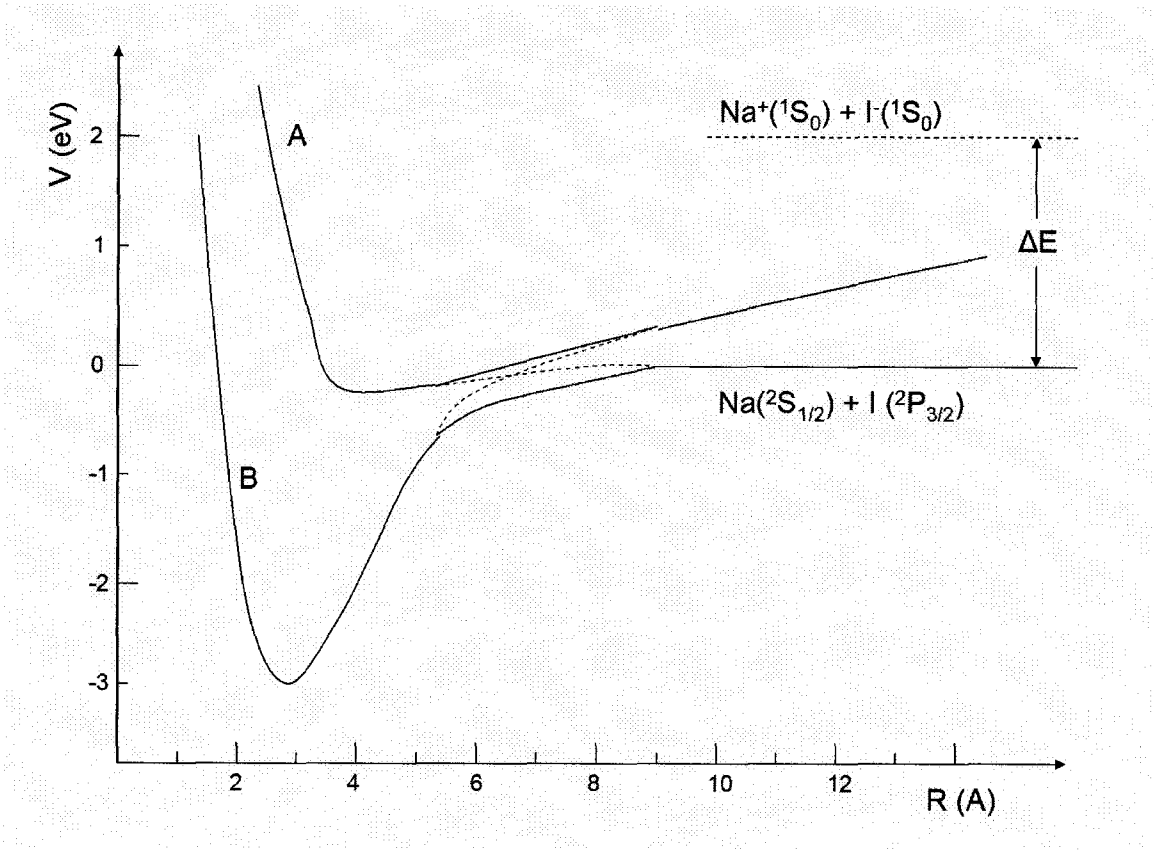

Figure 1.2 Avoided crossing of the potential energy curve for Na-I. The non-crossing point is greatly amplified.

Due to the adiabatic principle, curve B represents the potential energy of a Na atom and an iodine atom when they are brought together very slowly. The two atoms remain basically neutral until they are close to about 7 Å. Then below 7 Å they change to positive and negative ion pair. Curve A represents the potential energy of a Na^+ ion and an I^- ion when they are brought together very slowly. These two ions hold their charges until they are close to the same crossing radius. Then they become neutral for smaller distances. In other words, this means when two adiabatic states of the same symmetry

Reproduced with permission of the copyright owner. Further reproduction prohibited without permission.

come together the non-crossing rule forces the corresponding wave functions to change their character considerably.

However if two particles are brought together very rapidly, there is not enough time for the electrons to adjust their positions in the avoided crossing region. Then the system will have a chance to violate the non-crossing rule and move along a diabatic (or nonadiabatic) curve as shown in Figure 1.1. This process is called a diabatic transition. The probability of a diabatic transition was calculated independently by Landau, Zener and Stueckelberg, assuming the validity of the Born-Oppenheimer approximation. The probability is

$$p = \exp\left(-\frac{\delta}{v_{rad}}\right) \tag{1.9}$$

where $$\delta = \frac{2\pi H_{12}^2(R=R_c)}{d/dR(H_{11}-H_{22})_{R=R_c}}, \quad v_{rad} = v\left(1-b^2/R_c^2\right)^{1/2}$$

$H_{ij} = \langle \Phi_i \mid H_{el} \mid \Phi_j \rangle$ is the matrix element of the electronic Hamiltonian, v_{rad} is the radial component of the initial relative velocity at the crossing point and b is the impact parameter.

Clearly for the formation of an ion pair from two neutral atoms, the impact parameter b has to be less than the crossing distance R_c. This implies the crossing region is traversed twice and electron transfer may occur in the approach or separation of the atoms. Electron transfer can happen at either crossing. Thus there are four different cases for the approach of two neutral atoms. If an electron transfer occurs at the first crossing, then at the classical turning point (the smallest separation between particles) the system becomes ionic; this is called an ionic scattering. Otherwise it is called covalent scattering.

Reproduced with permission of the copyright owner. Further reproduction prohibited without permission.

In the case of ionic scattering an ion pair is formed at the first crossing, therefore the Coulomb attraction brings the two nuclei closer in comparison to covalent scattering. This is shown in Figure 1.3.

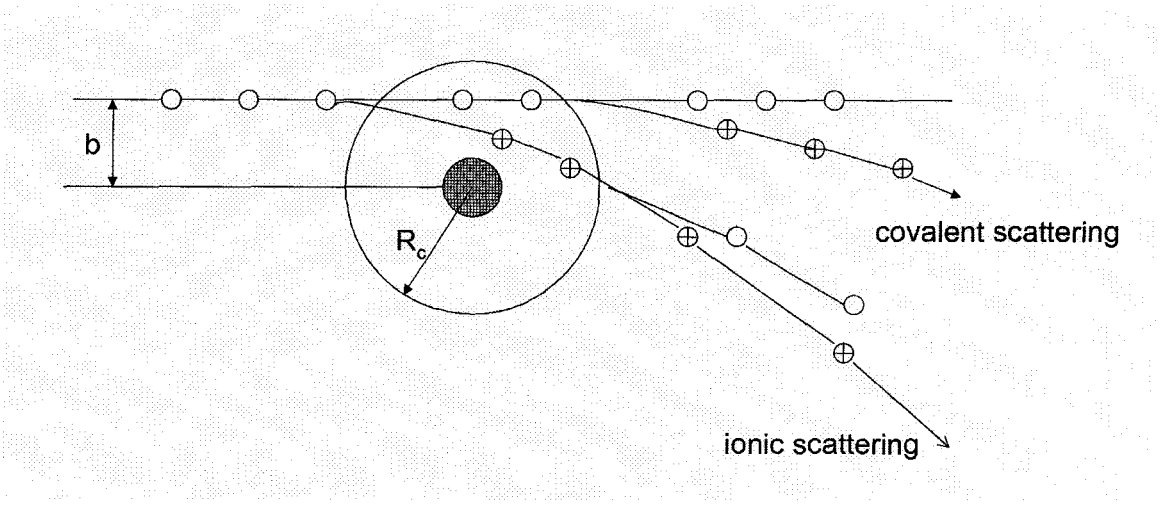

Figure 1.3 Simplified schematic diagram of a collision between a fast alkali atom and stationary halogen atom. The radius of the circle is R_c. The shaded area is the repulsive region of the potentials. The impact parameter is b. The small open circles represent neutral alkali atom, whereas those with a "+" inside represent positive ions.

Since the crossing region is passed twice, neglecting the coherent interference between the probability amplitude, the total probability for an ion pair formation is

$$P(b) = P_{cov} + P_{ion} = p(1-p) + (1-p)p = 2p(1-p) \qquad (1.10)$$

The contributions from the covalent and ionic scattering are equivalent. The total cross section is obtained by integrating all total probability over all b's from 0 to R_c.

Reproduced with permission of the copyright owner. Further reproduction prohibited without permission.

$$Q = 2\pi \int_0^{R_c} P(b) b db = 4\pi R_c^2 F(v/\delta_0) \tag{1.11}$$

where $F(v/\delta_0)$ is a universal function that approaches zero for both very low and very high v, the relative velocity. The maximum value 0.113 is reached at $v/\delta_0 = 2.36$.

Figure 1.1 suggests that R_c is much greater than the bond length of the corresponding stable molecule. Equation (1.11) shows that the cross section is on the order of πR_c^2, which is much greater than the corresponding gas kinetic cross section. This electron transfer process is called the harpoon mechanism: the valence electron from the incoming alkali atom jumps over to the halogen atom, and the Coulomb force brings the ion pair together. This is discussed in Herschbach's paper (HER 66).

The collision and electron transfer between an alkali atom and a molecule are a generalization of the atom-atom interaction. However the number of degrees of freedom has increased and one dimensional potential curves can no longer describe the situation. Multidimensional potential energy surfaces and crossing seams have to be introduced. Electron transfer can occur at the crossing seam of an ionic and a covalent surface. The transition probability can be calculated by a generalized Landau-Zener theory (NIK 68,GIS 81) and the result is similar to equation (1.9).

As a simple first approximation, the motion of the Rb atom with respect to the molecule center of mass can be decoupled from the internal motion of the molecule MX. This implies that excitation and dissociation caused by direct momentum transfer is neglected. Since R_c is large, this is not a bad approximation. The potentials of the neutral molecule and the molecular ion are thus approximately undisturbed by the presence of the atom or ion. In terms of molecular orbital theory, electron transfer from a Rb atom to a MX molecule can be regarded as an additional electron entering one of the lowest

Reproduced with permission of the copyright owner. Further reproduction prohibited without permission.

unoccupied molecular orbitals of MX, which usually has some σ*(M-X) character. Consequently MX^- generally has a larger equilibrium distance and smaller dissociation energy, which facilitate breaking of the M-X bond, see reaction (1.4) or (1.5). Some examples are shown in Figure 1.4. Therefore after the electron transfer the incipient negative ion will be formed on the repulsive part of its potential because of the Frank-Condon process and cause a stretch of the $M-X^-$ bond. Depending upon the potential curves of the molecule and negative ion, this dynamic stretch could lead to the dissociation of the negative ion, as illustrated in Figure 1.4 (b) and (c), or to a bound state, as Figure 1.4 (a) and (d). According to equation (1.7) and (1.8), R_c is a function of the electron affinity of the molecule. If the electron transfer occurs at the first crossing and there is enough time for the bond to stretch during the collision, R_c at the second crossing can be very different. If the stretch is periodic and reversible then R_c oscillates as a function of the collision time (MOU 87).

This research investigates the electron transfer reactions close to their thresholds, so the energy is not too high. Under such circumstance, the Rb^+ ion may have enough time to interact with the stretching incipient negative ion and carry away part of the excess energy. The negative ion could then be relaxed to, or close to, the ground vibrational state and the adiabatic electron affinity could be obtained.

Reproduced with permission of the copyright owner. Further reproduction prohibited without permission.

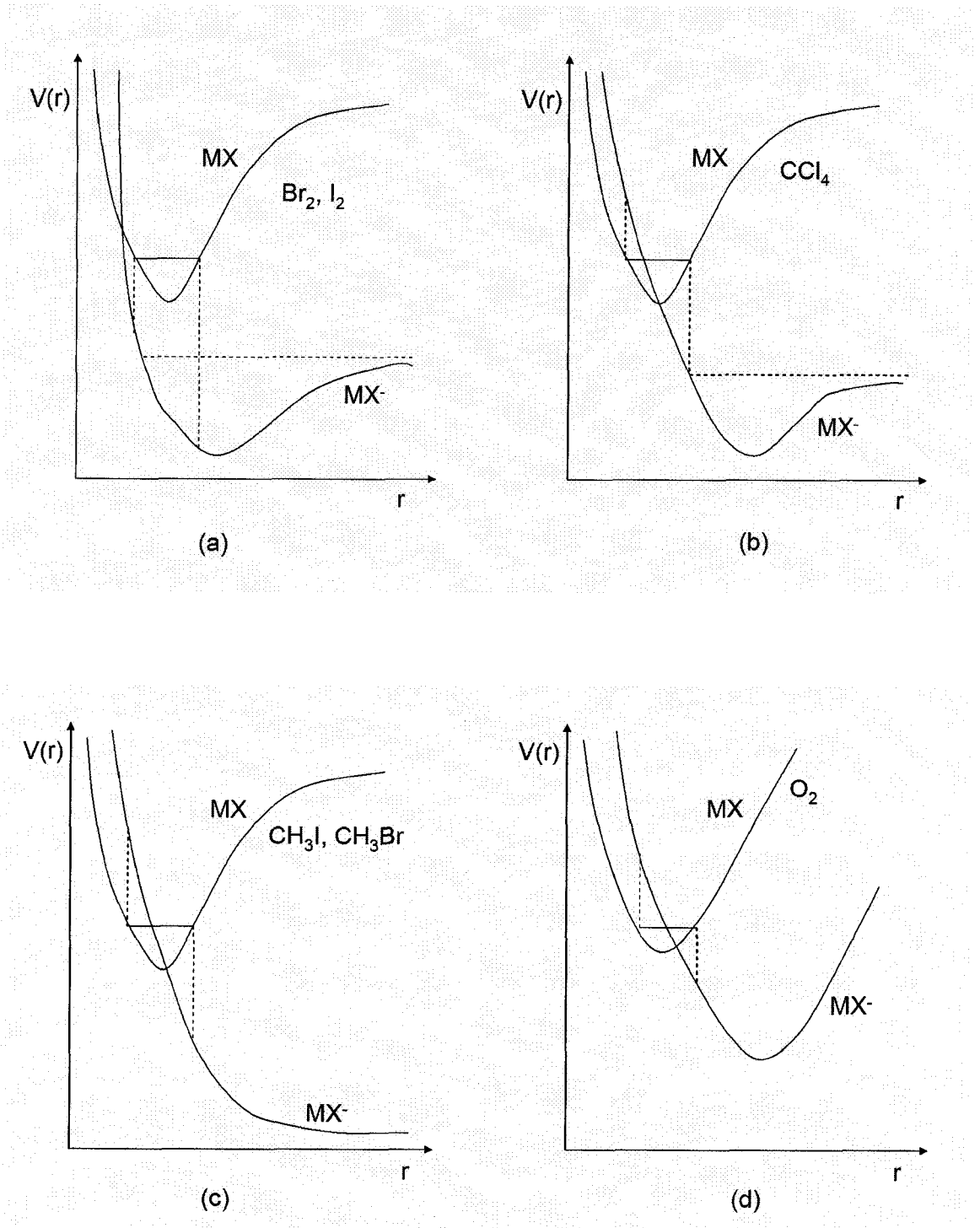

Figure 1.4 Potentials of different types of ground state neutral molecules and negative ions. A parent negative ion can be observed in (a) and (d).

Reproduced with permission of the copyright owner. Further reproduction prohibited without permission.

1.3 Electron Affinity

The basic quantity relating a neutral molecule to its negative ion is the electron affinity. The electron affinity of a molecule MX is defined as

$$EA = E(MX) - E(MX^-) \quad (1.12)$$

where E(MX) is the energy of MX in the ground electronic and vibrational state. This definition is general because the state of MX^- is not specified. The adiabatic electron affinity is defined when MX^- is in the ground electronic and vibrational state. Figure 1.4 shows that the internuclear distance of MX^- is larger than that of MX. Just after the electron transfer the negative ion is in the geometry of the neutral, $r(MX^-) = r(MX) = r_e(MX)$, the energy difference between the incipient negative ion and the neutral molecule is called the vertical electron affinity.

One can collide alkali metals with various molecules in the gas phase to obtain the electron affinities as discussed earlier. The nature of the apparent electron affinities depends on the collision energy. At very high energy the collision time is much shorter than the vibrational time of the negative ion and the Frank-Condon principle applies. The apparent electron affinity will be the vertical one. At energies near threshold the apparent electron affinity may be adiabatic as just discussed and this is the work in our lab.

Laser photodetachment is another method that has been used to measure the electron affinities of many molecules. Typically a fixed frequency laser is used to detach an electron from the target negative ion. The kinetic energy distribution of the detached electrons is measured. Generally the neutral may be left in a number of excited

Reproduced with permission of the copyright owner. Further reproduction prohibited without permission.

vibrational and even electronic states. The adiabatic electron affinity is obtained by determining the highest electron energy. This can be difficult if the ground state of the neutral has a poor Frank-Condon factor. The electron affinity is the difference between the photon energy and the electron arising from the (0, 0) band (LEO 85, ERV 92). The target negative ions are usually generated through ion-molecule chemistry in a flowing afterglow device (LEO 85).

There are other techniques that have been used to measure the electron affinities, such as electron bombardment and thermo chemistry (MAS 76).

1.4 Supersonic Beams

In the early stage of molecular beam experiments, effusive sources were used. The beam is formed by effusion of low pressure gas (a few torr) in a chamber through a small aperture. The speeds of the molecules obey the Maxwell distribution. The width of the aperture has to be small in comparison to the mean free path of the gas molecules. There are no collisions after a molecule has left the chamber, therefore the speed distribution of the gas beam is identical to that in the chamber. The knowledge of effusive beams is well established. But the intensity of the beam is very low, its energy is low and the speed distribution is broad.

Charge exchange is a way to make higher energy beams (mainly used for alkali metals). Alkali metal vapor atoms are surface ionized on a filament and accelerated through the same vapor chamber where resonance charge exchange occurs (ATE 75). A neutral beam is formed and the remaining ions are removed by an electric field

Reproduced with permission of the copyright owner. Further reproduction prohibited without permission.

perpendicular to the beam. The energy is determined by the accelerating voltage on the filament. However the beam intensity is too low to obtain appreciable signals for energies below 10 eV due to space charge.

In 1951 Kantrowitz and Grey (KAN 51) suggested a new method of making molecular beams with high intensity and narrow speed distribution. A high pressure gas sample is expanded through a small orifice to form a hydrodynamic flow. The size of the orifice is greater than the mean free path of the gas molecules allowing collisions among the molecules after they leave the nozzle. These collisions accelerate slow molecules in the stream and slow down the fast ones. As a result the speed distribution greatly shrinks and the temperature of the beam drops to a few Kelvin. The name "supersonic" comes from the fact that the hydrodynamic flow speed is higher than the local speed of sound in the beam. In the expansion rotational and vibrational motions are also converted to the translation and the corresponding temperatures decrease drastically. This rotational cooling greatly simplified the rotational and vibrational spectra of the beam molecules and revolutionized spectroscopy (SMA 77, SMA 75, SNA 81). Downstream from the nozzle the molecular density drops and the molecules reach the collision free region where a skimmer is placed on the beam axis. The skimmer collimates the beam, reduces the number of collisions between the incident beam molecules and the scattered molecules, and makes differential pumping possible.

An important aspect of supersonic beams is that all the molecules are traveling at nearly the same speed. This makes it possible to seed molecules of interest into a carrier gas and either accelerate or decelerate them. In our lab Rb atoms are seeded in H_2 for one beam and small organic molecules in He/Ar for the second beam. During the expansion

Reproduced with permission of the copyright owner. Further reproduction prohibited without permission.

the carrier gas molecules collide with the seed molecules many times and they all reach essentially the same speed at the end. By seeding heavy molecules in a light carrier gas the speed of the heavy molecules can be increased drastically. The amount of acceleration is determined by the number of collisions. One convenient way of controlling the number of collisions is to vary the pressure behind the nozzle. The seed fraction has to be low and the pressure high otherwise serious "slipping" occurs and the desired speed will not be achieved.

1.5 Steric Effect in Gas Phase Chemistry

Chemical reactions depend on the mutual orientation of the reagent. The kinetic theory of bimolecular reaction shows

$$k_{12} = \rho Z_{12} e^{-E_a/RT} \tag{1.13}$$

where k_{12} is the rate constant, Z_{12} is the specific gas kinetic collision frequency, E_a is activation energy, R is the gas constant, T is the absolute temperature, and ρ (which lies between 0 and 1) is the steric factor, the fraction of collisions in which the reagents are properly oriented. A well known example in the bimolecular nucleophilic substitution (S_N2) reaction, such as

$$OH^- + CH_3Br \rightarrow CH_3OH + Br^- \tag{1.14}$$

This reaction proceeds through the attack of OH^- at the backside (H end) of the carbon atom. The molecule inverts like a windblown umbrella expelling the Br^- in the process. This so called Walden inversion depends critically on the size of the groups undergoing the inversion. If the hydrogen atoms are replaced by methyl groups, the reaction rate will

Reproduced with permission of the copyright owner. Further reproduction prohibited without permission.

decrease orders of magnitude because the larger CH_3 groups impede the attack and inversion.

There are basically two methods of orienting molecules in the gas phase prior to collisions. One is to apply extremely strong electric fields upon simple dipole molecules (LOE 90, FRI 91), the other is to first select molecules exhibiting a first order Stark effect in certain quantum states and then orient the state-selected molecules in weak fields (BRO 96, LOE 95, PAR 89). The latter is used in our experiments.

The molecules under investigation are haloform molecules. They are symmetric top molecules with dipole moments along the symmetry axis. A supersonic molecular beam (target molecules seeded in He) is directed along the axis of an inhomogeneous electric hexapole field, and molecules are deflected in this field according to their rotational states. After passing through the field, molecules in quantum states that increase in energy as the electric field increases are focused and others are defocused. The focused molecules are then oriented in a weak electric field.

We studied electron transfer reactions between these haloform molecules and K atoms. The fast K atoms are made in this case by a charge exchange process. Collisions occur in a weak electric field between two time-of-flight mass spectrometers which are identical except that one is biased to detect positive ions, the other to detect negative ions. The ion pairs are detected in coincidence (described in Chapter 2).

Ion signals depend strongly on energy because the cross sections increase with energy. In order to emphasize the effect of molecular orientation on reactivity we report the steric asymmetry factor, *G*, defined as

Reproduced with permission of the copyright owner. Further reproduction prohibited without permission.

$$G(E)=\frac{\sigma_{-}(E)-\sigma_{+}(E)}{\sigma_{-}(E)+\sigma_{+}(E)} \tag{1.15}$$

where $\sigma_{\pm}(E)$ are the ion production cross sections for either positive or negative end attack. If reaction occurs at only one end, $G = \pm 1$, depending on the polarity of the reactive end. If all orientations were equally reactive, G would be zero.

The major products for the collisions between K atoms and haloform molecules are the X^- ions. The steric asymmetry factor G based on X^- shows that the negative end of $CHCl_3$ and $CHBr_3$ is slightly more reactive than the positive end. For CHF_3 the asymmetry factor is negative at low energies (below ~ 6.5 eV) but positive at high energies. G ranges from ~-0.6 to ~0.6. We believe electrons are transferred into different molecular orbitals at different energies. The hinderance caused by the X groups also plays a role in the steric effect.

This work was published in the *Journal of American Chemical Society*. For more details please refer to Appendix IV.

Reproduced with permission of the copyright owner. Further reproduction prohibited without permission.

Chapter 2. Experimental

Experiments were conducted to study the electron transfer between Rb atoms and various simple organic molecules. In these experiments, a neutral beam of molecules is crossed with a beam of fast rubidium atoms at a collision angle of 120° under high vacuum. If the energy of the colliding pair is above the reaction threshold for forming an ion pair at infinite separation, an electron transfer creates a positive ion (Rb^+) and negative ion which are detected in separate time-of-flight mass spectrometers in coincidence. The speed distribution of the Rb atoms is directly determined by measuring the arrival time distribution of atoms falling on a surface ionization detector, and the speed distribution of the gas beam is approximated as that of an isentropic expansion.

2.1 Vacuum Chamber

The two supersonic beams cross at an angle of 120° in the ultra high vacuum (UHV) chamber that sits in the hexagonal chamber, as shown in Figure 2.1. The Rb chamber is pumped by a Varian 0163 diffusion pump backed by a Leybold-Heraeus D90A mechanic pump; the gas beam chamber is pumped by a Varian 0185 diffusion pump backed by another D90A mechanical pump. The hexagon chamber is pumped by three Varian VHS-6 diffusion pumps that share the same Leybold-Heraeus D8A backing pump. A cylindrical liquid nitrogen trap is inserted into the hexagon chamber to increase the pumping speed for condensibles. Another liquid nitrogen trap is welded within the Rb flight tube to reduce the pressure. Rb atoms from the beam fly through this tube and their

Reproduced with permission of the copyright owner. Further reproduction prohibited without permission.

speed distribution is measured by the travel time through a known distance. A partition plate for each beam separates the beam source chamber from the hexagon chamber. Each beam passes through a Beam Dynamics skimmer and a hole in the partition plate before entering the hexagon chamber. The skimmers and holes collimate the beams and achieve differential pumping. The gas beam can be flagged with a solenoid-driven flag that is mounted on the partition plate.

The UHV chamber is pumped by a Leybold-Heraeus 360CSV turbo pump backed with a Leybold-Heraeus D8A mechanical pump. An ionization gauge is installed on each chamber to monitor the pressure. When both beams are turned on, the pressure in the Rb chamber ranges from ~5 x 10^{-6} to ~5 x 10^{-5} torr, the gas beam chamber is ~5 x 10^{-6} torr, hexagon chamber is ~3 x 10^{-6} torr and UHV is ~1 x 10^{-6} torr. Due to space and equipment limitations the UHV chamber is connected to the turbo pump through two Tees.

Four ½'' size holes are drilled in the UHV chamber for the beams to pass through. Each pair of holes are diametrically opposite to assure alignment and minimum pressure buildup inside the chamber. A mini gate valve with O-ring seal covers each hole. This is shown in Figure 2.2. When all the valves are closed the pressure in the UHV chamber can reach 2 x 10^{-8}. This UHV chamber not only provides better vacuum but also keeps the mass spectrometers from oil contamination due to back streaming of diffusion or/and mechanical pump oil.

Reproduced with permission of the copyright owner. Further reproduction prohibited without permission.

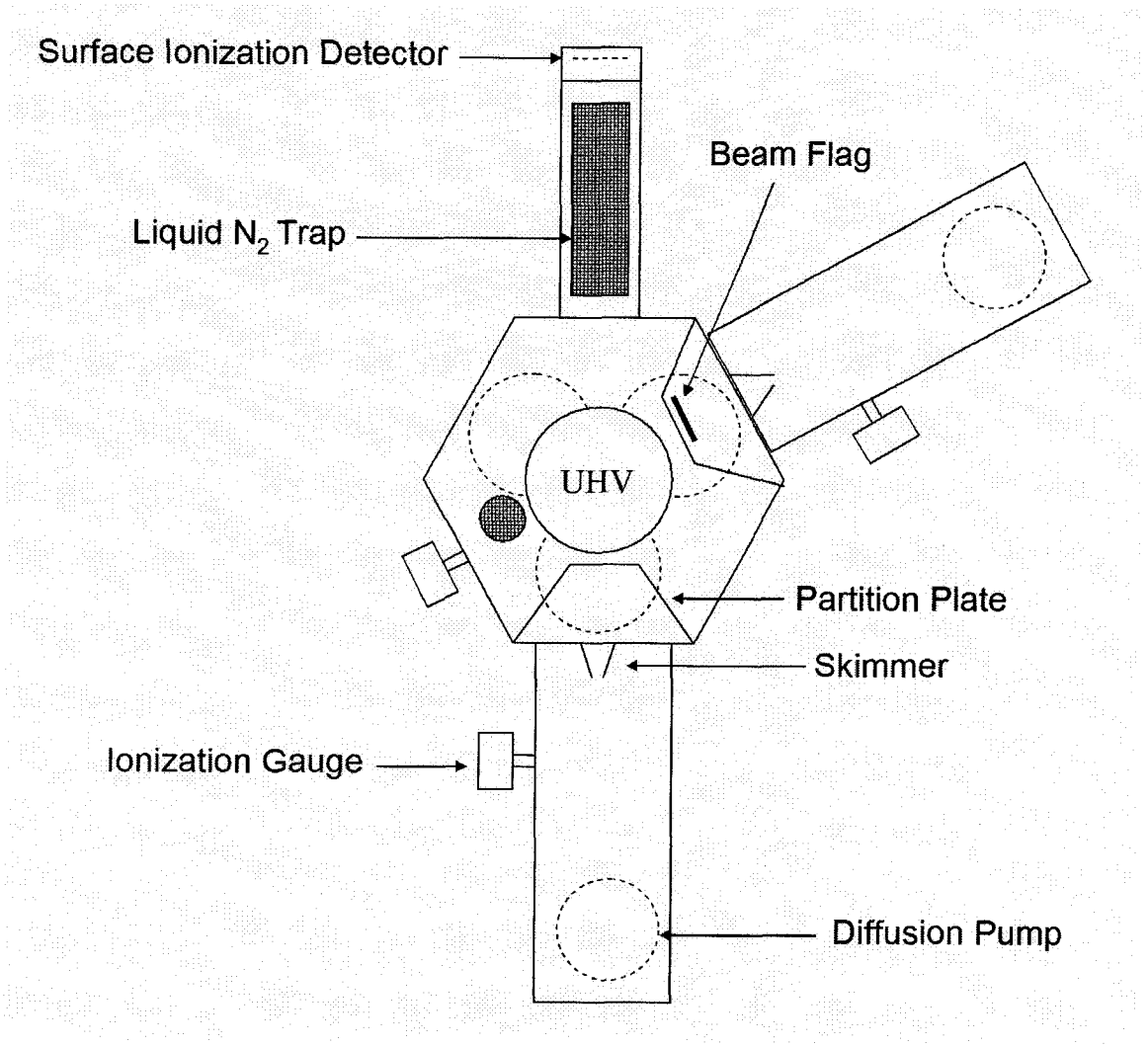

Figure 2.1 Crossed beam vacuum chamber

Reproduced with permission of the copyright owner. Further reproduction prohibited without permission.

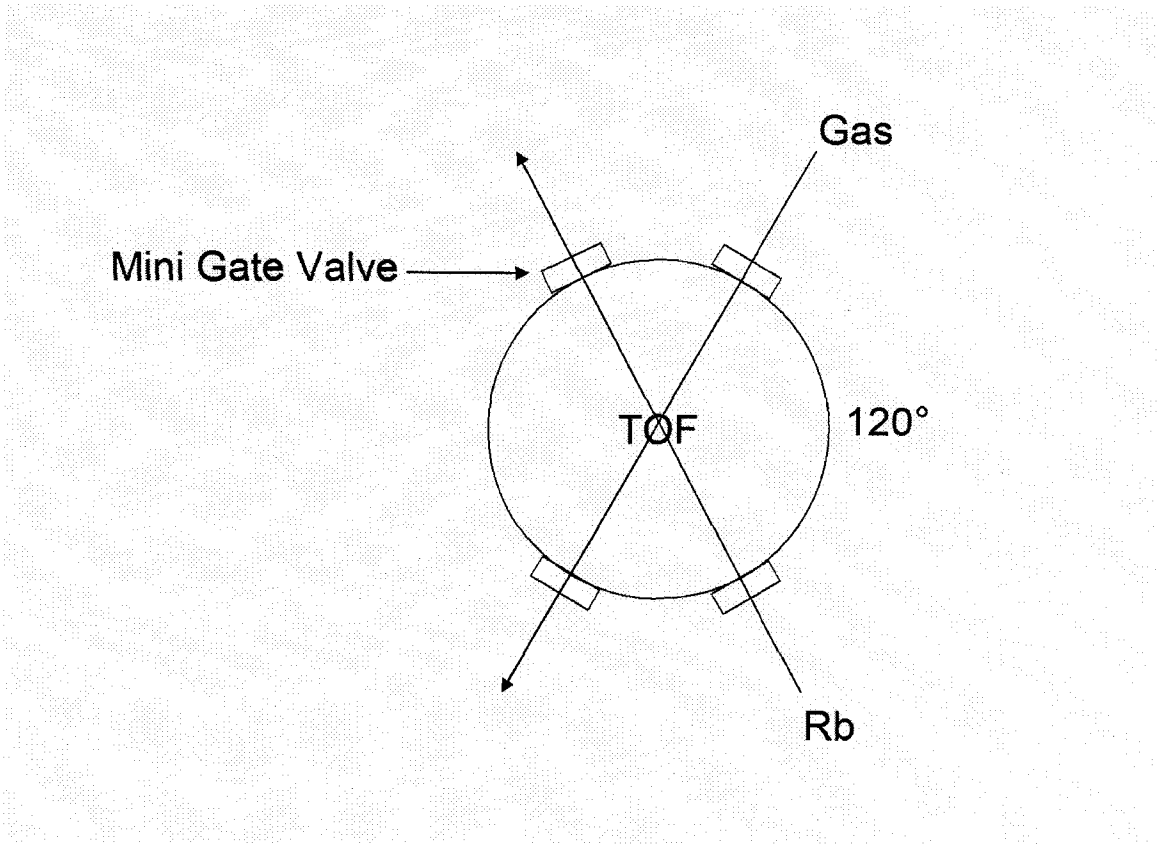

Figure 2.2 Top view of UHV chamber with TOF mass spectrometers and mini gate valves

2.2 Rubidium Source

The alkali source consists of an oven body and a nozzle that are connected together as shown in Figure 2.3. The oven body is made of stainless steel and a Swagelok fitting is welded to the nozzle side. A long coiled 1/8 " copper tube and a VCR fitting are connected to H_2 on the input side. Holes are drilled in the body for the tantalum heating springs. These springs are made by winding 0.010'' tantalum wires on a 1/16 " rod. The springs are covered by ceramic tubes and fish spines for electrical isolation and tied to

Reproduced with permission of the copyright owner. Further reproduction prohibited without permission.

copper wires that supply the power. Rb ampoules are ordered from Strem Chemicals, Inc and broken inside the oven. A ~5cm^2 tantalum mesh is left in the oven with the alkali metal to facilitate evaporation. The oven is sealed by a 2 ¾ " conflat flange. Six screws are tightened to seal the oven. The cover is also heated to keep the alkali metal from condensing on it. One of the holes on the oven body holds a chromel-alumel thermocouple to monitor the temperature. The operating temperature is ~ 220 °C.

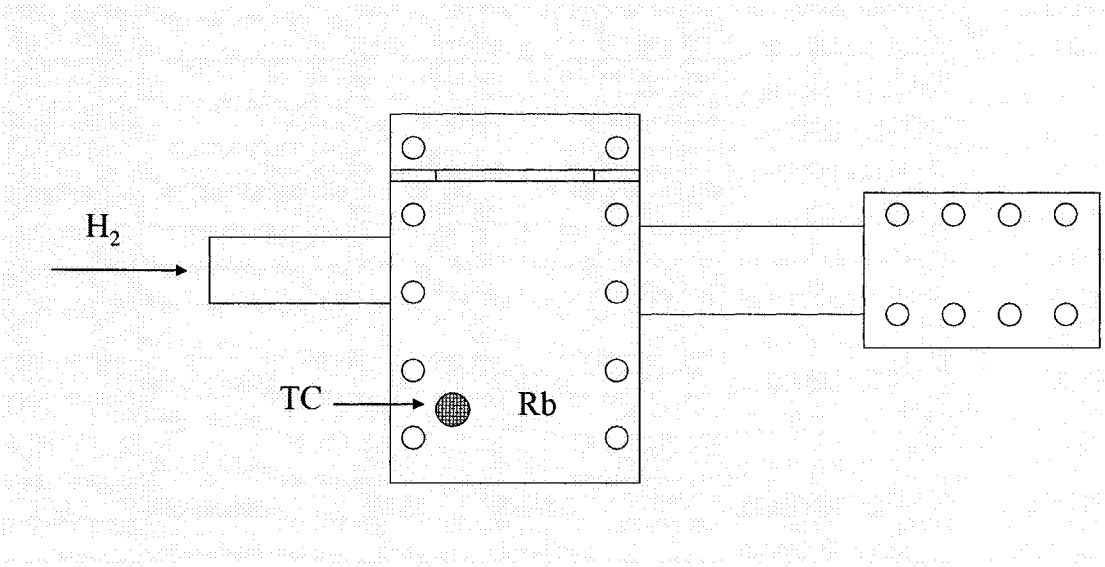

Figure 2.3 Alkali metal oven and nozzle

The nozzle is made of stainless steel VCR fittings and a Bird Precision disk as shown in Figure 2.4. E is a stainless steel VCR gland (1/4'' tubing) machined to a knife edge, B is a cut of the heavy side of gland, C is a gasket coming with the glands, and D is a Bird Precision disk with a 0.0020 " ruby orifice. The knife edge of E makes the seal on D. The assembly is secured within the female nut A. The whole nozzle is in a sleeve

Reproduced with permission of the copyright owner. Further reproduction prohibited without permission.

encircled with tantalum spring heaters and then wrapped with zirconia felt to minimize radiative heat loss. A chromel-alumel thermocouple is located between the sleeve and the nozzle. The operating temperature is 600~800 °C.

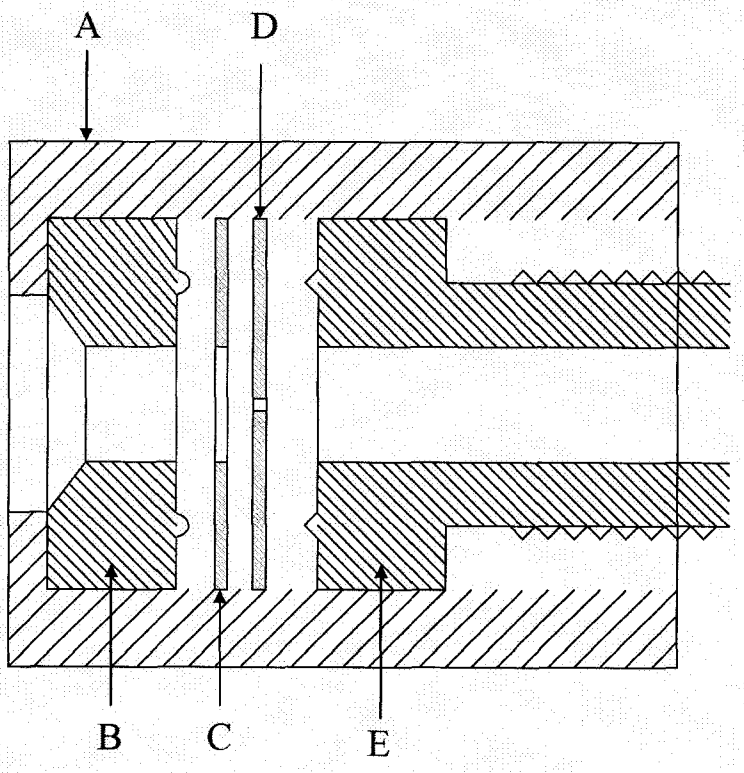

Figure 2.4 Structure of the alkali source nozzle

Reproduced with permission of the copyright owner. Further reproduction prohibited without permission.

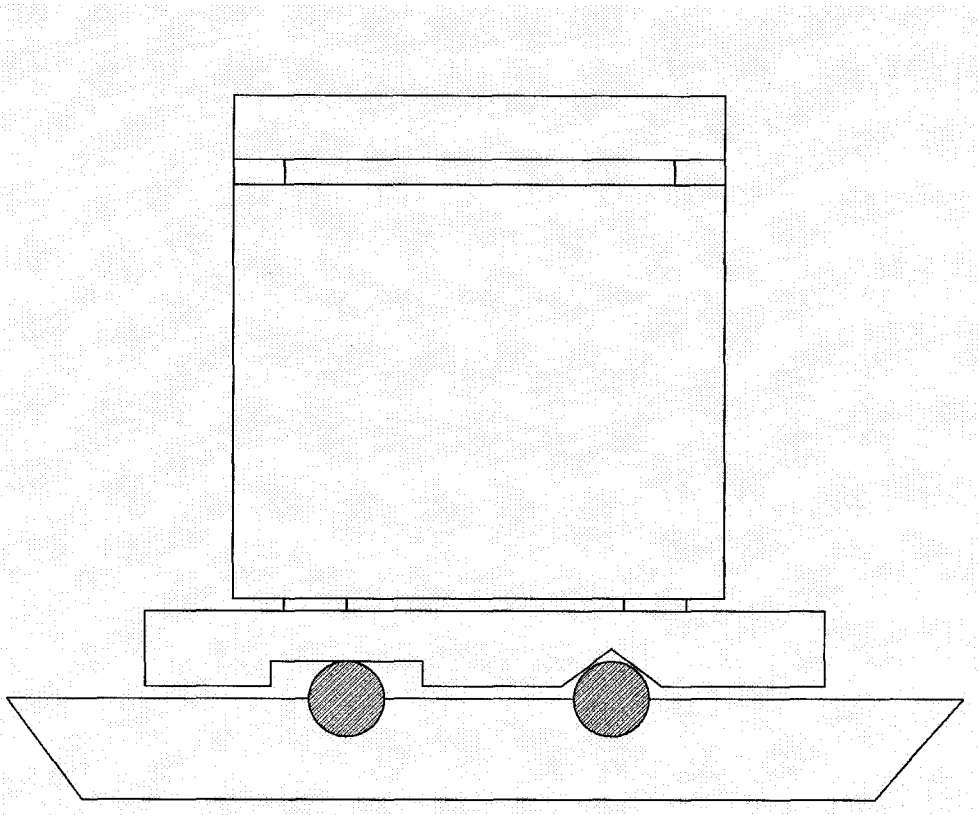

Figure 2.5 Kinematic mount of the alkali beam source

The oven nozzle combination sits on the rails of a kinematic mount and is secured by two "L" shape steel clamps. High pressure H_2 (~30 psi out of a regulator) is connected to the oven through a needle valve that manually controls the pressure inside the oven. An MKS Baratron measures the pressure in the gas line.

A Beam Dynamics skimmer is mounted 2~3 cm away from the nozzle. This skimmer is used to collimate the beam and achieve differential pumping. On the other side of the skimmer is the hexagon chamber.

Reproduced with permission of the copyright owner. Further reproduction prohibited without permission.

2.3 Gas Source

If the sample is gaseous at room temperature, it is mixed with He or Ar depending on the molecular weight and the desired energy. For heavy molecules Ar is more often chosen as it reduces the "slip" (the departure of observed velocity from theoretical value) during the supersonic expansion. When the sample is a liquid with a reasonably high vapor pressure, it is vacuum freeze-thawed to remove the air dissolved. The flask is then opened to a vacuum tank until it is filled with the vapor. He or Ar is then added to make the expansion mixture. If the vapor pressure of the sample is too low to make a mixture, a modified lecture bottle serves as the sample source as illustrated in Figure 2.6. The liquid sample fills the bottom part of the lecture bottle and a fiber glass tube connects the inlet line to the liquid. The fiber glass tube helps to maintain the vapor pressure above the liquid by acting as a wick. The gas pressure at the nozzle is regulated by a Granville-Philips automatic pressure controller to 250 ± 5 torr to ensure a supersonic flow while maintaining a reasonable vacuum. An MKS baratron monitors the output pressure and provides the input signal to the automatic pressure controller.

The gas oven and nozzle are essentially the same as the Rb source except the oven cover is sealed by an O-ring. It is kept at room temperature unless a solid sample is loaded and heated.

Reproduced with permission of the copyright owner. Further reproduction prohibited without permission.

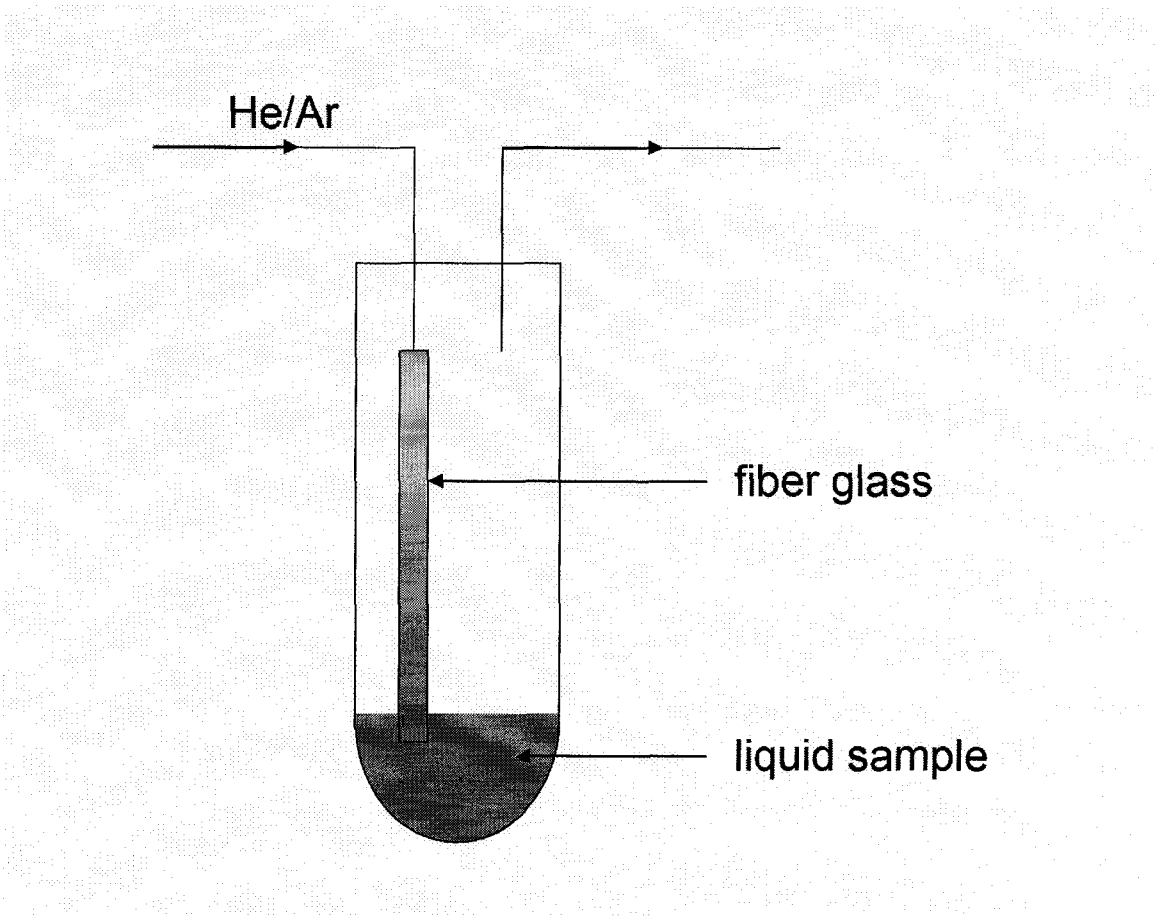

Figure 2.6 Modified lecture bottle as a sample source

2.4 Detection of Negative Ions

All the negative ions produced in the collisions are detected by coincidence time-of-flight mass spectrometry. This is illustrated in figure 2.7. The alkali beam and the gas beam cross at an angle of 120° in a horizontal plane. Each of them passes through a pair of mini gate valves as shown in Figure 2.2. During the collision an electron is transferred from a Rb atom to the gas molecule and if the energy is greater than the reaction

Reproduced with permission of the copyright owner. Further reproduction prohibited without permission.

threshold an ion pair is formed. The parent negative ions may break apart into smaller fragments.

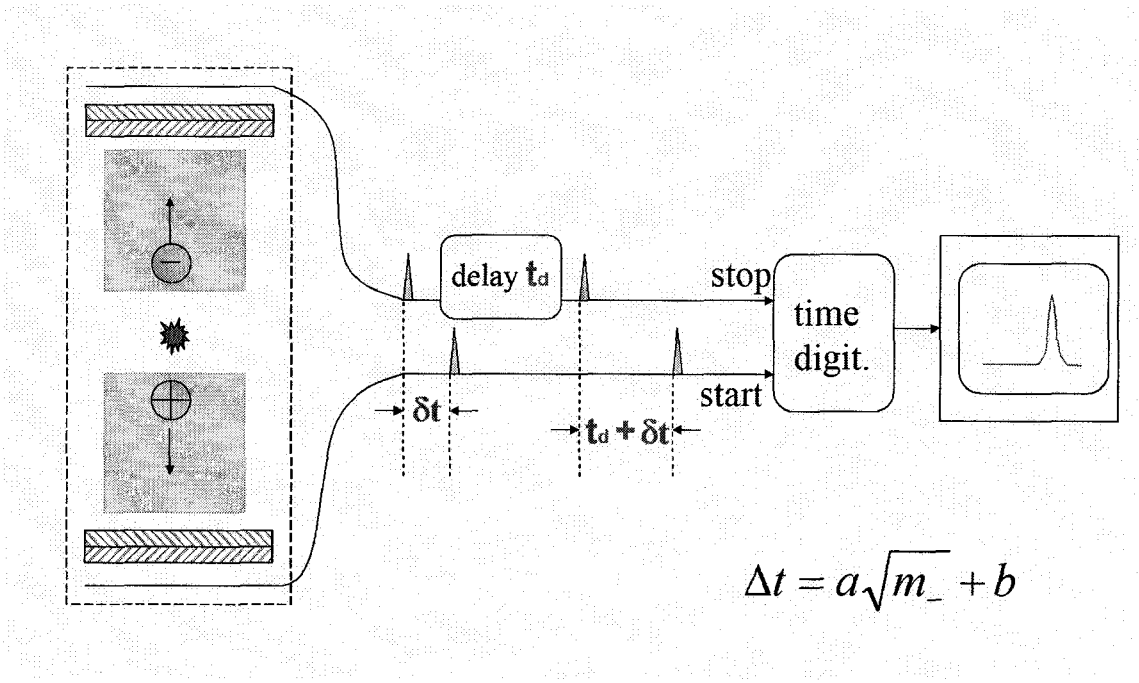

Figure 2.7 Principle of coincidence time-of-flight mass spectrometry

In the UHV chamber there are two identical mass microchannel plate ion detectors that are perpendicular to the beam plane. The top mass spectrometer is at positive voltages whereas the bottom one is at negative voltages of the same magnitude. Thus the positive ions (almost all Rb^+) are extracted to the bottom detector and negative ions to the top. Every ion that impinges on the detector generates an electric pulse. This pulse travels through an ORTEC 9301 fast preamp, an ORTEC 9320 amplifier/discriminator and reaches a LeCroy time digitizer. The positive ion pulse triggers the time digitizer which waits up to 10 μs for a pulse from the negative ion

Reproduced with permission of the copyright owner. Further reproduction prohibited without permission.

detector to stop the digitizer. If a negative stop pulse is recorded in this interval the TDC produces a 12 bit digital signal proportional to the time between pulses. The negative ion pulses are delayed 4000 ns by a Stanford delay/pulse generator so that the negative pulse always arrives after the positive pulse. The usual count rate is in the range of 100~10000 particles per second. The number of ions produced in 10 μs is thus only 0.001~ 0.1, so it is almost certain that the negative ion formed in the same event with the positive ion is counted. A computer collects the number of stop pulses in the 2048 channels of the TDC, giving the number of ion pairs vs. the time difference.

The time for an ion to travel from the collision center to the detector is $t_+ = a_+\sqrt{m_+} + b_+$ and $t_- = a_-\sqrt{m_-} + b_-$, where "+" and "-" stand for positive and negative ions, respectively. The parameters a_+, b_+, a_-, and b_- are determined only by the geometry of the mass spectrometers and the voltages applied and thus are all constants. The mass m_+ is 85 or 87 amu corresponding to the two main Rb isotopes. Combining these two equations gives $\Delta t = t_d + \delta t = t_d + t_- - t_+ = t_d + a_-\sqrt{m_-} + b_- - a_+\sqrt{m_+} - b_+ = a_-\sqrt{m_-} + b_i$, where b_i is combination of the constant terms and I refers to ^{85}Rb and ^{87}Rb. The flight time difference varies as the square root of the negative ion mass. Samples such as SF_6 and CF_3Br are used as standards to determine a_- and b_i since the product negative ions from these molecules are known. The mass of new negative ions are determined based upon this calibration line. Figure 2.8 is the spectrum of SF_6. The double peak is due to the two isotopes of Rb. ^{85}Rb and ^{87}Rb have two slightly different values of t_+ and SF_6 has only one mass 146. Consequently there are two different Δt for SF_6 which appear as two close peaks.

Reproduced with permission of the copyright owner. Further reproduction prohibited without permission.

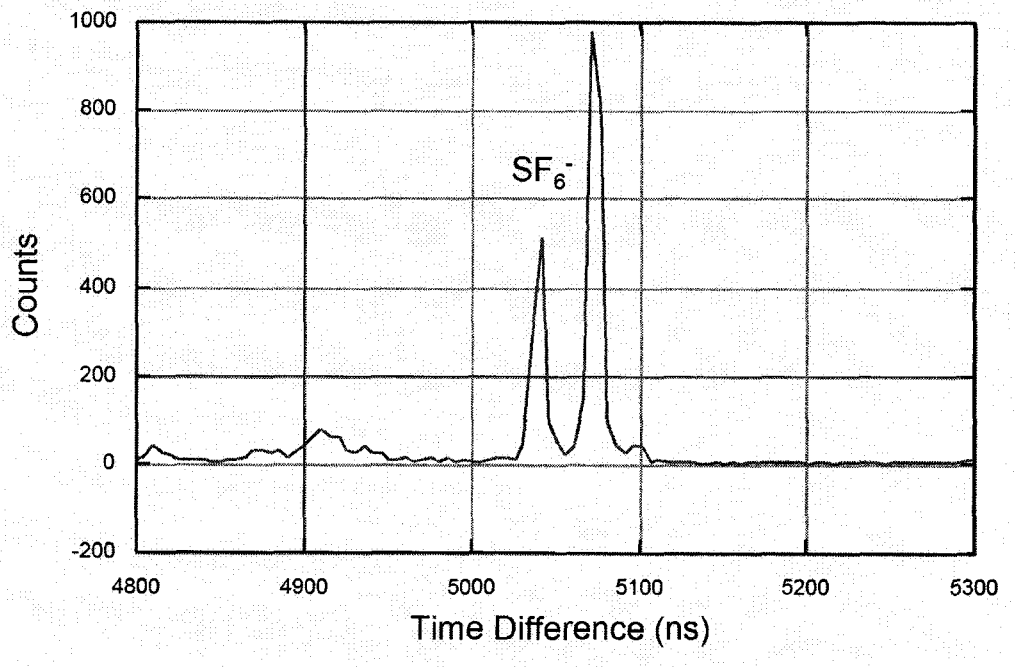

Figure 2.8 Coincidence time-of-flight mass spectrum of SF_6

Reproduced with permission of the copyright owner. Further reproduction prohibited without permission.

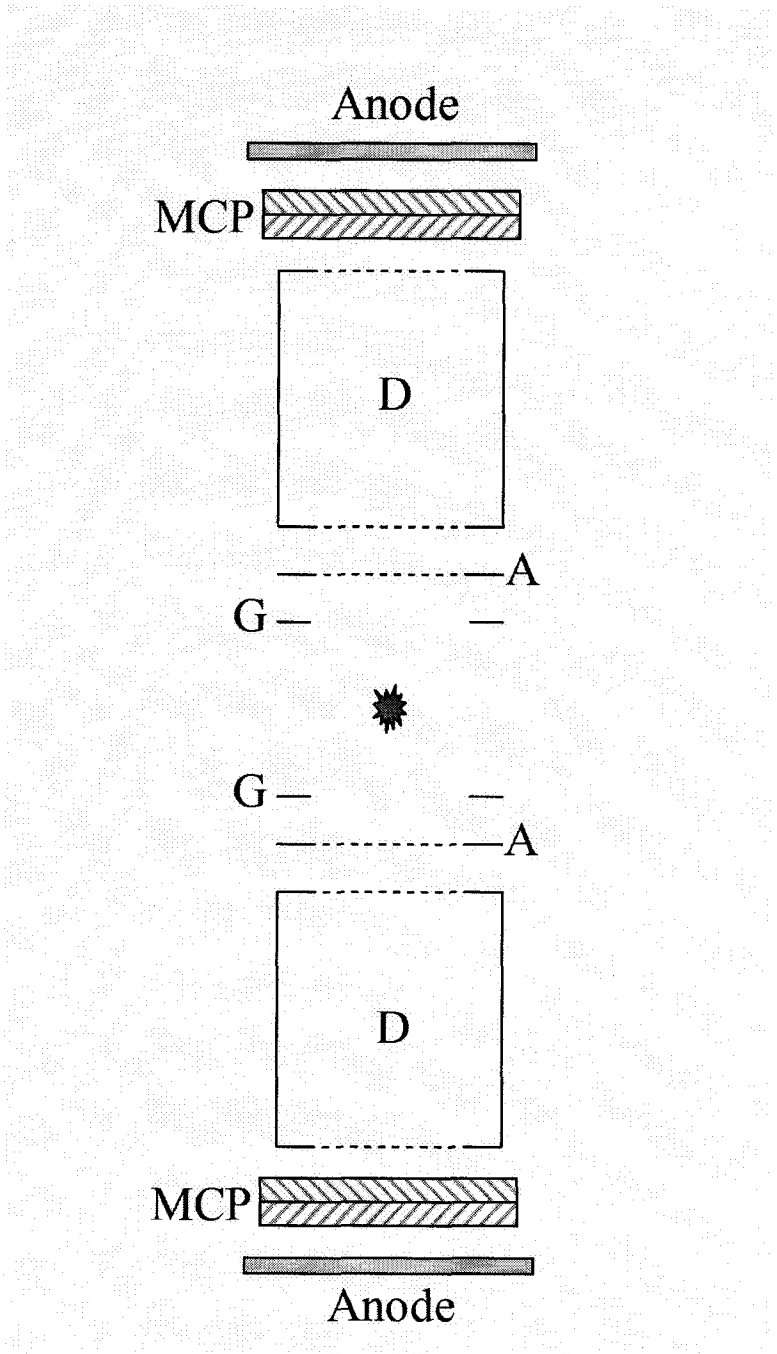

Figure 2.9 Wiley-McLaren TOF mass spectrometers

Reproduced with permission of the copyright owner. Further reproduction prohibited without permission.

The structure of the two TOF Wiley-McLaren (WIL 55) mass spectrometers is shown in Figure 2.9. Each one consists of a guard, an accelerator, a drift tube and a detector. The guards and accelerators are made of 2'' diameter stainless steel rings of 1'' opening covered by 95% transparent Ni mesh (Buckbee-Mears). Each drift tube is made of four deflection plates ~10 cm in length. The two ends are covered by the same kind of rings as the accelerators. Each detector is made of a pair of Burle micro channel plates and a stainless steel plate as an anode.

SF_6 is used as a sample to find the voltages giving optimal resolution (discussed in section 2.6) due to its high signal. Once they are found they apply to all negative ions regardless of their mass (WIL 55). The voltages on the accelerators and the drift tubes are adjusted until the optimal resolution is established. The voltages on the detectors are kept constant. The guard plates are installed to make the field uniform. In theory only the ratio of the voltage on the accelerator to the drift tube determines the optimal resolution. However in order to collect all the ions from the collisions the voltages are set to reasonably high values, the first line in Table 2.1. In order to make the drift tubes field free regions, the voltages applied on the ends and sides are the same (no deflection voltages are applied). The R values for positive and negative ions are slightly different because the two beams do not collide exactly in the middle of the two mass spectrometers.

Reproduced with permission of the copyright owner. Further reproduction prohibited without permission.

Table 2.1 Experimental optimal voltages on mass spectrometers

V_A	V_D	R		V_A	V_D	R
500	950	1.9		-500	-1030	2.06
400	760	1.9		-400	-820	2.05
300	570	1.9		-300	-580	1.93

V_A and V_D stand for the voltages on the accelerator and drift tube, respectively.

$R = V_D/V_A$. The first three columns are for negative ions (positive voltages), the last three columns are for positive ions.

2.5 Measurement of the Rb Beam Speed Distribution

The Rb atoms are accelerated by H_2 under pressures up to ~1500 torr at ~770 °C, whereas the heavier gas molecules are expanded in He or Ar at room temperature and 250 torr. According to the theory of isentropic expansion (equation 3.8) most of the collision energy comes from the Rb beam. However, neither of these two beams is monoenergetic. In order to quantitively correlate the reaction behavior with energy and to find the electron affinities of the product negative ions, it is necessary to have the speed distributions of both beams.

The speed distribution of the Rb beam is determined by measuring the arrival time distribution (ATD) of the Rb beam on a hot tungsten filament as shown in Figure 2.10. The speed distribution of the gas beam is estimated by theory.

Reproduced with permission of the copyright owner. Further reproduction prohibited without permission.

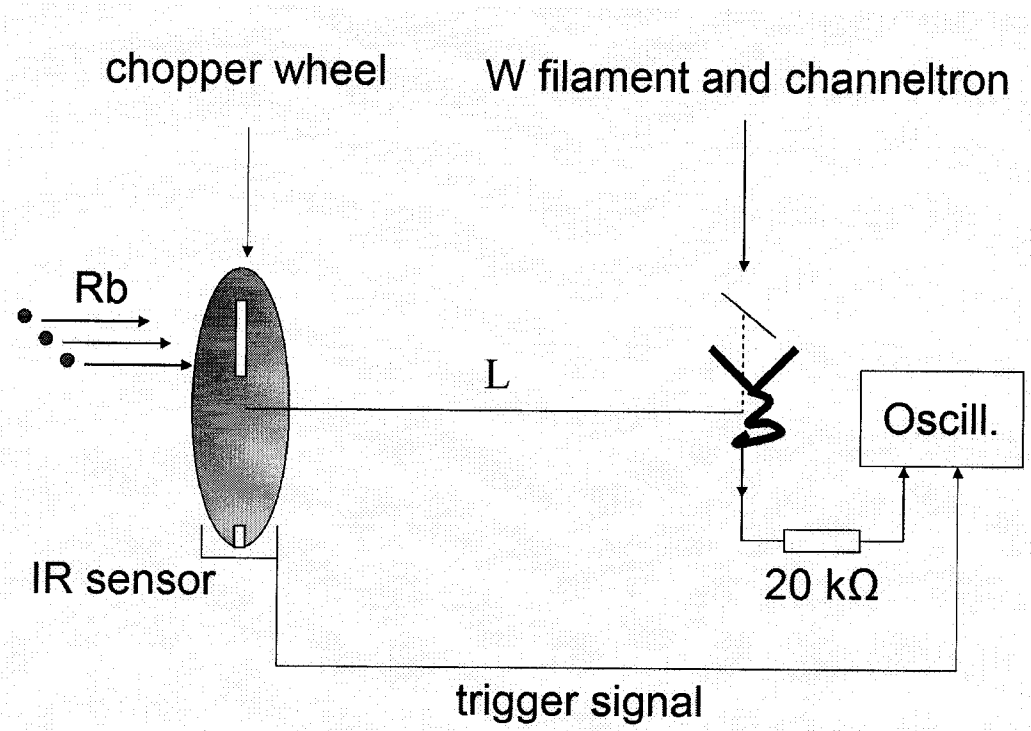

Figure 2.10 Rb beam speed distribution measurement

After passing through the UHV chamber the Rb atoms strike a chopper wheel that is perpendicular to the beam and spinning at 400 Hz. A slit in the wheel chops the beam into small packets which then fly 563 ± 2 mm until they hit a hot tungsten filament. The Rb atoms are surface ionized on the filament and then extracted into an electron multiplier. The output current flows through a 20 kΩ resistor. The voltage drop is then monitored as a function of time by a Tektronix TDA 430A oscilloscope and stored in a computer. A second slit on the edge of the chopper wheel is diametrically opposed to the one that chops the beam. An IR sensor is mounted across the edge and sends the trigger signal to an oscilloscope.

Reproduced with permission of the copyright owner. Further reproduction prohibited without permission.

The chopper wheel is made of aluminum and is 3 " in diameter. The slits are 0.015 " wide. The one chopping the beam is 0.375 " long. A balancing hole is drilled on the line of the slits. The wheel is driven by a 400 Hz hysteresis synchronous motor from Globe Motors. It can rotate clockwise and counter clockwise. A 400 Hz sinusoidal signal from an EZ FG-8002 function generator is fed into a Dukane 125 power amplifier. The output current is used to drive the motor.

The wheel and the motor are both inside the hexagon vacuum chamber and the motor heats up rapidly and can be damaged. To reduce this effect, the mount holding the motor is cut away to expose over 90% of the motor surface area to facilitate heat radiation while still securing the motor. An Iron-Constantan thermocouple is held between the motor and the mount to monitor the temperature. Minimal driving power is used by adjusting the amplitude of the sinusoidal current that drives the motor, and monitoring the trigger signal during the adjustment to keep the motor running at 400 Hz. The power is turned on only during the time of collecting ATD data.

The nozzle orifice, the skimmer hole, the chopping slit in the wheel, and the tungsten filament have to lie on a straight line. This alignment is done using a Wild Heerbrugg KM-276 telescope. The open time of the shutter, or gate function $A(\lambda)$, is measured by a diode laser and a photomultiplier with the alkali source replaced by a diode laser. The tungsten filament in Figure 2.10 is removed and two pieces of shim stock are put very close together to form a slit to mimic the filament. The shims are taped outside on the window glass at the end of the flight tube. The laser light is detected by an Oriel photomultiplier. The chopper wheel spins at 400 Hz and the output current from the photomultiplier flows through a 500 Ω resistor. The voltage across the resistor is

Reproduced with permission of the copyright owner. Further reproduction prohibited without permission.

recorded by the Tektronix TDS 430A oscilloscope in the same fashion as the ATD signal being collected. The chopper wheel can be spun clockwise or counter clockwise; the resulting gate functions are almost identical. This is illustrated in Figure 2.11.

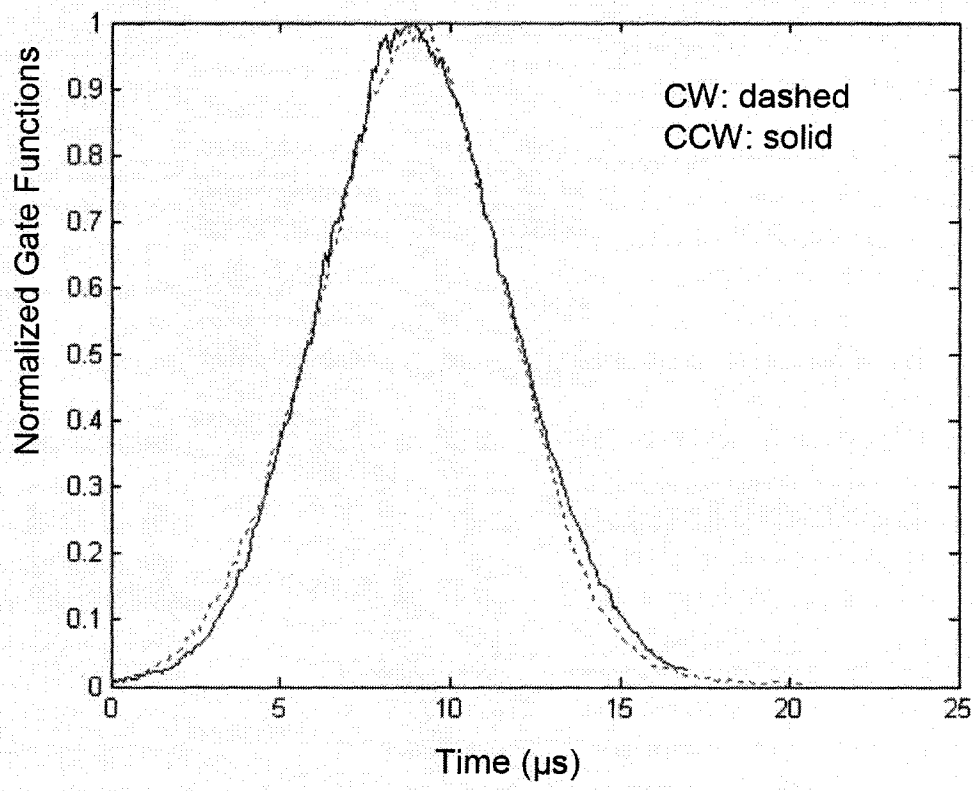

Figure 2.11 Normalized gate functions of the chopper wheel. The solid curve is the gate function measured when the wheel spins in a counter clockwise direction whereas the dashed one is for clockwise spin.

Reproduced with permission of the copyright owner. Further reproduction prohibited without permission.

2.6 Wiley-McLaren time-of-flight mass spectrometer

Time-of-flight (TOF) mass spectrometers are common tools to identify ions from collision ionization reactions. In our apparatus two identical Wiley-McLaren TOF mass spectrometers (WIL 55) are utilized to collect coincidence signals from the reaction between Rb and other molecules. The following is the working principle of a TOF mass spectrometer.

Two coupled Burle microchannel plates are used as ion detectors. The voltage across the plates is ~ 2000 V, which provides a gain of ~ 10^8 that allows one to detect very weak signals. The main task is to determine the mass. Figure 2.12 is the schematic structure of a typical TOF mass spectrometer. Ions are formed in the region around the ground potential. There is an accelerating field determined by the voltage V_A applied on the accelerator. After the accelerator there is a drift tube with voltage V_D, in between is a second accelerating field. Inside of the drift tube is a field free space.

Reproduced with permission of the copyright owner. Further reproduction prohibited without permission.

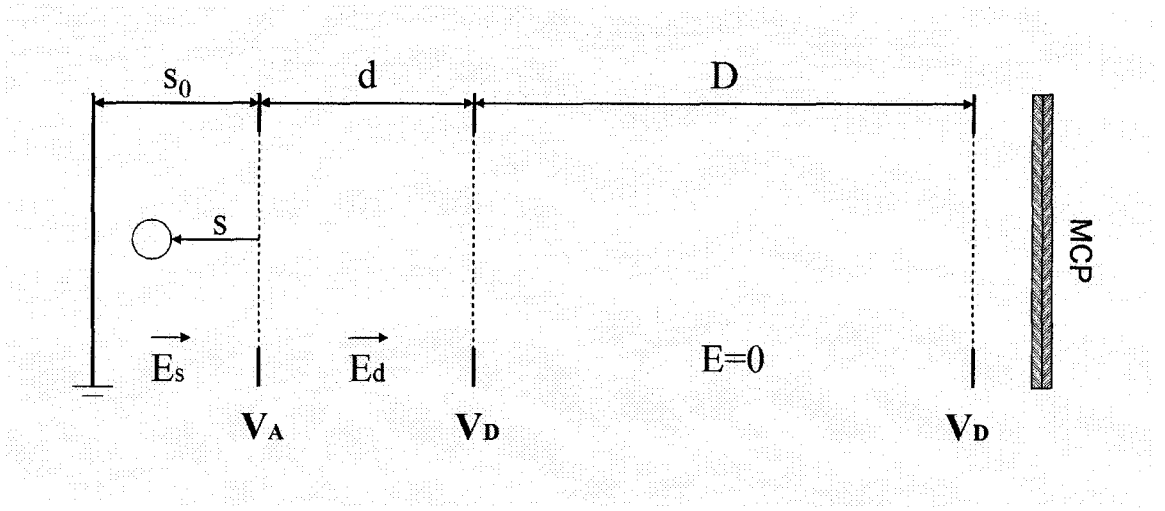

Figure 2.12 Schematic of a TOF mass spectrometer.

Ions are not formed in a single plane but have a space distribution. Despite the different initial locations of the ions, the mass spectrometer is able to resolve the masses. This is called space focusing. According to Figure 2.12 the time for an ion with mass m and charge q to travel from the ion source to the detector is

$$T(U_0, s) = T_s + T_d + T_D \tag{2.1}$$

where U_0 is the initial kinetic energy along the field direction, and s is the distance from the accelerator to the ion. When an ion leaves the drift tube its speed is very high and the distance between the drift tube and the detector is very small. Furthermore the ion will continue to accelerate toward the detector. Thus the time spent between the drift tube and the detector is very small compared to previous stages and not shown in equation (2.1). From basic mechanics one finds

$$T_s = 1.02\frac{\sqrt{2m}}{qE_s}\left[\sqrt{U_0 + qsE_s} \pm \sqrt{U_0}\right] \tag{2.2a}$$

Reproduced with permission of the copyright owner. Further reproduction prohibited without permission.

$$U = U_0 + qsE_s + qdE_d \tag{2.2b}$$

$$T_d = 1.02\frac{\sqrt{2m}}{qE_s}\left[\sqrt{U} - \sqrt{U_0 + qsE_s}\right] \tag{2.2c}$$

$$T_D = 1.02\frac{\sqrt{2m}\,D}{2\sqrt{U}} \tag{2.2d}$$

The units are cm for distances, V/cm for field strength, eV for energy, amu for mass, and μs for time. For optimal resolution

$$\frac{\partial T(U_0, s)}{\partial s} = 0 \tag{2.3}$$

As discussed previously U_0 is small, for space focusing let $U_0 = 0$. Suppose the average distance from the collision center to the accelerator is s_0, as shown in Figure 2.12, let $s = s_0$. Combine with the result from equation (2.3),

$$D = 2s_0k_0^{3/2}\left(1 - \frac{1}{k_0 + k_0^{1/2}}\frac{d}{s_0}\right) \tag{2.4}$$

where

$$k_0 = \frac{V_D}{V_A} \tag{2.5}$$

After the spectrometer is built the only adjustable factor in equation (2.4) is k_0. This result demonstrates that the optimal resolution for such a mass spectrometer is obtained either by solving equation (2.4) or empirically adjusting the ratio of the voltage on the accelerator to the drift tube. Equation (2.4) also indicates that the optimal resolution is mass independent! This is a great advantage for the experiments because a variety of ions are formed but only one sample is needed to tune the mass spectrometers. SF_6 is chosen as the standard gas due to the huge signal it gives.

Reproduced with permission of the copyright owner. Further reproduction prohibited without permission.

The physics of space focusing is that an ion initially closer to the detector (smaller s value) acquires less energy and is overtaken by ions further from the detector (bigger s value). This process is depicted in Figure 2.13.

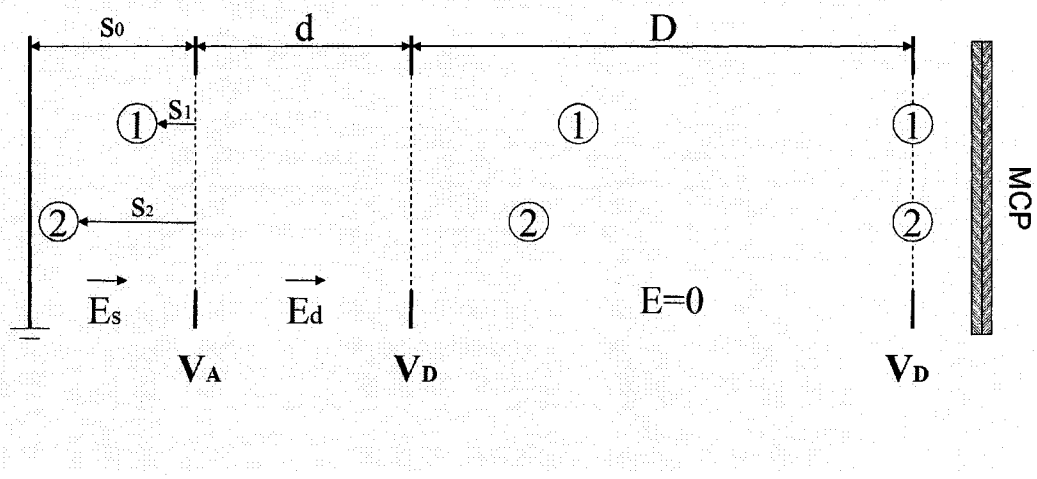

Figure 2.13 The process of space focusing. The initial position of ion 1 is closer to the detector than ion 2. But ion 2 acquires more energy ($qs_2E_s > qs_1E_s$) during the acceleration and eventually catches up ion 1 at the detector.

Ions also have different kinetic energies upon their formation because the input energy for collision ionization is not monoenergetic. To focus ions with different kinetic energies (energy focusing) an ion reflectron is usually used (MAM 73). In the machine being used however, the two spectrometers are perpendicular to the beam plane. Thus a velocity component of an ion along the field direction is small unless the impact parameter is very small and oriented along the spectrometer axes. Therefore energy focusing is not much of a concern and is not done.

Reproduced with permission of the copyright owner. Further reproduction prohibited without permission.

Chapter 3. Data Analysis

In order to investigate how the reactions change with energy and find the electron affinities of various negative ions, we need to know the speed distribution of the alkali beam and the gas beam. The former is extracted from the ATD and the latter is estimated by theory. Combining these two speed distributions leads to the energy distribution in the center of mass system. Fundamental kinetic theory is used to link the measured negative ion signals with the reaction cross section and the energy distribution. A computer program can then be used to fit the experimental data with the energy threshold as a parameter. From conservation of energy, the electron affinities of the product negative ions are found. This chapter shows in detail how the data are treated according to the above procedure.

3.1 Deconvolution of Arrival Time Distribution

The speed distribution of the supersonic Rb beam is given by

$$F_1(v) = B_1 f_1(v) = B_1 v^2 \exp\left[-\left(\frac{v - v_0}{\Delta v}\right)^2\right] \tag{3.1}$$

where B_1 is the normalization constant, v_0 is the stream velocity of the expansion, and Δv a measure of the deviation from the stream velocity (PAU 00). The translational temperature is given by $T = \frac{m(\Delta v)^2}{2k}$, where m is the mass of the atom and k is Boltzmann's constant. This distribution is characterized by only two parameters v_0 and Δv.

Reproduced with permission of the copyright owner. Further reproduction prohibited without permission.

How is the ATD related to the speed distribution? The surface ionization detector is sensitive to the flux distribution of the beam, which is *vf(v)*. Let's define the time zero to be the moment when the first atom passes through the slit. At time *t*, only those atoms whose speeds satisfy equation (3.2) will arrive at the detector.

$$v(\lambda)=\frac{L}{t-\lambda} \tag{3.2}$$

where λ is the open time of the slit and $\lambda \leq t$, L is the distance from the chopper to the detector. The instantaneous flux on the detector at time t will be

$$N(t)=\int_{\frac{L}{t}}^{\infty} A(\lambda) n v f(v)\, dv \tag{3.3}$$

where $A(\lambda)$ is the gate function and n the number density of the beam. Substitute (3.1) and (3.2) into (3.3) and change t to μ, we have

$$N(\mu)=C_1 \int_0^{\mu} \frac{L^4}{(\mu-\lambda)^5} A(\lambda) \exp[-(\frac{L}{(\mu-\lambda)\Delta v}-\frac{v_0}{\Delta v})^2]d\lambda \tag{3.4}$$

The detector and the circuit have a response function that delays and broadens the signal and this function is usually an exponential decay. Taking this into account the observed ATD is

$$y(t)=C_2 \int \exp\left(-\frac{t-\mu}{\tau}\right) N(\mu)d\mu \tag{3.5}$$

where τ is called the response time. We can see that the ATD is a convolution of the speed distribution, the gate function of the chopper wheel and the response function (ALC 69).

The task now is to extract the speed distribution out of the ATD. The response time τ is calculated from the tail of the ATD signal (ALC 69, YOU 73) simply using

Reproduced with permission of the copyright owner. Further reproduction prohibited without permission.

$$\ln[y(t)]_{tail} = -\frac{t}{\tau} + C \tag{3.6}$$

Figure 3.1 shows an example. The value of τ depends on the detector's characteristic time and the electronics characteristic time. It is usually between 15~25 μs for the current setting.

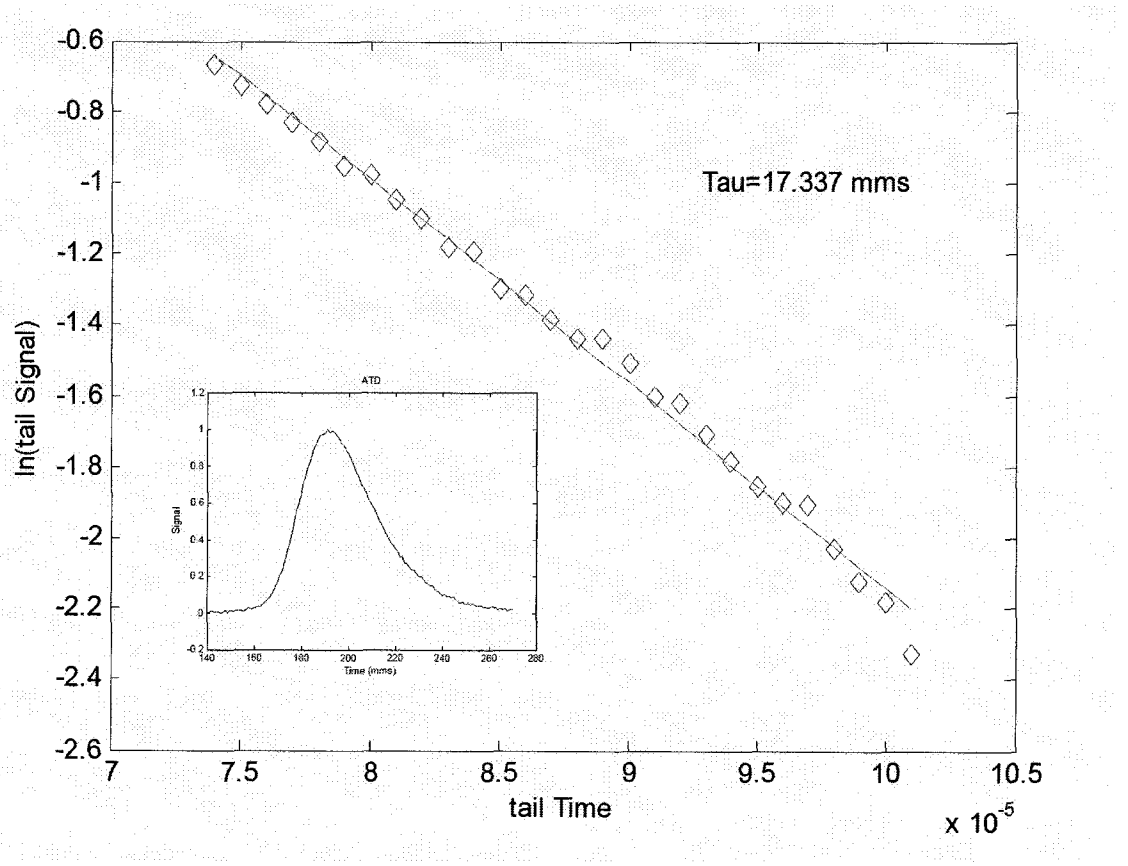

Figure 3.1 Logarithm of the ATD tail signal vs. time. The slope is $-1/\tau$. The inset is the ATD signal that the line is based on. The diamonds are experimental values. The straight line going through them is the least square fitting line.

Reproduced with permission of the copyright owner. Further reproduction prohibited without permission.

The optimal values of v_0 and Δv are found by the Marquardt nonlinear least square method (BEV 03). A Matlab program is written based on this method (for details please refer to Appendix I). Figure 3.2 is a typical fit of the ATD. The agreement is excellent in virtually every case and Figure 3.2 is truly *typical*.

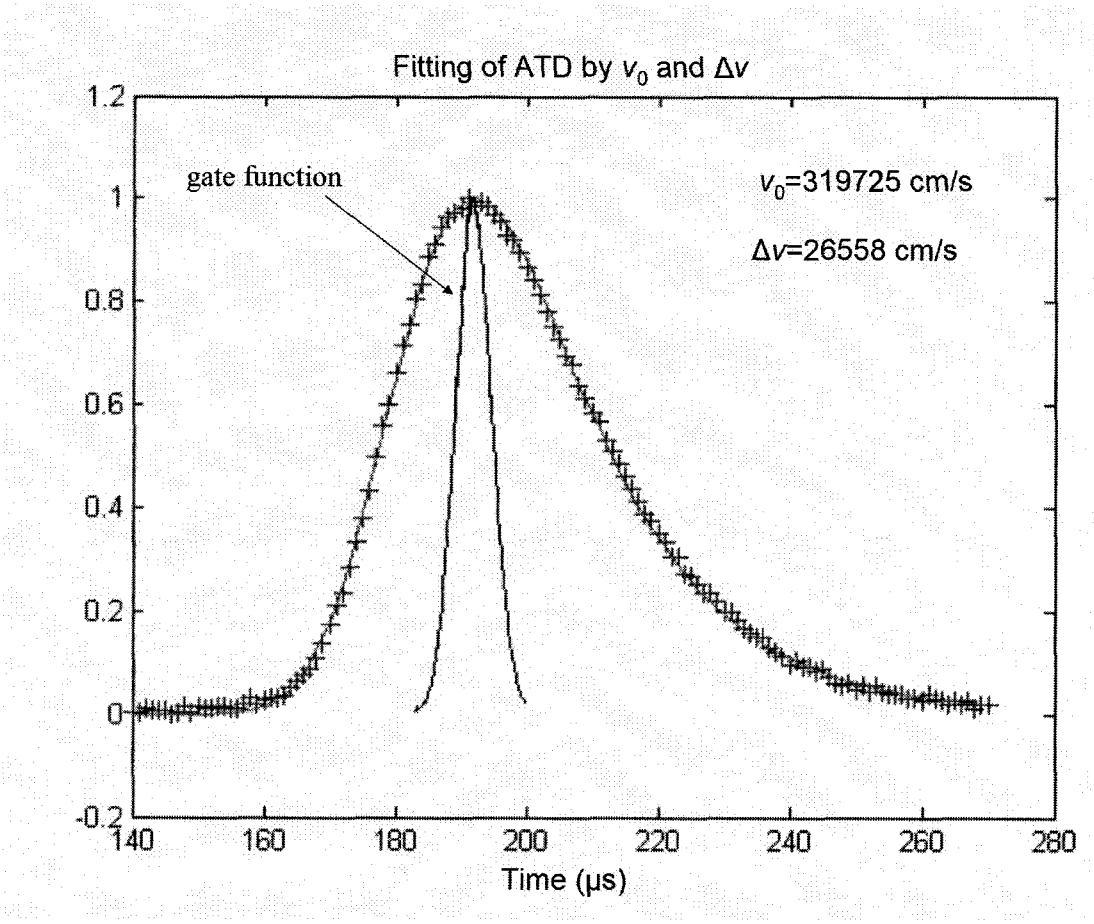

Figure 3.2 Fit of the ATD by two parameters v_0 and Δv. The "+" are experimental points and the smooth curve going through them is the fit. The gate function of the chopper wheel is also drawn for comparison, showing how the ATD would look like if the beam were monoenergetic and the detector response were instantaneous.

Reproduced with permission of the copyright owner. Further reproduction prohibited without permission.

3.2 Energy Distribution

The major part of the collision energy comes from the Rb beam because the Rb oven and nozzle are heated and the atoms are seeded in H_2 whereas the gas beam is at room temperature and seeded in He or Ar. The speed distribution of the Rb beam is measured as described above. Since the model fits the data very well, it is reasonable to assume that the gas beam speed distribution has the same form as the Rb beam, which is

$$F_2(v) = B_2 f_2(s) = B_2 s^2 \exp\left[-\left(\frac{s - s_0}{\Delta s}\right)^2\right] \tag{3.7}$$

For an isentropic expansion the kinetic energy of a molecule is (ABU 67)

$$\frac{1}{2} m_h s_0^{\,2} = \frac{m_h}{\overline{m}} \int_0^{T_0} \overline{C}_p dT \tag{3.8}$$

where m_h is the mass of the heavy molecule, s_0 is the speed, $\overline{m}$ is the average mass of the beam, T_0 is the temperature of the nozzle, and $\overline{C}_p$ is the average heat capacity of the beam. It is assumed that the molecules are rotationally but not vibrationally cooled, but even if a few degrees of freedom for vibration are cooled, we have found that effect on the final results is very small. Equation (3.8) actually gives the upper limit of the gas beam energy assuming the seed molecules are traveling at the same speed of the carrier gas. The average speed ratio $v_0/\Delta v$ of the Rb beam is about 10. Since both beams are supersonic the speed ratio of the gas beam $s_0/\Delta s$ is chosen to be 10 and s spreads within $\pm 3\Delta s$ with respect to s_0. This speed extent covers over 99% of the gas molecules and a wider range of the speed does not affect the final results.

Reproduced with permission of the copyright owner. Further reproduction prohibited without permission.

We can now combine these two distributions to find the relative speed distribution. This is best discussed in terms of the Newton diagram of the velocities of the colliding pair as illustrated in Figure 3.3.

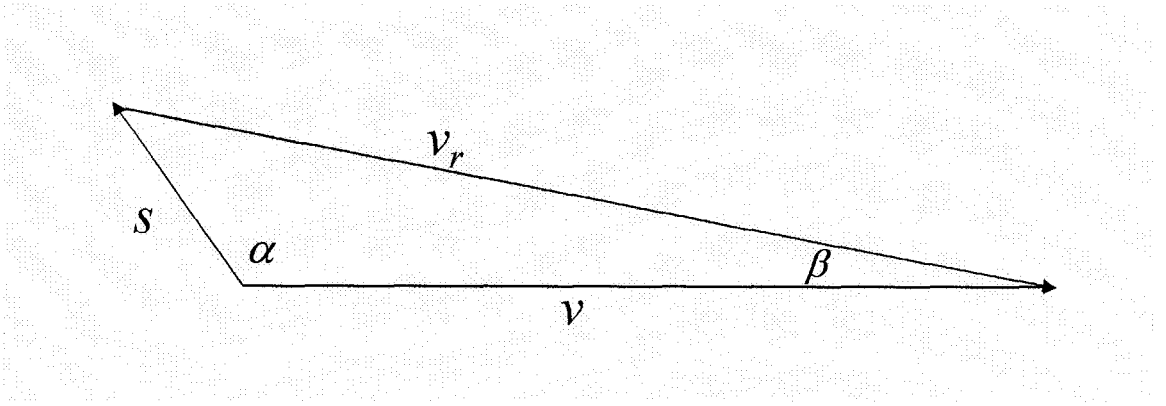

Figure 3.3 Newton diagram for the collision between a Rb atom and a gas molecule.

Here v is the speed of a Rb atom, s is the speed of a gas molecule, $\alpha = 120^{\circ}$ is the angle between these two beams, v_r is the relative speed, and β is the angle between v and v_r. It was shown (DAT 61) that

$$\begin{aligned} v &= v_r \sin(\alpha+\beta)/\sin\alpha \\ s &= v_r \sin\beta/\sin\alpha \\ dsdv &= \frac{v_r}{\sin\alpha} dv_r d\beta \\ \alpha &= \frac{2\pi}{3} \\ 0 &\le \beta \le \pi - \alpha \end{aligned} \tag{3.9}$$

Thus β ranges from 0 to $\pi/3$ according to the relative magnitude of s and v. It is an indication of the direction of the relative velocity. The relative velocity distribution $g(v_r,\beta)$ must satisfy equation

Reproduced with permission of the copyright owner. Further reproduction prohibited without permission.

$$f_1(v)f_2(s)dsdv = g(v_r,\beta)dv_r d\beta \tag{3.10}$$

In our experiments however, only the magnitude of v_r is important. So we can integrate over β and find the relative speed distribution

$$f(v_r) = \int_0^{\pi/3} g(v_r,\beta)d\beta \tag{3.11}$$

Substitute (3.1), (3.7), (3.9) and (3.10) into (3.11), after rearrangement one finds

$$f(v_r) = \left(\frac{v_r}{\sin\alpha}\right)^5 \int_0^{\pi/3} \sin^2(\alpha+\beta)\sin^2\beta \exp\left[-\left(\Omega^2 v_r^{\,2} - \Phi v_r + \Gamma\right)\right]d\beta \tag{3.12}$$

where

$$\begin{aligned}
&\left(\frac{v-v_0}{\Delta v}\right)^2 + \left(\frac{s-s_0}{\Delta s}\right)^2 = \Omega^2 v_r^{\,2} - \Phi v_r + \Gamma \\
&\Omega^2 = \left(\frac{\sin^2(\alpha+\beta)}{(\Delta v)^2} + \frac{\sin^2\beta}{(\Delta s)^2}\right)\frac{1}{\sin^2\alpha} \\
&\Phi = 2\left(\frac{v_0\sin(\alpha+\beta)}{(\Delta v)^2} + \frac{s_0\sin\beta}{(\Delta s)^2}\right)\frac{1}{\sin\alpha} \\
&\Gamma = \left(\frac{v_0}{\Delta v}\right)^2 + \left(\frac{s_0}{\Delta s}\right)^2
\end{aligned} \tag{3.13}$$

The energy distribution of the reaction is related to the speed distribution by

$$h(E)dE = f(v_r)dv_r \tag{3.14}$$

Since $E = \frac{1}{2}\mu v_r^2$, we have

$$h(E) = \frac{f(v_r)}{\mu v_r} \tag{3.15}$$

Reproduced with permission of the copyright owner. Further reproduction prohibited without permission.

3.3 Determination of Reaction Thresholds

We start from basic kinetic theory of chemical reactions. For a two particle collision, the rate of production (#/sec/cc) is

$$R = k\, n^t_1\, n^t_2 \tag{3.16}$$

where k is the rate constant, n^t_1 is the number density of beam one and n^t_2 is for beam two. The rate of production (#/sec) in the crossed beam volume V is

$$S = RV = V k\, n^t_1\, n^t_2 \tag{3.17}$$

The rate constant depends on relative speed v_r or collision energy $E = \frac{1}{2}\mu v_r^2$ by $k = v_r \sigma(E)$, where $\sigma(E)$ is the cross section of the reaction. Since there is a speed distribution for both beams, the number of atoms between v and $v + dv$ is $dn_1(v) = n_1{}^t B_1 f_1(v) dv$, and the number of molecules between s and $s + ds$ is $dn_2(s) = n_2{}^t B_2 f_2(s) ds$. The corresponding signal will be

$$\begin{aligned} d^2S &= V dn_1(v) dn_2(s) v_r \sigma(E) \\ &= V B_1 B_2 n_1{}^t n_2{}^t v_r \sigma(E) f_1(v) f_2(s) ds dv \end{aligned} \tag{3.18}$$

The backing pressure of the gas beam is kept constant, so B_2 and n^t_2 are constant for a particular gas sample. The crossing volume V is also assumed to be a constant, then

$$S = V B_1 B_2 n_1{}^t n_2{}^t \int\int v_r \sigma(E) f_1(v) f_2(s) ds dv \tag{3.19}$$

Substitute (3.10) and (3.11) into (3.19),

$$S = V B_1 B_2 n_1{}^t n_2{}^t \int_0^\infty v_r \sigma(E) f(v_r) dv_r \tag{3.20}$$

As mentioned before the ATD signal is sensitive to the flux of the Rb beam,

Reproduced with permission of the copyright owner. Further reproduction prohibited without permission.

$S_{ATD} = \int V(t)dt = C_A B_1 n_1^t \int v f_1(v)dv$, $V(t)$ is the original ATD signal (voltage vs. time), C_A is some proportional constant. From this equation, we have $B_1 n_1^t = \frac{S_{ATD}}{C_A \int v f_1(v)dv}$.

Substituting into (3.20),

$$S = \frac{VB_2 n_2^t}{C_A} \frac{S_{ATD}}{\int v f_1(v)dv} \int_0^\infty v_r \sigma(E) f(v_r) dv_r = N \frac{S_{ATD}}{\int v f_1(v)dv} \int_0^\infty v_r \sigma(E) f(v_r) dv_r \qquad (3.21)$$

In this equation there are only two unknowns N and $\sigma(E)$.

It was suggested by Wigner (WIG 48)that for the production of parent negative ions near thresholds, i.e. Rb + M → Rb^+ + M^-, the cross section is a step function of energy

$$\sigma(E) = \begin{cases} 0 & E < Th \\ \sigma_0 & E \geq Th \end{cases} \qquad (3.22)$$

For the production of three particles, two of which have equal but unlike charges, this cross section can be modified to (HAR 57)

$$\sigma(E) = \begin{cases} 0 & E < Th \\ \sigma_0 (E - Th)^{3/2} & E \geq Th \end{cases} \qquad (3.23)$$

Th stands for the reaction threshold. Now there are two unknown parameters $N\sigma_0$ and Th in (3.21). A Matlab program was written to fit the experimental signal by adjusting these two unknowns (for details please refer to Appendix II).

According to the conservation of energy, Th = IP + BDE - EA, where IP is the ionization potential of Rb, BDE is the bond dissociation energy, and EA is the electron affinity of the product negative ion. The IP of all alkali metals are well known. So we can determine the BDE or EA from this equation if any one of them is known.

Reproduced with permission of the copyright owner. Further reproduction prohibited without permission.

Chapter 4. Results and Discussion

4.1 C_2F_5Cl and C_2F_5I

A mixture of C_2F_5Cl (10%) and He (90%) is required to obtain reasonable magnitude coincidence signals. For C_2F_5I a 10% mixture in He gives huge signals that confuse the coincidence detection even at low energies. After diluting the samples a few times, we found a 0.032% of C_2F_5I in Ar optimal. During the experiments, the pressure of the gas mixture behind the nozzle is held constant at 250 torr by an automatic pressure valve and a controller to ensure a supersonic flow and maintain a reasonable vacuum. The reaction energy is adjusted by changing the backing pressure of the Rb beam. The temperature of the Rb oven is ~220 °C and nozzle is ~770 °C.

Figure 4.1 is a coincidence mass spectrum of C_2F_5Cl at low energy and Figure 4.2 is the same molecule at high energy. The negative ions formed by Rb and C_2F_5Cl are Cl^-, CF_3^- and $C_2F_5^-$. The corresponding reactions are

$$Rb + C_2F_5Cl \rightarrow Rb^+ + Cl^- + C_2F_5 \quad (4.1)$$

$$Rb + C_2F_5Cl \rightarrow Rb^+ + Cl + C_2F_5^- \quad (4.2)$$

$$Rb + C_2F_5Cl \rightarrow Rb^+ + CF_3^- + CF_2Cl \quad (4.3)$$

The double peak of $C_2F_5^-$ reflects the Rb^+ ion isotopes at m/e=85 and 87, which account for 72% and 28% of the element and give different start pulses in the coincidence technique. Thus the Cl^- peak should be quartet (Cl^- has m/e=35 and 37) but two of the peaks strongly overlap and we are able to resolve only three. The mass scale has been calibrated with several gases such as CF_3Br and SF_6. The peak Z around mass 80

Reproduced with permission of the copyright owner. Further reproduction prohibited without permission.

corresponds to $\Delta t = 0$ and is called "zero time peak". We believe it is an artifact caused by a Rb^+ hitting the edge of a pore in the MCP and ejecting an electron backward to the negative ion detector. Because the electron moves so quickly, it is detected almost simultaneously with the positive ion and a peak appears at zero time difference.

At low energies $C_2F_5^-$ is the major product. As energy goes up the $C_2F_5^-$ intensity increases very slightly, but Cl^- intensity increases dramatically and becomes the major product, suggesting that Cl^- has a higher threshold than $C_2F_5^-$.

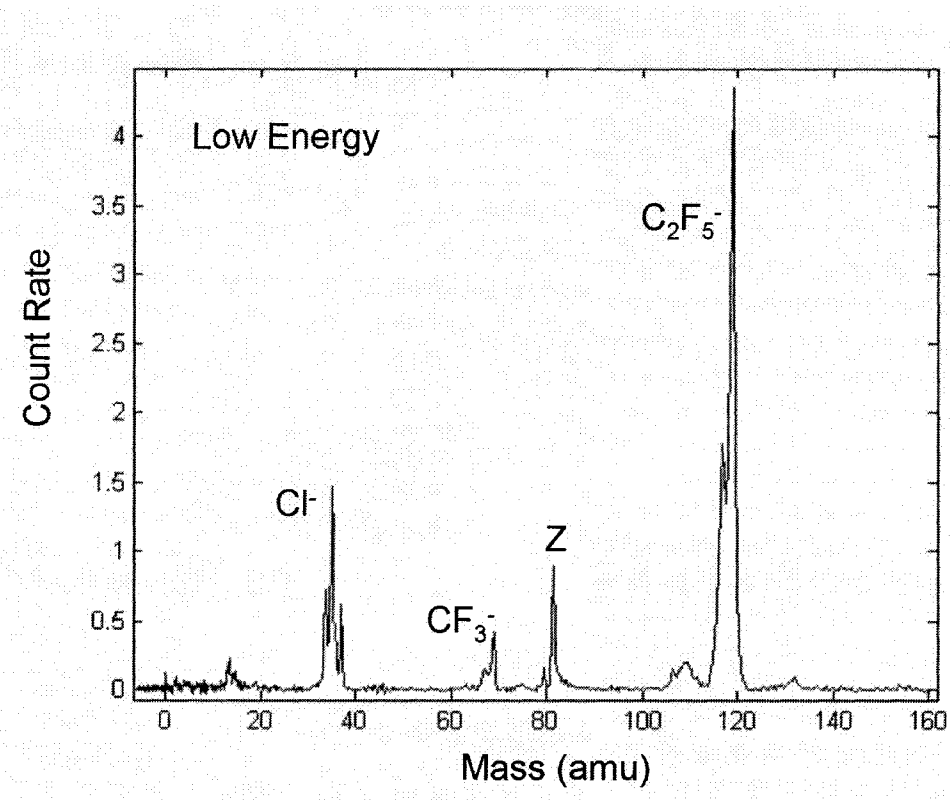

Figure 4.1 Coincidence time of flight mass spectrum showing negative ions formed by electron transfer to C_2F_5Cl at low energy.

Reproduced with permission of the copyright owner. Further reproduction prohibited without permission.

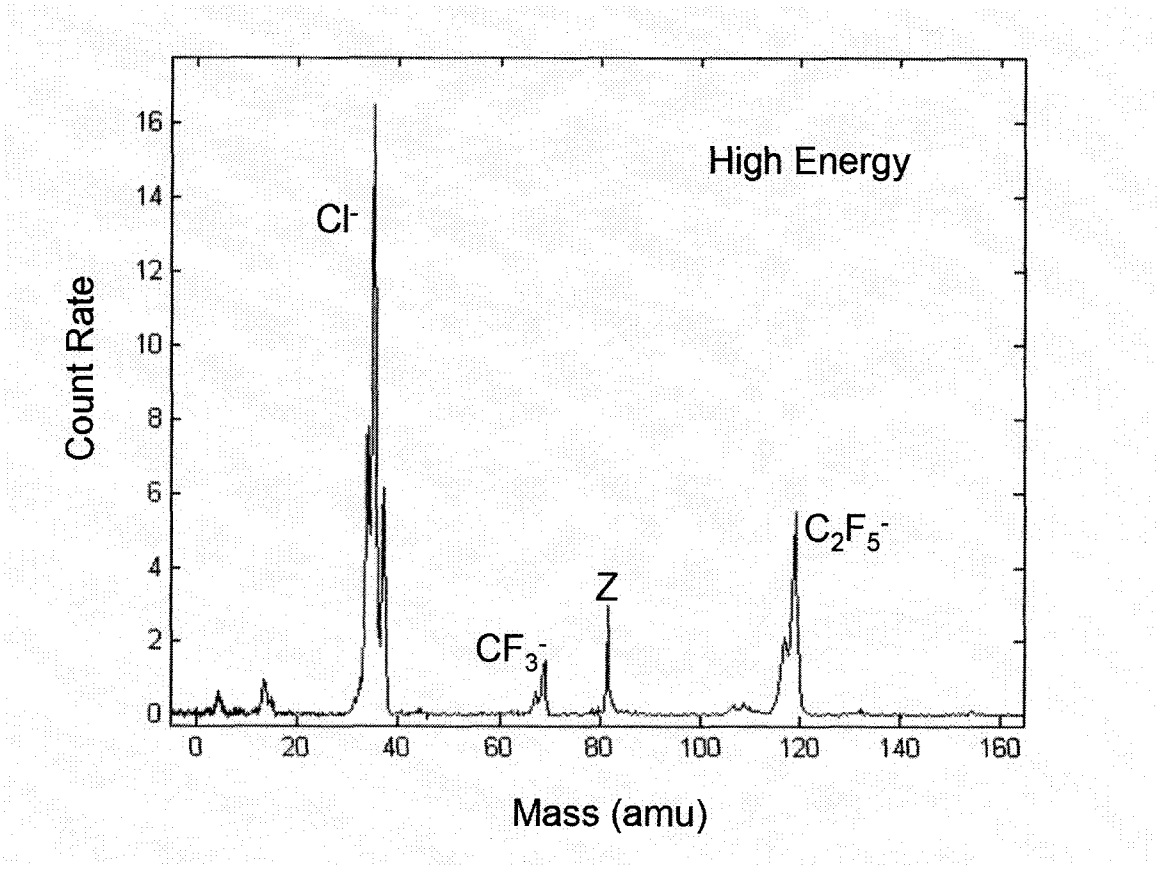

Figure 4.2 Coincidence time of flight mass spectrum showing negative ions formed by electron transfer to C_2F_5Cl at high energy.

Reproduced with permission of the copyright owner. Further reproduction prohibited without permission.

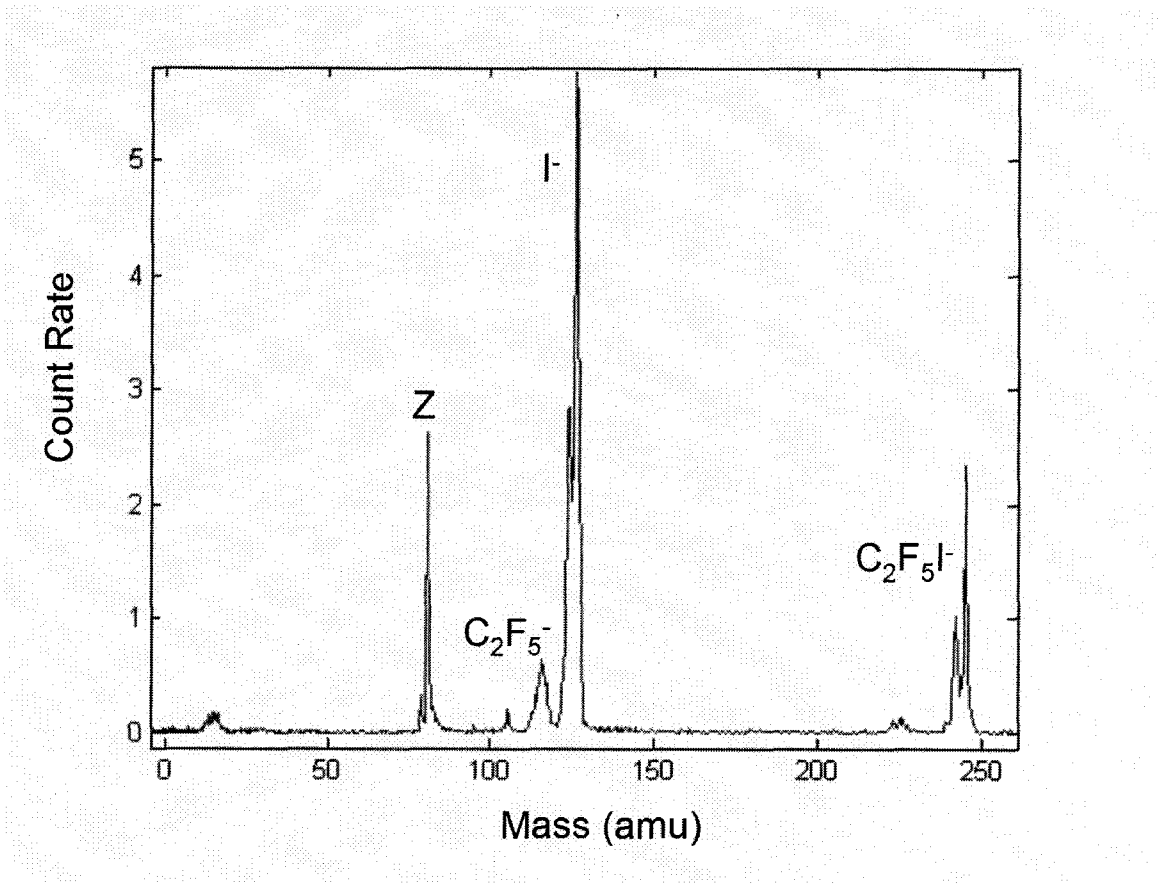

Figure 4.3 Coincidence time of flight mass spectrum showing negative ions formed by electron transfer to C_2F_5I.

The mass spectrum of C_2F_5I is shown in Figure 4.3. The pattern does not change with energy so one spectrum is enough to represent the result. The situation is different from that of C_2F_5Cl. The major product is always I^- and the parent ion $C_2F_5I^-$ is observed. The $C_2F_5^-$ intensity is much lower than that of I^-. $C_2F_5^-$ seems to have about the same threshold as that of I^-. The associated reactions are

$$Rb + C_2F_5I \rightarrow Rb^+ + I + C_2F_5^- \qquad (4.4)$$

Reproduced with permission of the copyright owner. Further reproduction prohibited without permission.

$$Rb + C_2F_5I \rightarrow Rb^+ + I^- + C_2F_5 \quad (4.5)$$

$$Rb + C_2F_5I \rightarrow Rb^+ + C_2F_5I^- \quad (4.6)$$

We follow the procedure described in Chapter 3 to fit the data of C_2F_5Cl and C_2F_5I to find the reaction thresholds of forming $C_2F_5^-$, Cl^-, I^- and $C_2F_5I^-$. The CF_3^- signal is too low to analyze.

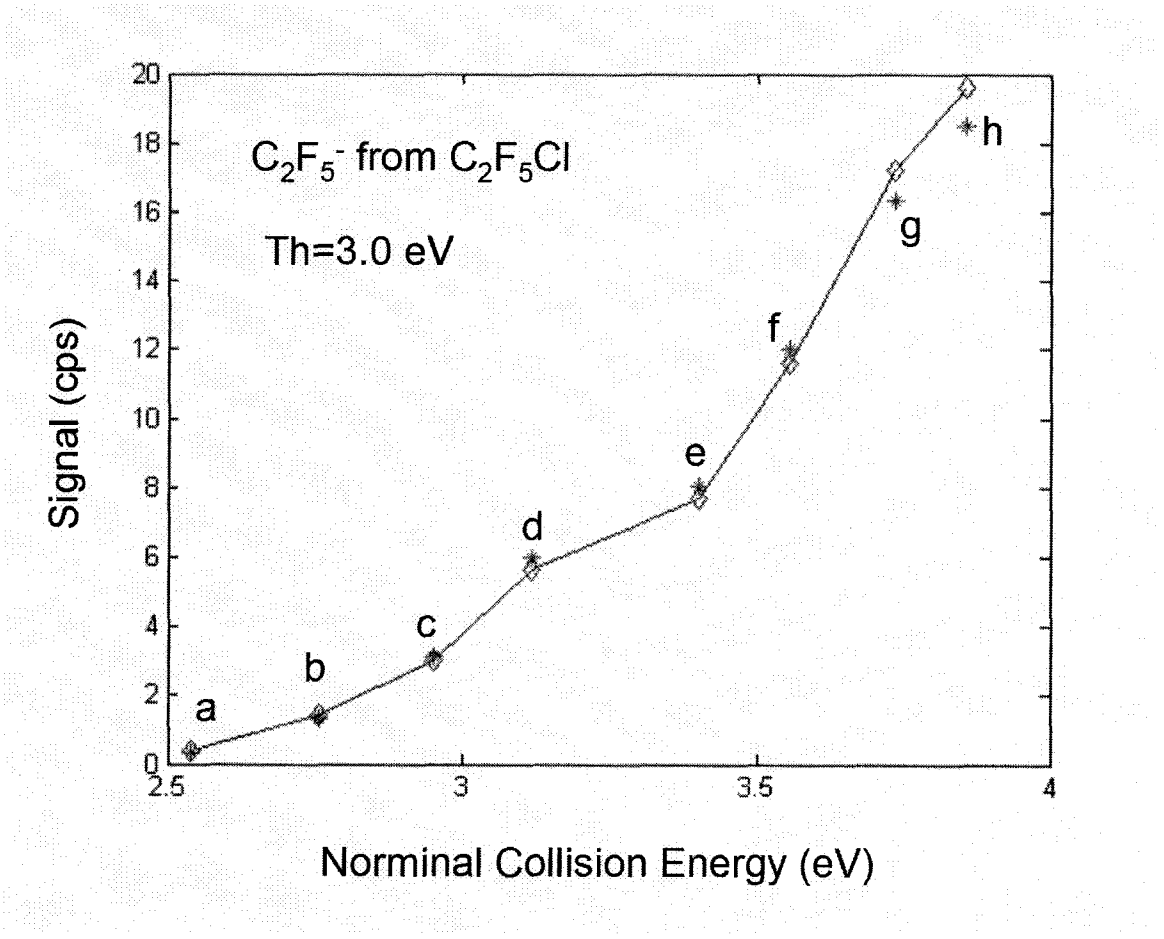

Figure 4.4 Signal of $C_2F_5^-$ arising from collisions of Rb and C_2F_5Cl at various nominal energy conditions. The stars are experimental data and the diamonds are calculated from best fit parameters. The line connects the points and guide eyes.

Reproduced with permission of the copyright owner. Further reproduction prohibited without permission.

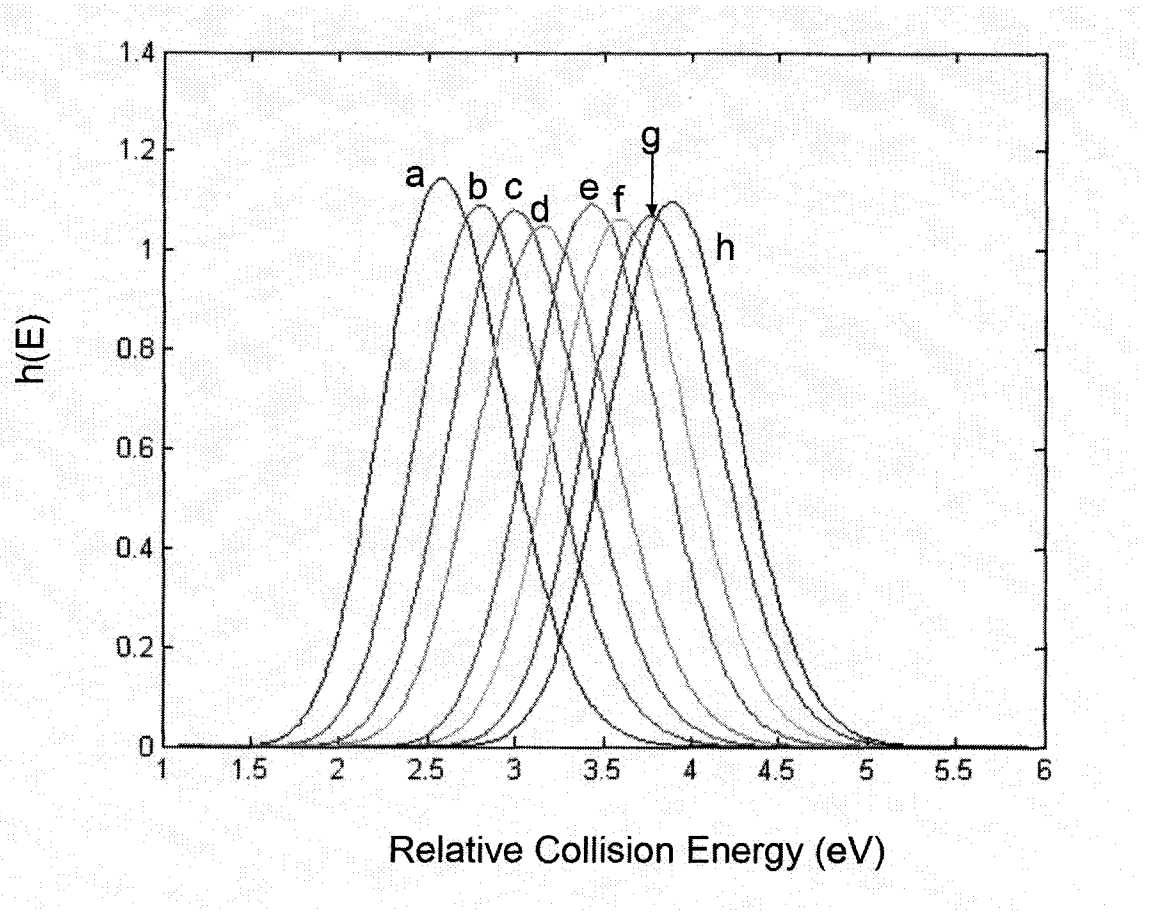

Figure 4.5 Relative collision energy distributions calculated from the speed distribution parameters obtained from the arrival time distributions of Rb beam. The speed distribution of the gas beam is assumed to be given by equation (3.7).

In Figure 4.4 the experimental data and calculated values are shown together. The calculation is based on equation (3.21) and (3.23)with two adjustable parameters Th and N. The best fit threshold is found to be 3.0 eV for the formation of $C_2F_5^-$ from the collisions between Rb and C_2F_5Cl. The energy distribution of *each* point in Figure 4.4 is shown in Figure 4.5. One may notice that in Figure 4.4 there are three data points (a, b and c) below 3.0 eV. This is understandable from Figure 4.5 which shows that in the first

Reproduced with permission of the copyright owner. Further reproduction prohibited without permission.

three curves (a, b and c) there is a fraction of collisions whose energies are greater than 3.0 eV. This fraction lies in the right wings (high energy part) of the distribution curves.

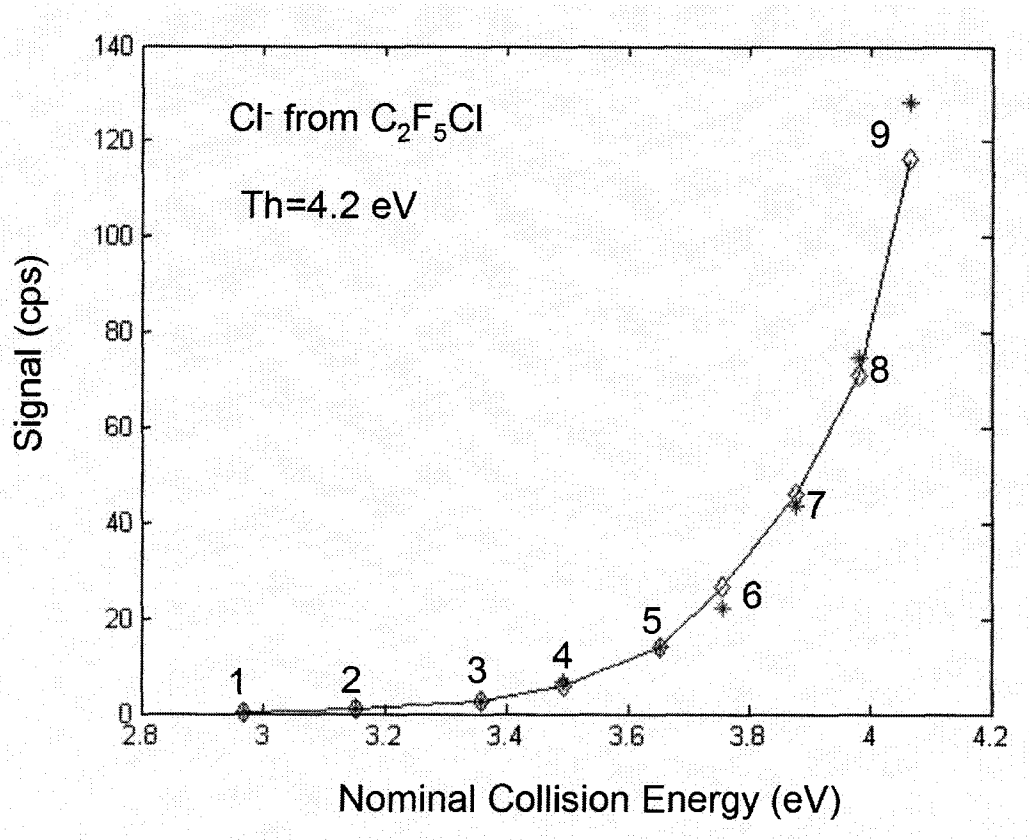

Figure 4.6 Experimental signals for Cl^- from C_2F_5Cl and the best fit.

Reproduced with permission of the copyright owner. Further reproduction prohibited without permission.

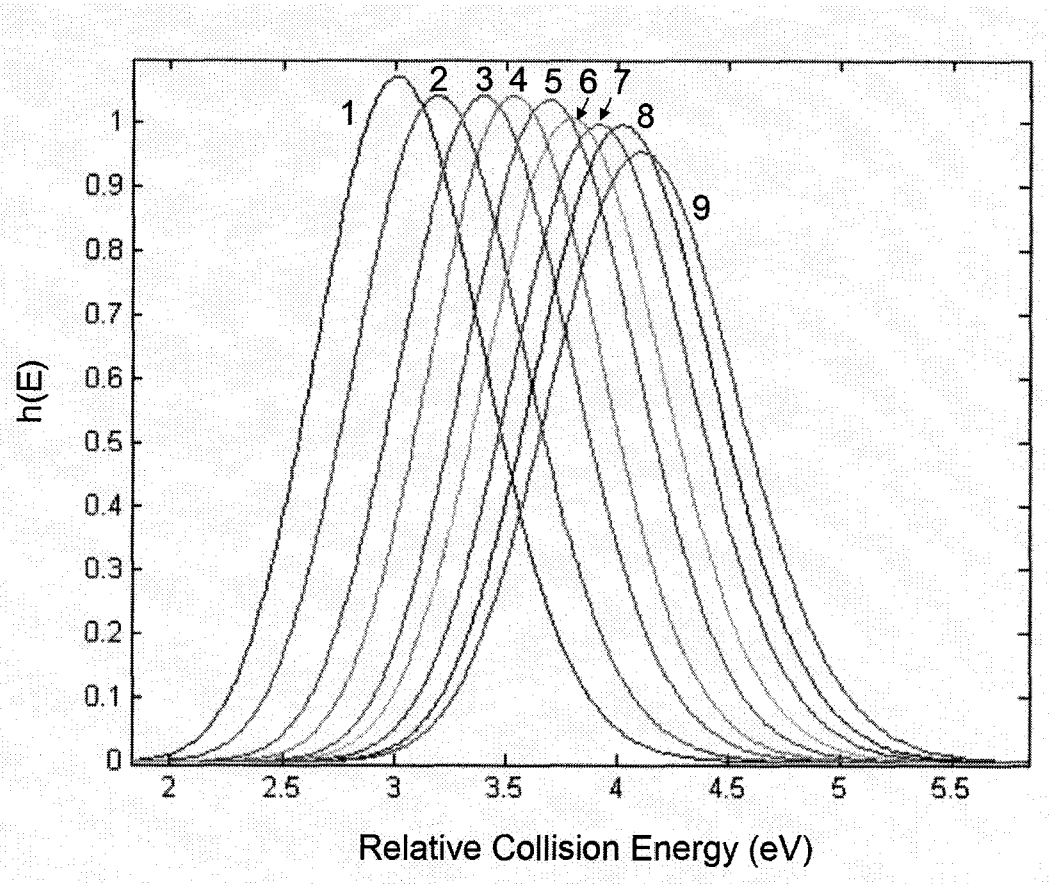

Figure 4.7 Relative energy distributions for the collisions between Rb and C_2F_5Cl to produce Cl^-.

Similarly the results of Cl^- from C_2F_5Cl are shown in Figure 4.6 and 4.7. For the first few curves (1 and 2 for example) in Figure 4.7 only a small portion (tail) of the collisions have energies greater than 4.2 eV and are reactive. This part is not very accurately measured compared to other high energy curves because it comes from the tail of the arrival time distribution. Consequently some very low energy points are already eliminated before the fitting because the energy distributions above the threshold are not well know. At energies much higher than the thresholds the excitation functions

Reproduced with permission of the copyright owner. Further reproduction prohibited without permission.

(equations 3.22 and 3.23) are no longer valid, and these points are also excluded. We use these two rules to select all the data that have been collected. Most of the data points are good for analysis, for example, all the points in Figure 4.6 and curves in Figure 4.7 are included.

Figure 4.8 to 4.11 are the results of I-, $C_2F_5^-$ and $C_2F_5I^-$ from the collisions between Rb and C_2F_5I. There are 11 data points. For $C_2F_5I^-$ only the first 7 points are used.

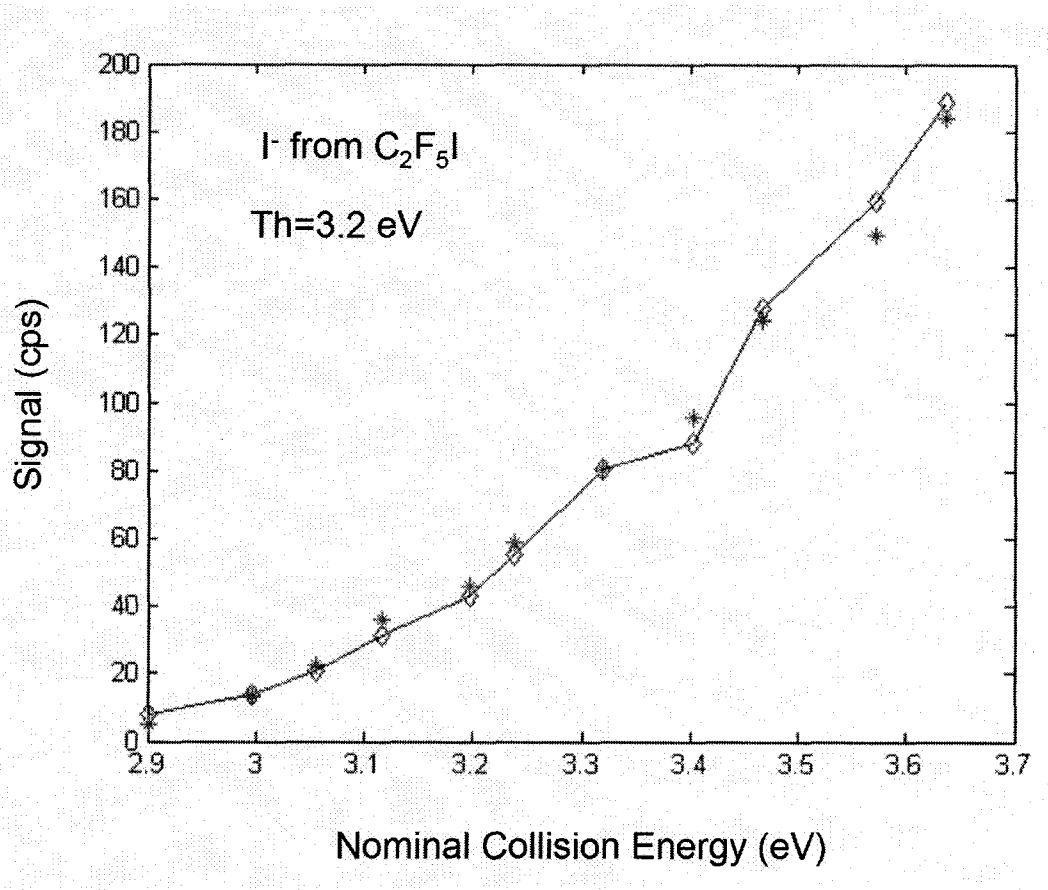

Figure 4.8 Experimental signals for I^- from C_2F_5I and the best fit.

Reproduced with permission of the copyright owner. Further reproduction prohibited without permission.

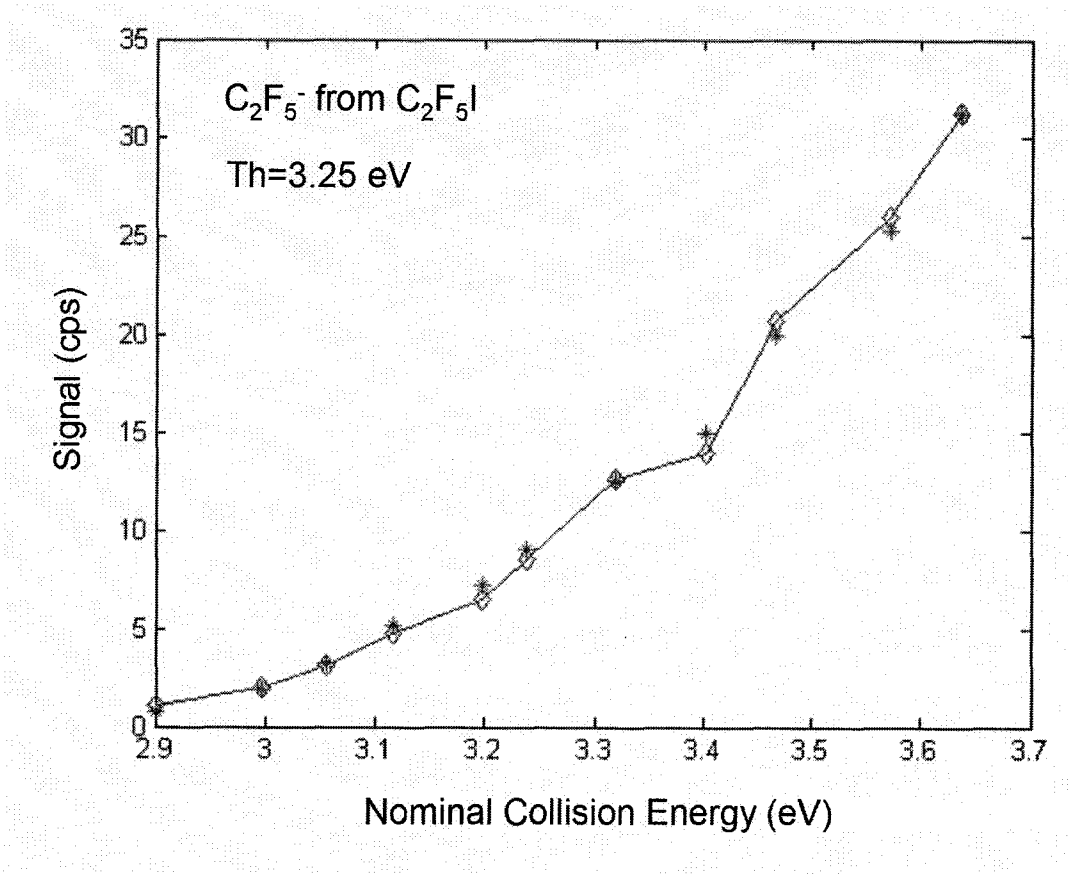

Figure 4.9 Experimental signals for $C_2F_5^-$ from C_2F_5I and the best fit.

Reproduced with permission of the copyright owner. Further reproduction prohibited without permission.

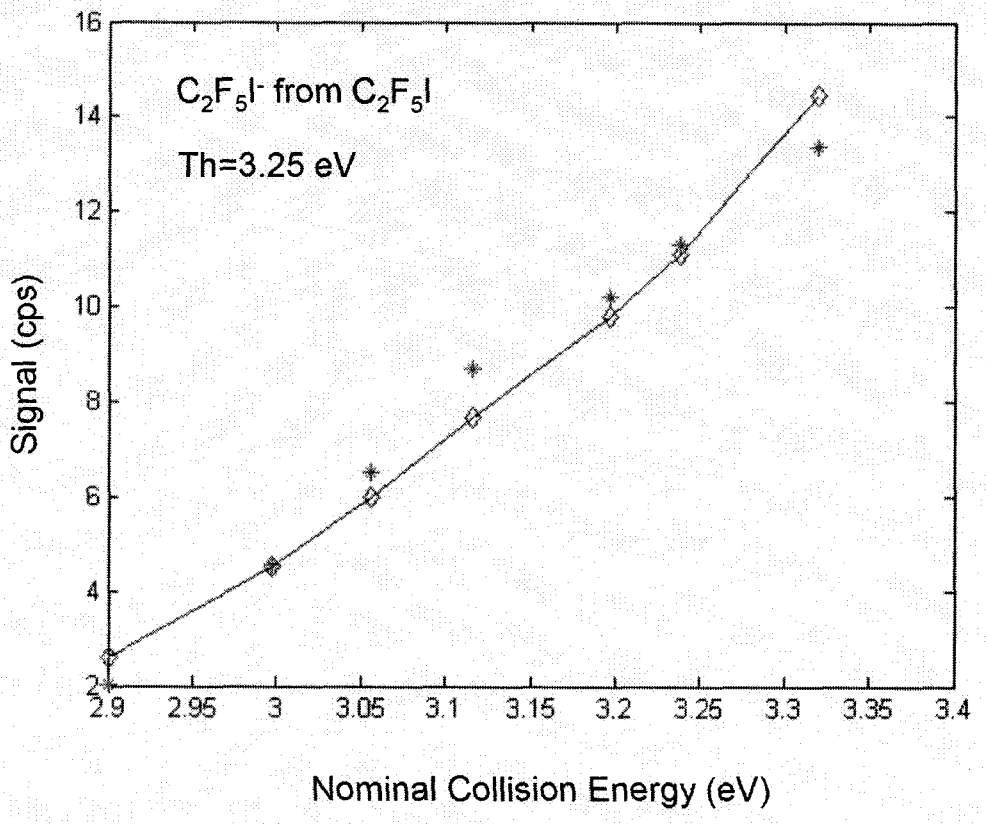

Figure 4.10 Experimental signals for $C_2F_5I^-$ from C_2F_5I and the best fit.

Reproduced with permission of the copyright owner. Further reproduction prohibited without permission.

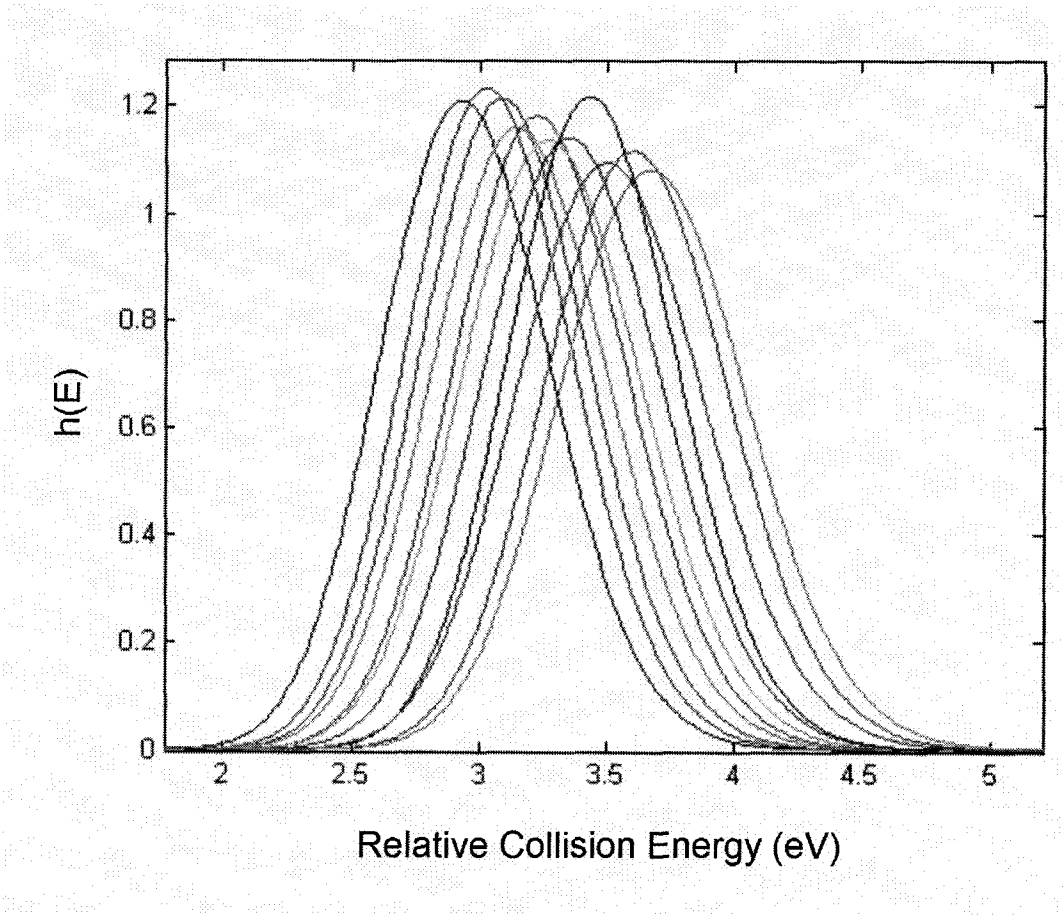

Figure 4.11 Relative energy distributions for the collisions between Rb and C_2F_5I.

Reproduced with permission of the copyright owner. Further reproduction prohibited without permission.

The experiments for both C_2F_5Cl and C_2F_5I were repeated several times although the energy range in a given experiment was sometimes optimized only for one ion. Similar experiments are done on test gases such as CF_3Br and SF_6. These are summarized in Table 4.1. Columns 3 and 4 are results from the current work, and column 5 is from the literature.

Table 4.1 Measured thresholds[a]

molecule	ion	threshold (eV)	EA(eV)	EA(eV) lit.
CF_3Br	Br^-	≈3.13±0.1	≈ 4.12	3.37
	CF_3Br^-	3.25±0.08	0.93	0.91
SF_6	SF_6^-	3.80	0.48	0.3-1.2
C_2F_5Cl	Cl^-	4.27±0.11	3.47 [b]	3.61
	$C_2F_5^-$	2.93±0.08	4.84 [b]	≈2
C_2F_5I	I^-	3.13±0.08	3.27[c]	3.06
	$C_2F_5^-$	3.20±0.09	3.20[c]	≈2
	$C_2F_5I^-$	3.22±0.03	0.96	--

a) IP(Rb) = 4.18 (NIS 03) b) BDE(C-Cl) ≈ 3.95 (MCM 82) c) BDE(C-I) ≈ 2.22 (MCM 82) d) BDE(C-Br) ≈ 3.06 (MCM 82)

(Literature values for EA's are from NIS 03)

As mentioned previously the electron affinities (EA) in Table 4.1 are calculated from the equation Th = IP+BDE-EA, where Th is the energetic threshold for ion-pair

Reproduced with permission of the copyright owner. Further reproduction prohibited without permission.

formation, and BDE is the dissociation energy of any chemical bonds which must be broken to form the negative ion. Just after the electron is transferred, the incipient negative ion is likely to be formed in an excited state via a Franck-Condon process in which the electron is attached to the molecule in a time much less than that required for the nuclei to move to their (new) equilibrium positions.

Most of the electron affinities listed in Table 4.1 are in reasonably good agreement with literature values, except for Br and C_2F_5. The electron affinity of C_2F_5I has apparently not been previously measured.

The discrepancy between our value for Br^- and the better established literature value arises because the mass peaks for Br^- (m/e = 79 and 81) strongly overlap the "zero time peak" in the coincidence mass spectrum. This problem is worse at low signal rates, and consequently the threshold is strongly affected.

The electron affinity for C_2F_5 is an anomaly. Previous measurements are near 2.0 eV (HARL 72, SUL 76) in good agreement with a theoretical value of 1.8 eV (KIN 97), but yet the mass spectra obtained at low and high energy (Figure 4.1) show that $C_2F_5^-$ is the dominant ion at low energy. Since the EA for Cl is 3.6 eV, this suggests that EA (C_2F_5) > 3.6 eV. For C_2F_5I a lower value for EA (C_2F_5) was obtained, although this value was still much greater than generally accepted.

A possible explanation for the widely varying EA's of C_2F_5 is that the $C_2F_5^-$ ion is being made in different excited states in the various experiments. The Rb electron donor materially participates in the electron transfer process and this could manifest itself in the deactivation of the transient negative molecular ion. This deactivation is likely to be more effective in the chloride (HARL 03) giving the ground electronic state. Thus it seems

Reproduced with permission of the copyright owner. Further reproduction prohibited without permission.

possible that the chloride and iodide are producing different electronic states of the $C_2F_5^-$ ion and suggesting that the literature values for EA (C_2F_5) are for even more excited states. If this reasoning were correct, EA (C_2F_5) $\approx$ 4.8 eV.

There is another possibility which we believe is more likely. Alkali metals are known to dimerize in the gas phase, and many spectroscopic properties (HUB 79) and reactivities (WEL 80, REC 77, DIS 77) of the dimers are known. The dimers constitute about 0.1% of the alkali vapor above the liquid, but dissociate upon heating the vapor independent from the liquid. We estimate that for equilibrium in the nozzle at 1100K the fraction of dimers in the Rb vapor is 10-100 ppm. Another similar alkali beam source built in Herschbach's group also suggests a tiny amount of dimers (LAR 74). The coincidence mass spectra require a Rb^+ ion to start the clock, otherwise the mass calibration would be vastly different. But dimer could produce Rb^+ according to (4.7)

$$Rb_2 + C_2F_5X = Rb^+ + C_2F_5^- + RbX \qquad (4.7)$$

with a threshold Th=BDE(Rb_2)+IP(Rb)+BDE(C-Cl)-EA(C_2F_5)-BDE(RbX). Using values for BDE and IP in Table 4.1 and Huber & Herzberg's (HUB 79) BDE for Rb_2, RbCl and RbI (0.49, 4.34 and 3.30 eV, respectively) the threshold for reaction (4.1) is predicted to be 1.92eV (C_2F_5Cl) and 1.59 eV (C_2F_5I), assuming EA(C_2F_5) = 2.0 eV.

The "threshold" reported in Table 4.1 for $C_2F_5^-$ from C_2F_5Cl is 2.9 eV, calculated assuming reaction of the monomer via equation (4.2). The speed of the Rb atom giving this collision energy is $\approx$ 2.4 km/s, which is considerably slower than 4.6 km/s expected for the H_2 seed gas. The speed of the dimer is not known, but certainly lags the speed of the monomer since the monomer lags the speed of the H_2. Using a small-angle kinematic model for the acceleration of the monomer (Appendix III), the measured speed of the

Reproduced with permission of the copyright owner. Further reproduction prohibited without permission.

monomer allows us to estimate the dimer speed at this "threshold" as ≈ 1.4 km/s. The collision energy of the dimer at this speed is ≈ 2.0 eV in qualitative agreement with the expected threshold for reaction of the dimer. A similar calculation for the iodide suggests that the dimer energy at its "threshold" is ≈2.4 eV. Thus the dimer has enough energy to react at the respective thresholds, but the energy of the dimer is less than the energy of the monomer.

The corresponding reaction of the dimer to produce Cl^- or I^-

$$Rb_2 + C_2F_5X = Rb^+ + X^- + RbC_2F_5 \qquad (4.8)$$

is highly unlikely because RbC_2F_5 is probably weakly bound, and the threshold for forming $Rb^+ + X^- + Rb + C_2F_5$ will be about 4.7 eV, corresponding to an apparent energy of the monomer ≈ 7eV. Formation of Cl^- is thus expected to be dominated by the monomer reaction.

Reproduced with permission of the copyright owner. Further reproduction prohibited without permission.

Table 4.2 Tests for dimer participation in C_2F_5Cl

T_N(K)	T_B(K)	v_0(km/s)	Δv(km/s)	Cl^-(cps)	$C_2F_5^-$ (cps)	$Cl^-/C_2F_5^-$
1091	498	3.02	0.33	63	8	7.8
835	498	3.01	0.25	4.5	3	1.5
1091	416	3.02	0.29	3.7	0.21	18
1091	498	2.84	0.33	11	5.4	2
835	498	2.84	0.26	1.1	1.6	0.7

Two sets of auxiliary measurements are made to see if Rb dimers play a role in the measurements. The experimental conditions and results for these tests are shown in Table 4.2. Decreasing the Rb nozzle temperature from 1091K to 835K, keeping the oven temperature at a constant 498K, and adjusting the backing pressure slightly to keep v_0 constant (although Δv decreases a bit) should favor dimer by increasing the equilibrium constant K for the dimerization constant. Both the Cl^- and $C_2F_5^-$ signals decrease, but the $C_2F_5^-$ signal *increases* relative to the Cl^- signal as can be seen in the ratio. A similar result is obtained at a lower backing pressure (2.84 km/s). If atoms are responsible for both Cl^- and $C_2F_5^-$ the ratio should not change, but if dimers are responsible for $C_2F_5^-$, we expect lower nozzle temperatures to favor dimers and to decrease the signal ratio, as observed. In a second test the oven temperature is lowered to 416K keeping the nozzle temperature at 1091K. The equilibrium dimer pressure, P_D, is given by $P_D=KP_M^2$ where K is the equilibrium constant for dimerization and P_M is the monomer pressure. Decreasing the temperature drastically lowers the vapor pressure P_M, and the dimer pressure is expected

Reproduced with permission of the copyright owner. Further reproduction prohibited without permission.

to further decrease. Thus, if $C_2F_5^-$ arises from dimer, decreasing the oven temperature should *lower* the $C_2F_5^-$ signal relative to Cl^- (the ratio should increase), and this is observed. We thus believe that the most likely explanation for our anomalously low threshold for $C_2F_5^-$ is that the ion is formed from the small (ppm) concentration of Rb dimers in the beam via equation (4.7). The numerical values for the $C_2F_5^-$ threshold are in error because we used the energy distribution for the monomer. Rough estimates of dimer speeds at the threshold are consistent with known values for the electron affinity of C_2F_5 and further support the assignment of these thresholds to the dimer reaction, equation (4.7).

Electron attachment of C_2F_5I has been studied using monoenergetic electrons (LAN 02). "Zero energy" electrons produce I^-, and electrons a few volts higher produce F^- from several overlapping resonances. In the present experiments we also observe I^-, but no F^- is observed because the energy is too low to break the C-F bond. As expected, the parent negative ion is not observed in the electron attachment experiments, but is observed in the electron transfer experiments reported here. The electron affinity of C_2F_5I is 0.96 ± 0.1 eV and showing that this is a stable ion.

We believe this result is for the atomic reaction:

$$Rb + C_2F_5I = Rb^+ + C_2F_5I^- \qquad (4.9)$$

The threshold for reaction (4.9) (Table 4.1) is apparently 3.22 eV, corresponding to a Rb speed of 2.46 km/s. Using the kinematic model of Appendix III, we estimate the dimer speed to be 1.46 km/s giving a collision energy of the dimer as 2.4 eV. Possible dimer reactions are

$$Rb_2 + C_2F_5I = Rb^+ + C_2F_5I^- + Rb \qquad (4.10)$$

Reproduced with permission of the copyright owner. Further reproduction prohibited without permission.

$$Rb_2 + C_2F_5I = Rb_2^+ + C_2F_5I^- \quad (4.11)$$

The threshold for reaction (4.10) is ≈ 3.7 eV, and the energy provided is too low. Reaction (4.7) is much more exoergic than reaction (4.10) because the very stable RbCl is formed. The formation of RbCl is the driving force of reaction (4.7). Reaction (4.11) produces a dimer ion that would give a totally different mass spectrum than we observe and it can be ruled out. We conclude that dimer channels do not complicate the determination of the threshold, and that the parent negative ion, $C_2F_5I^-$, is produced from Rb atoms, reaction (4.9).

The electron affinity of C_2F_5I, 0.96 ±0.1 eV, is in reasonable agreement with other analogous halogen compounds: EA(CF_3Br) = 0.91 eV (COM 78) and 0.93 eV (this work) and EA(CF_3I) = 1.4 eV (TAN 76) and 1.6 eV (COM 78).

4.2 Hexafluorobenzene (C_6F_6)

C_6F_6 contains a benzene ring and six fluorine atoms. The formation of the parent negative ion in the gas phase has an interesting and controversial history that lasts over thirty years. The electron affinity ranges from ~ 1.8 eV (tandem mass spectrometry, LIF 73) to the most recent value of ~ 0.5 eV (rate constants for electron attachment/detachment, MIL 04). The G3(MP2) theory (CUR 99) yields an electron affinity of 0.454 eV (MIL 04). The symmetry of the molecule also changes from D_{6h} to C_{2v} after the attachment of an electron (MIL 04, SHC 83, HIR 90).

We seed C_6F_6 (2.67%) in Ar as a mixture gas. After the collision with Rb atoms, parent negative ions, $C_6F_5^-$ and electrons are observed. Figures (4.12), (4.13) and (4.14)

Reproduced with permission of the copyright owner. Further reproduction prohibited without permission.

are the coincidence TOF mass spectra of C_6F_6 at low, medium and high energy, respectively. Figure (4.15) is the corresponding energy distribution.

At low energy, $C_6F_5^-$ is the dominant ion. As energy increases electron and parent ion signals start to grow up and become greater than $C_6F_5^-$ signal. This is better seen in Figure 4.16(a). The electron peak has a very long tail, which is not obvious in the mass scale. Figure 4.17 is a magnified version of the electron peak from Figure 4.13.

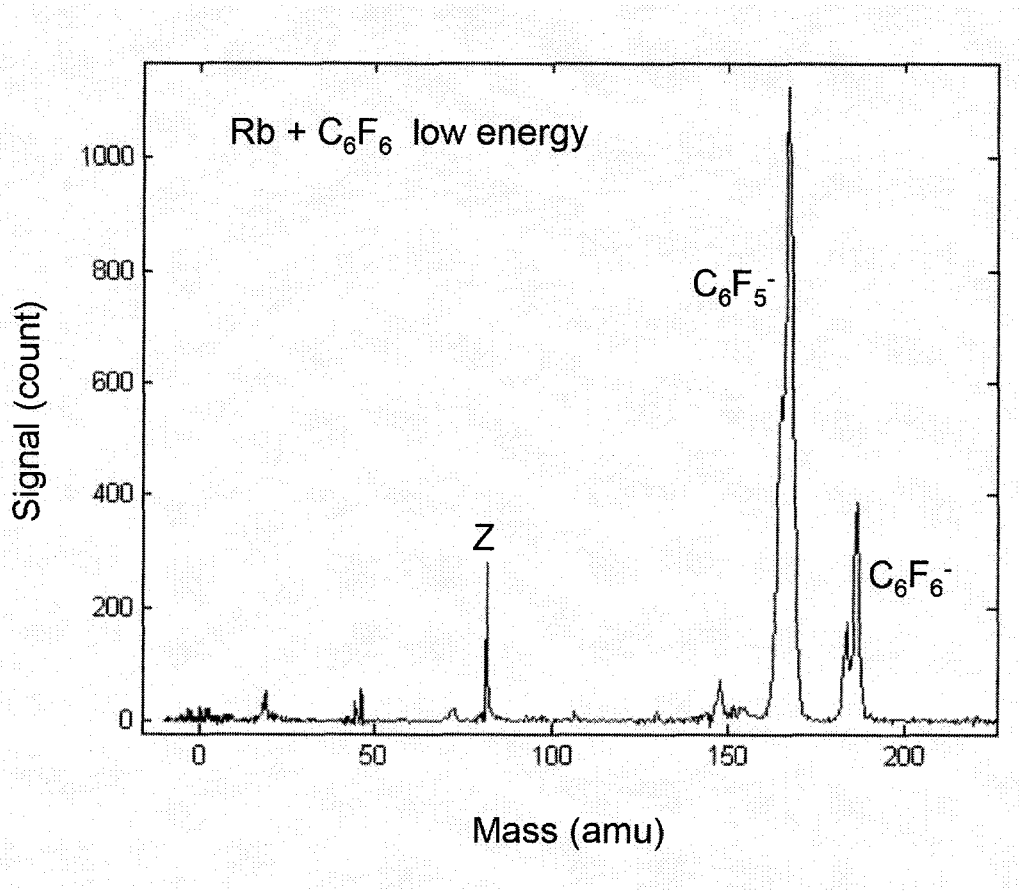

Figure 4.12 Coincidence mass spectrum of C_6F_6 at low energy (counted for 200 s), corresponding to curve 2 in Figure 4.15.

Reproduced with permission of the copyright owner. Further reproduction prohibited without permission.

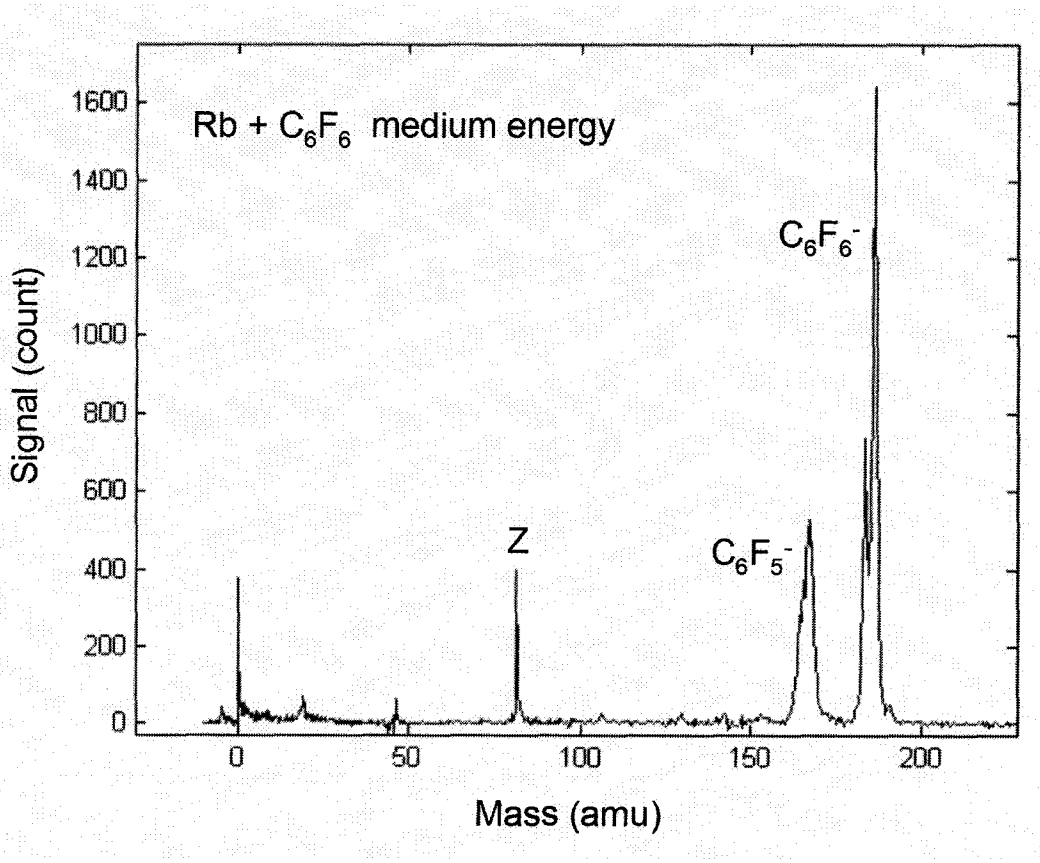

Figure 4.13 Coincidence mass spectrum of C_6F_6 at medium energy (counted for 100 s), corresponding to curve 7 in Figure 4.15.

Reproduced with permission of the copyright owner. Further reproduction prohibited without permission.

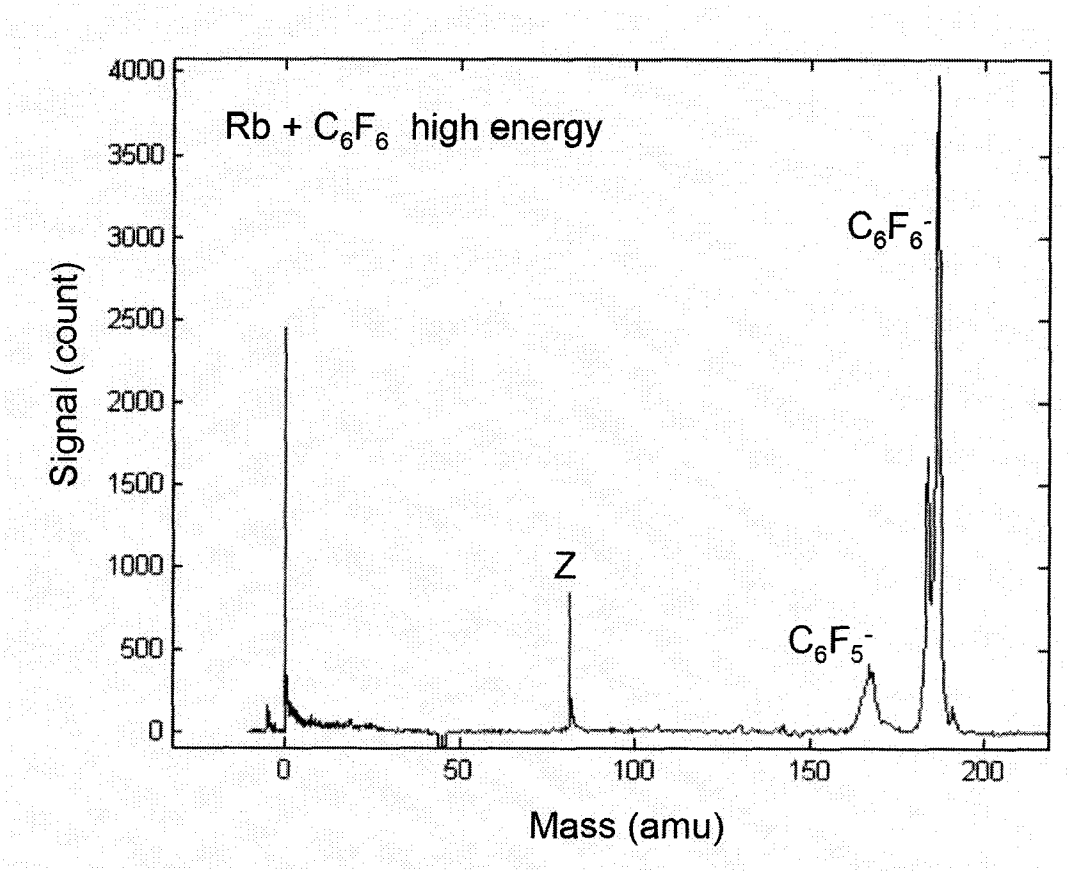

Figure 4.14 Coincidence mass spectrum of C_6F_6 at high energy (counted for 100 s), corresponding to curve 11 in Figure 4.15.

Reproduced with permission of the copyright owner. Further reproduction prohibited without permission.

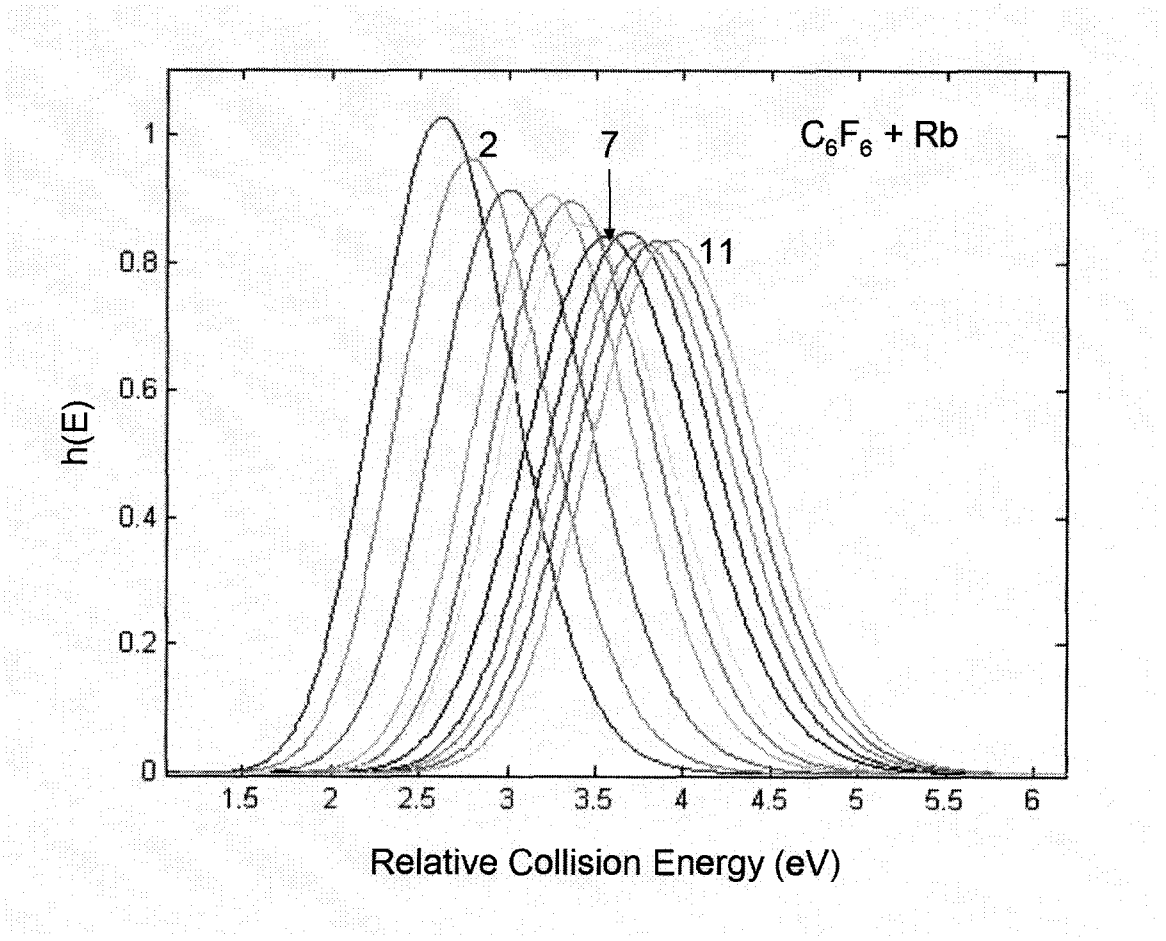

Figure 4.15 Relative energy distributions for the collisions between Rb and C_6F_6. These 11 curves are numbered in a sequential order from the lowest energy (curve 1) to the highest (curve11).

Reproduced with permission of the copyright owner. Further reproduction prohibited without permission.

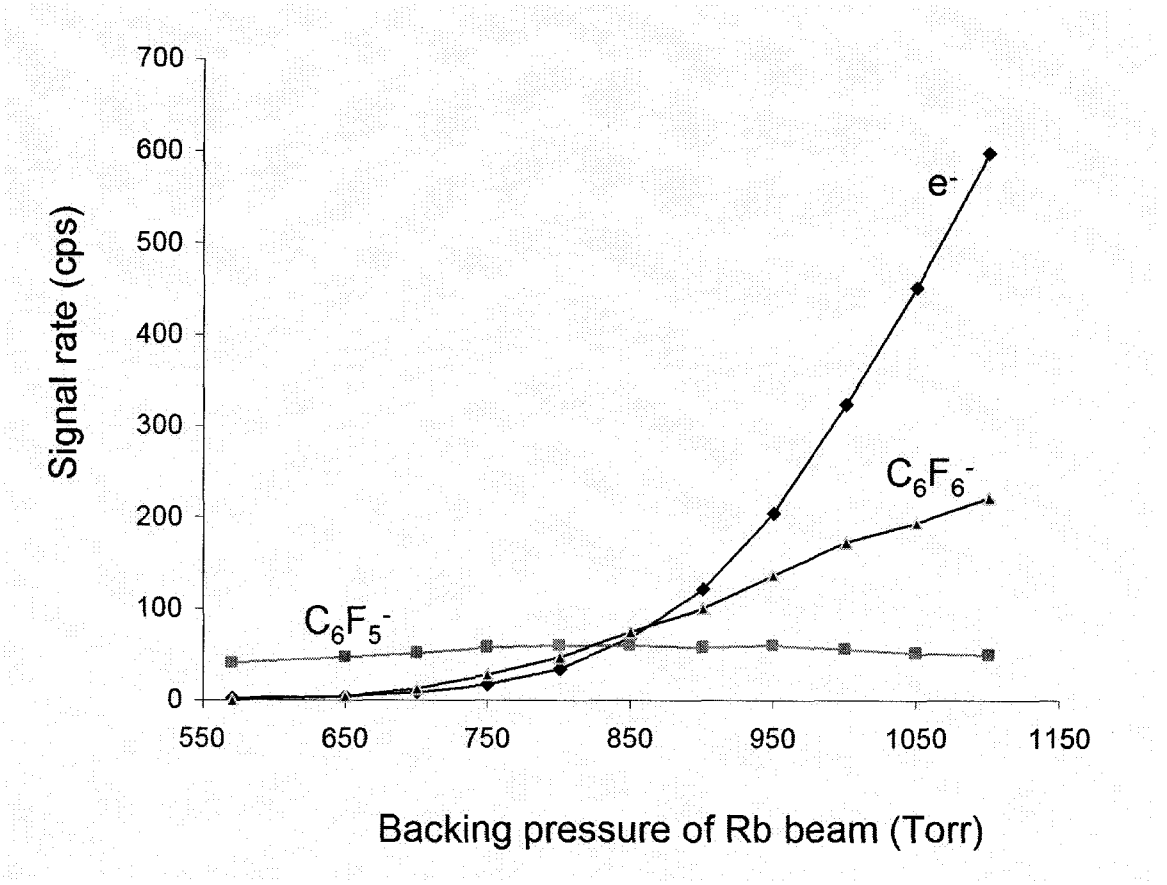

Figure 4.16(a) Different ion signals produced from the collisions between Rb and C_6F_6 as a function of the backing pressure for Rb beam. The collision energy increases as the backing pressure is increased.

Reproduced with permission of the copyright owner. Further reproduction prohibited without permission.

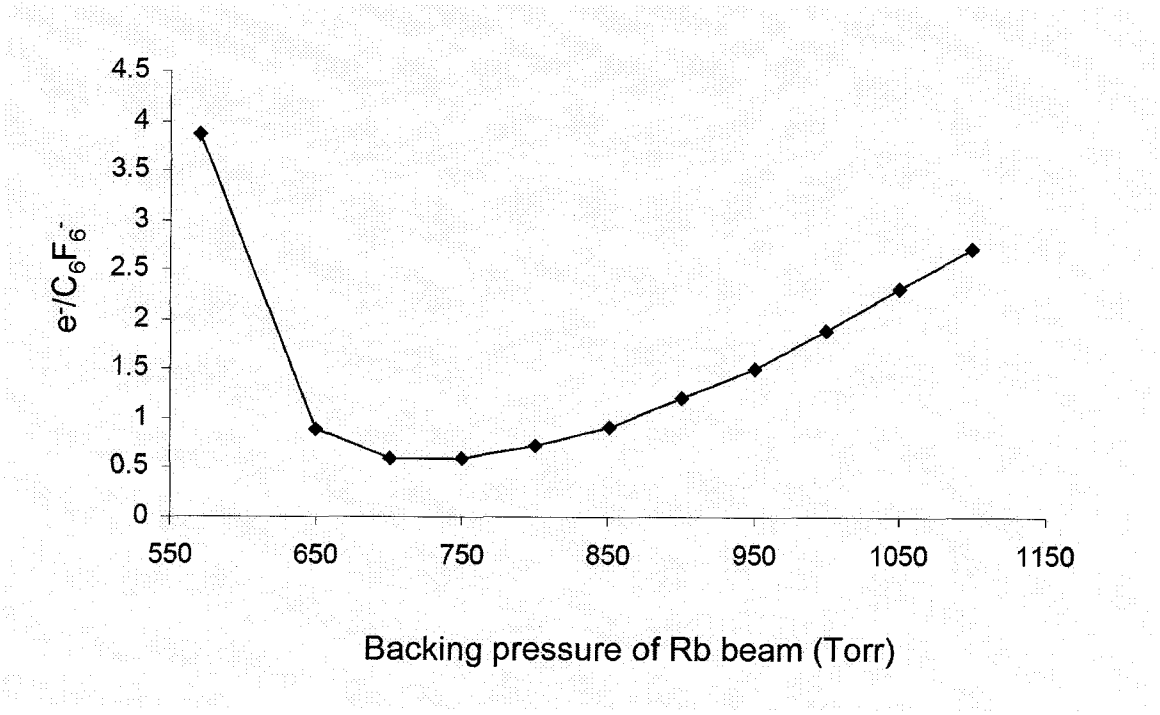

Figure 4.16(b). Ratios of electron to $C_6F_6^-$ signal as a function of Rb beam backing pressure.

Reproduced with permission of the copyright owner. Further reproduction prohibited without permission.

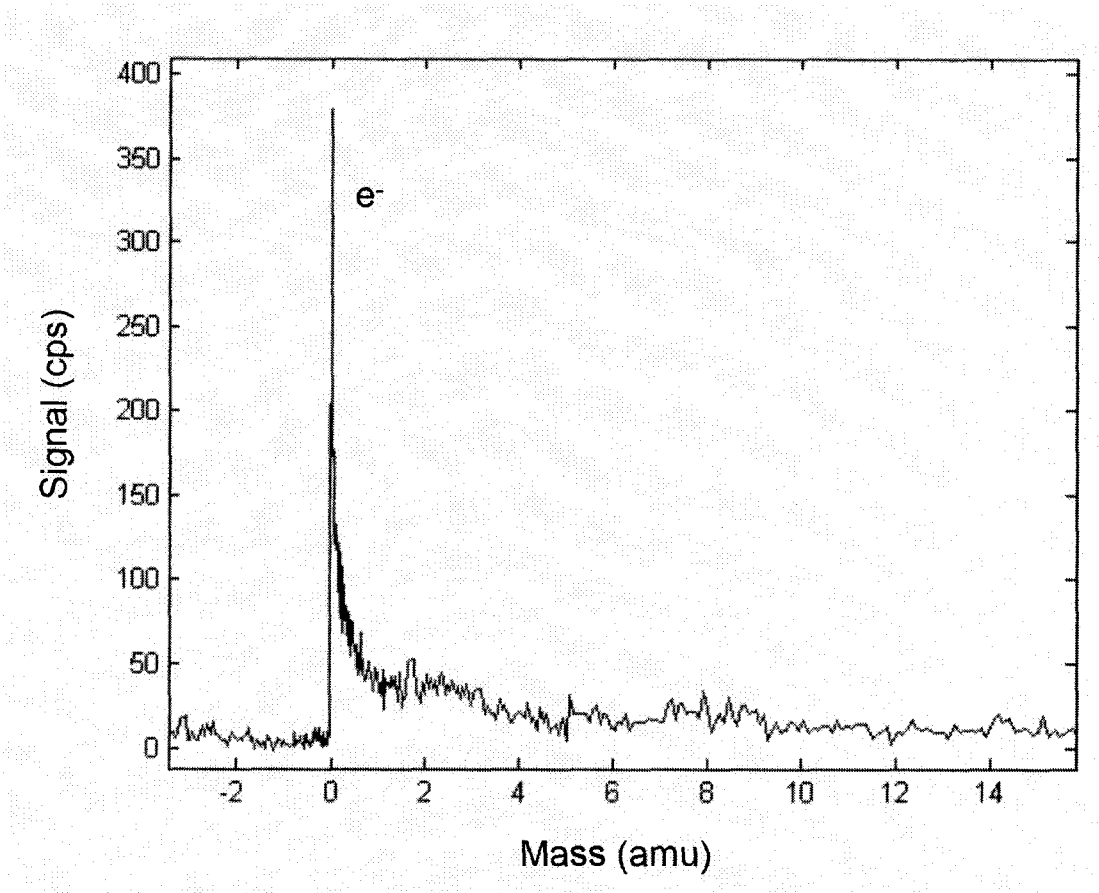

Figure 4.17 Electron peak with a long tail from Figure 4.13.

Reproduced with permission of the copyright owner. Further reproduction prohibited without permission.

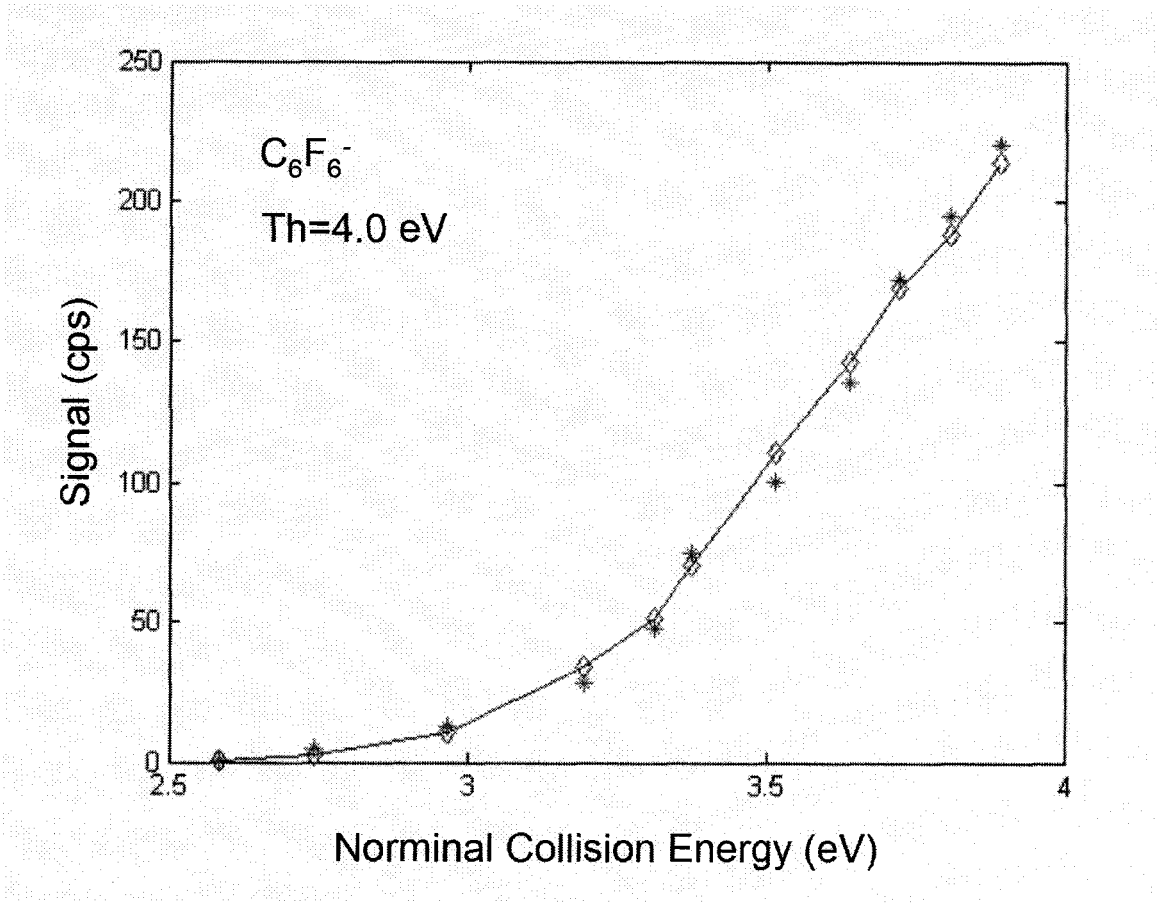

Figure 4.18 Experimental signal of $C_6F_6^-$ and the best fit.

Using the method from Chapter 3 we fit the signal of $C_6F_6^-$ and find the reaction threshold to be 4.0 ± 0.04 eV. The corresponding electron affinity of C_6F_6 is 0.18 eV.

The reaction we are interested is $Rb + C_6F_6 \rightarrow Rb^+ + C_6F_6^-$ (4.12). However all of the $C_6F_6^-$ ions formed in (4.12) are certainly not stable because some can autodetach an electron, $C_6F_6^- \rightarrow C_6F_6 + e^-$ (4.13). As energy increases the $C_6F_6^-$ signal increases as well, but the fraction of autodetaching $C_6F_6^-$ becomes greater because the ratio of electron signal to $C_6F_6^-$ goes up as seen in Figure 4.16(b). (The first few points do not show this trend because the signals at these points are very low and the cutoff of the long electron

Reproduced with permission of the copyright owner. Further reproduction prohibited without permission.

tail is from high energy data.) At high energy it is harder for C_6F_6 molecules to capture electrons from Rb atoms, and the interaction time between the temporary $C_6F_6^-$ ions and the Rb^+ ions is shorter. Both factors make the formation of a stable negative ion difficult. In addition, more energy will populate higher states of $C_6F_6^-$. The long tail of the electron peak indicates that the temporary $C_6F_6^-$ ions autodetach electrons on their flight path to the detector. The detected $C_6F_6^-$ ions are probably not in their ground state, but these ions have a lifetime at least on the order of a few μs enabling us to detect them. The signals with a threshold of 4.0 eV are not from $C_6F_6^-$ which is autodetaching. The Rb^+ ions do not remove all the excess energy from the temporary negative ions and so leave them in some lower (compared to the vertical transition) excited states. The measured electron affinity in this case is called a reactive electron affinity (GIS 79) caused by an incomplete relaxation of the temporary negative ion and thus smaller than the most recent literature value (MIL 04).

In analogy to the situation of C_2F_5Cl, we believe the $C_6F_5^-$ ion comes from the dimer reaction $Rb_2 + C_6F_6 \rightarrow Rb^+ + C_6F_5^- + RbF$ (4.14). The formation of RbF is the driving force of this reaction. One might also see $C_6F_5^-$ as a fragment of some large impurity which would have a larger kinetic energy.

4.3 Chlorine Substituted Ethene Series

Four kinds of chloroethene molecules are used as samples to test double bond systems:

Reproduced with permission of the copyright owner. Further reproduction prohibited without permission.

1) 1% C_2Cl_4 and 99% He

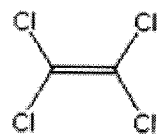

2) 2.5% C_2HCl_3 and 97.5% He

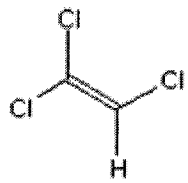

3) 10% $CH_2=CCl_2$ and 90% He

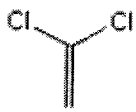

4) 10% trans-$C_2H_2Cl_2$ and 90% He

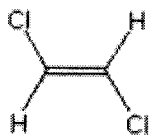

The coincidence mass spectra are shown in Figure 4.19 to 4.22.

Reproduced with permission of the copyright owner. Further reproduction prohibited without permission.

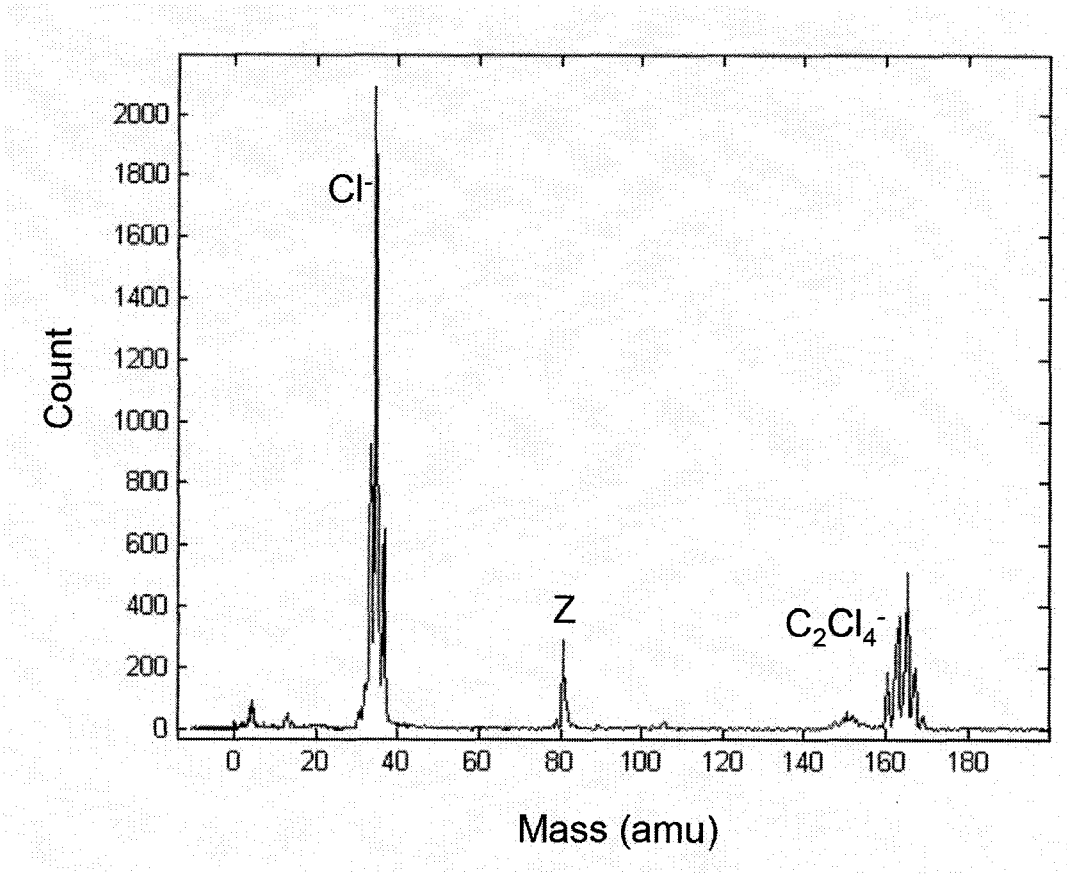

Figure 4.19 Coincidence mass spectrum of C_2Cl_4. The multiple peak of $C_2Cl_4^-$ is due to the Cl and Rb isotopes.

Reproduced with permission of the copyright owner. Further reproduction prohibited without permission.

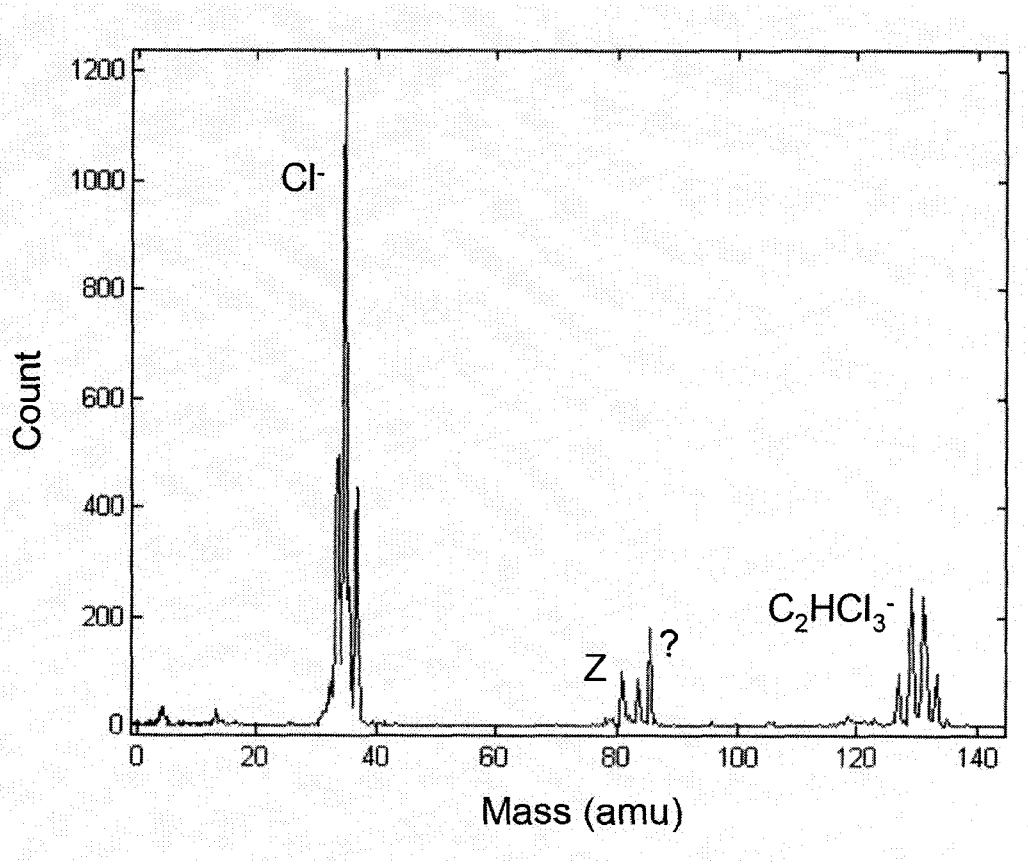

Figure 4.20 Coincidence mass spectrum of C_2HCl_3. The unknown small peak next to the zero time peak has mass around 85.

Reproduced with permission of the copyright owner. Further reproduction prohibited without permission.

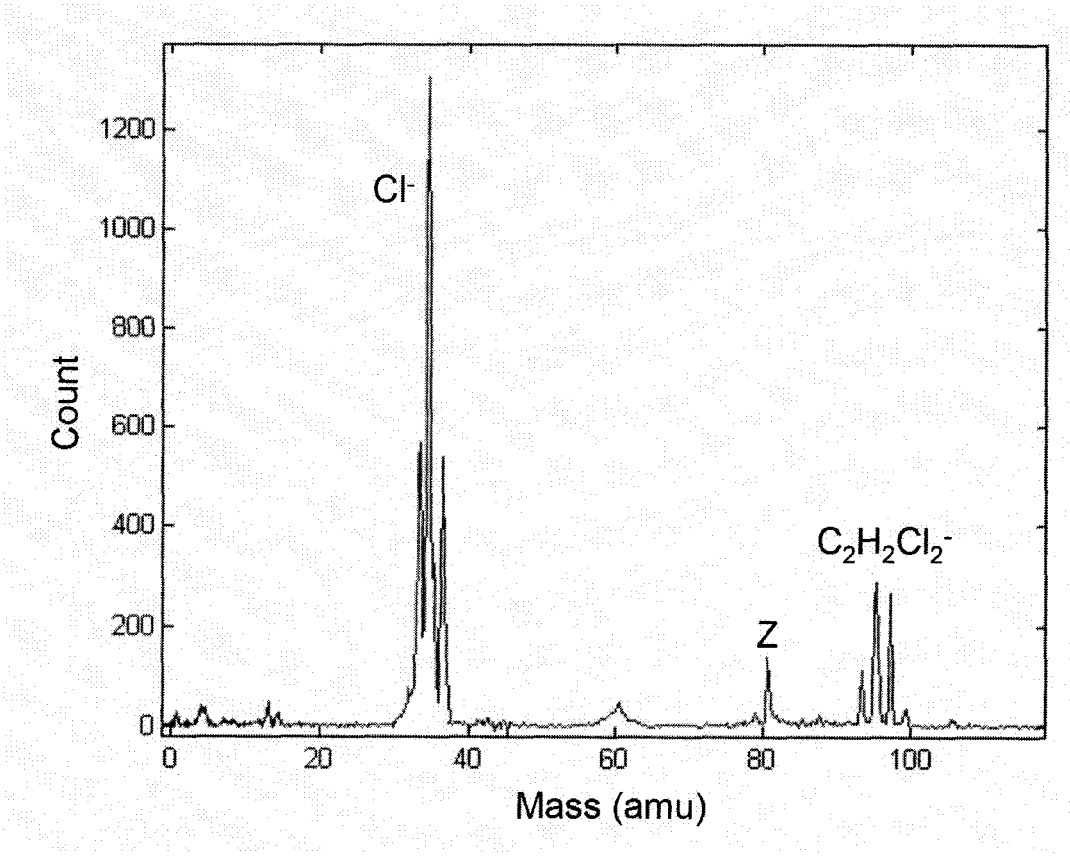

Figure 4.21 Coincidence mass spectrum of CH_2=CCl_2. The small peak at mass 60 is probably CH_2=CCl^-.

Reproduced with permission of the copyright owner. Further reproduction prohibited without permission.

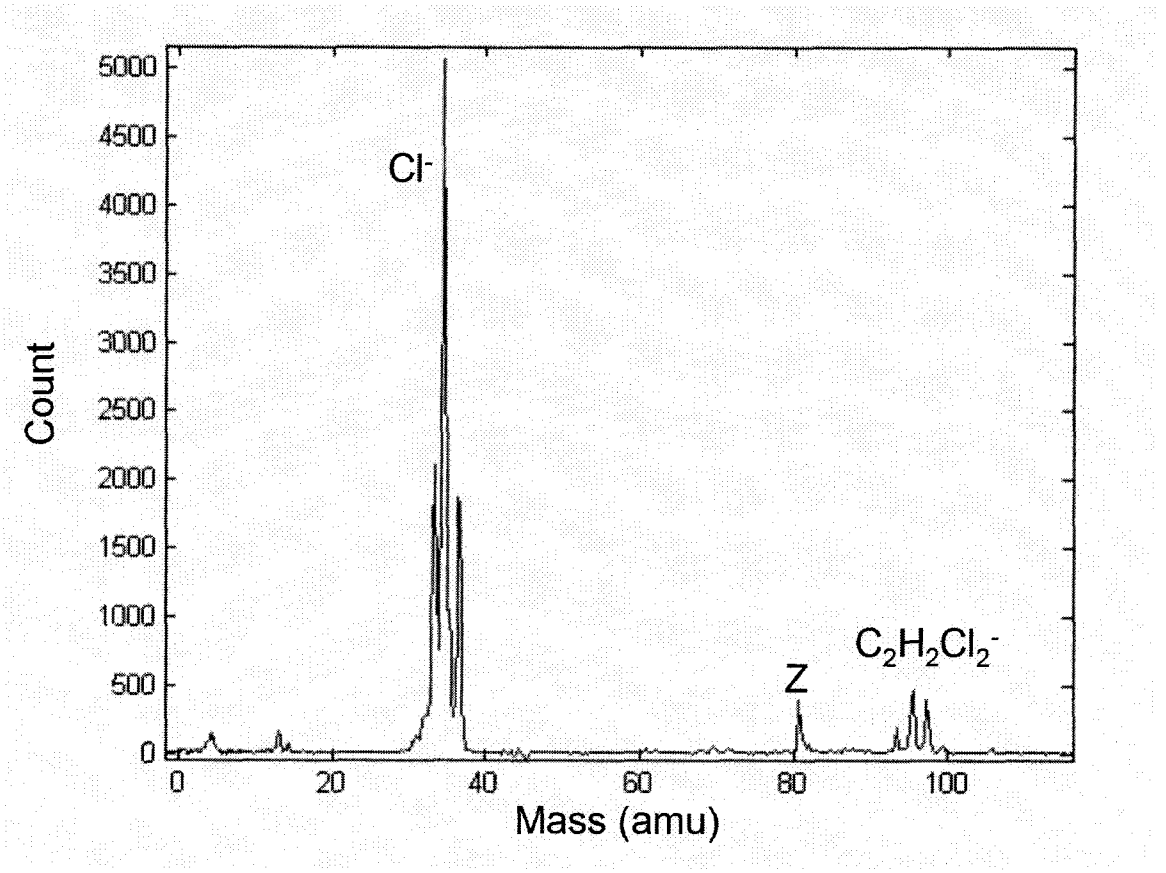

Figure 4.22 Coincidence mass spectrum of trans-$C_2H_2Cl_2$.

Parent negative ions are observed for all four molecules and Cl^- is the major product. In C_2HCl_3 the BDE of the C-H bond is ≈ 4.7 eV (LOU 03). According to the lowest energy distribution curve (Figure 4.23) the reaction threshold should be at most ~ 5 eV (end of the tail). If the negative ion signal around mass 132 is $C_2Cl_3^-$ instead of the parent ion, then the electron affinity of $C_2Cl_3^-$ will be ~ 3.9 eV, which is almost impossible. Although the mass spectrometers are not able to distinguish $C_2HCl_3^-$ and $C_2Cl_3^-$, we conclude that the signal is from the parent ions. This conclusion applies to CH_2=CCl_2 and trans-$C_2H_2Cl_2$ as well.

Reproduced with permission of the copyright owner. Further reproduction prohibited without permission.

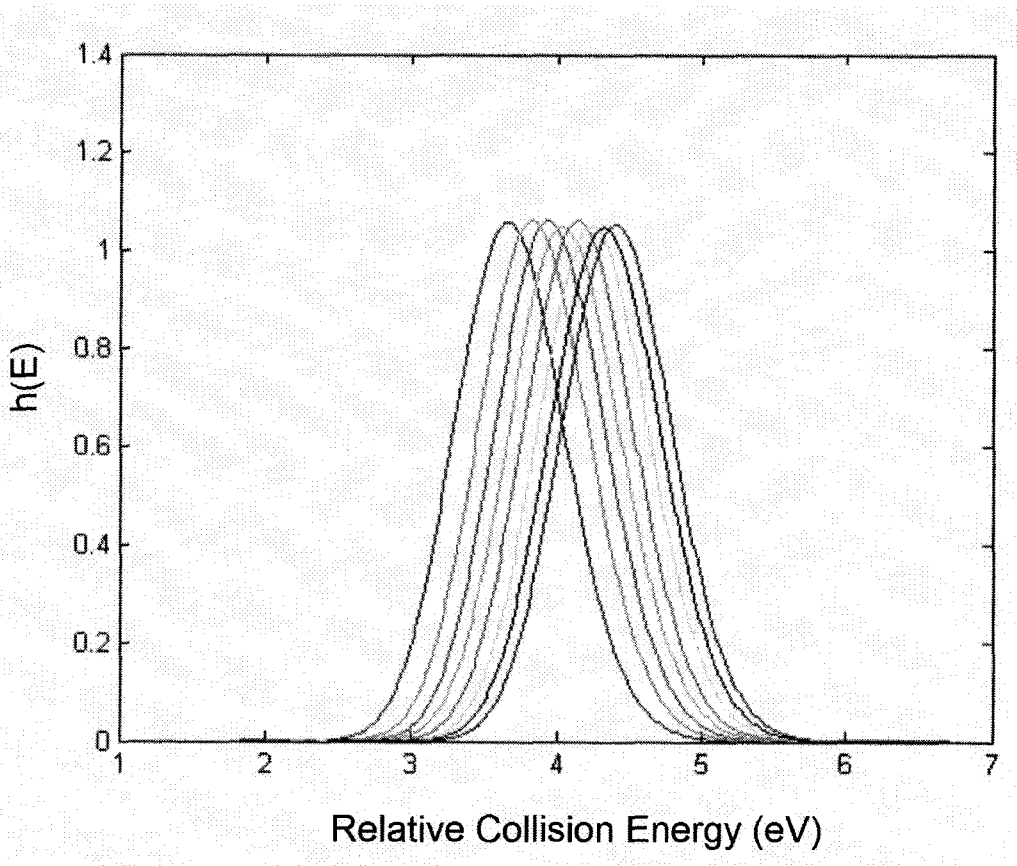

Figure 4.23 Relative energy distributions for the collisions between Rb and C_2HCl_3.

Following the data analysis in Chapter 3 the results are summarized in Table 4.3. Since the EA of Cl is well known (3.62 eV), from the Cl^- signal we calculate the C-Cl BDE instead.

Reproduced with permission of the copyright owner. Further reproduction prohibited without permission.

Table 4.3 Measured thresholds

Molecules	Ion	Threshold (eV)	EA (eV) or BDE (eV)	lit. EA (eV)[a] or lit. BDE (eV)[b]
C_2Cl_4	$C_2Cl_4^-$	4.60 ± 0.19	-0.42	0.64
	Cl^-	4.65 ± 0.14	4.09	3.98
C_2HCl_3	$C_2HCl_3^-$	4.38 ± 0.08	-0.20	0.40
	Cl^-	4.35 ± 0.07	3.79	4.06
$CH_2=CCl_2$	$CH_2=CCl_2^-$	4.45 ± 0.07	-0.27	0.1
	Cl^-	4.18 ± 0.04	3.62	4.05
t-$C_2H_2Cl_2$	t-$C_2H_2Cl_2^-$	4.52 ± 0.15	-0.34	n/a
	Cl^-	4.18 ± 0.08	3.62	3.83

a) *NIST Chemistry WebBook*

b) LOU 03

The negative values of EA's for parent ions suggest that these ions are formed in some excited states with a lifetime greater than a few μs. The BDE of C-Cl bond is close to the right value.

Because of the big mass difference between the seed molecules and He we expect the seed molecules are not moving as fast as the He atoms (it is called "slip"). Actually equation (3.8) is only an estimate of the speed of the gas molecules. If the molecules are moving slower than equation (3.8) predicts, the collision energy is actually lower than

Reproduced with permission of the copyright owner. Further reproduction prohibited without permission.

calculated, and the real threshold is less than that reported in Table 4.3. Let's try to roughly estimate the slip. C_6F_6 is actually seeded in both He and Ar although only the Ar data is shown previously. When seeded in He the threshold for forming $C_6F_6^-$ is about 5.35 eV. Assuming the slip in Ar is negligible and using the threshold for $C_6F_6^-$ in Ar (4.0 eV) as the correct value, the model of Appendix II suggests that the C_6F_6 speed (in He) is ~ 60% of an ideal isentropic expansion. Since the masses of all the chlorine substituted ethene molecules are much greater than He, we assume these molecules are also traveling at ~ 60% of the speed of an isentropic expansion (as the case of C_6F_6). With this very coarse estimation the results for the parent negative ions are in Table 4.4. These values are all positive and much closer to those in the literature (Table 4.3), showing that the slip can really be an issue in these experiments. In order to address this problem, a future work could be done to measure the speed distribution of the gas beam by another time-of-flight method with a chopper wheel and a quadrupole mass spectrometer.

Table 4.4 Thresholds for parent negative ion formation with the estimation of slip

Molecules	Th (eV)	EA (eV)
C_2Cl_4	3.65	0.53
C_2HCl_3	3.60	0.58
$CH_2=CCl_2$	3.85	0.33
t-$C_2H_2Cl_2$	3.95	0.23

Reproduced with permission of the copyright owner. Further reproduction prohibited without permission.

4.4 Other Molecules

Benzene, CO_2, biacetyl, uracil, NH_3, acetone, CF_3CFCl_2, CH_3F, C_2F_4 and $CH_2=CF_2$ are also tested in our system. The parent negative ion of biacetyl is observed but the signal is not good enough for quantitative analysis. Uracil is heated in the gas oven but the parent ion signal is still too low and not clear for identification. Other impurity peaks also appear from this sample and the intensities are greater than the uracil parent ion. Heating the sample tends to clog the nozzle. Only Cl^- is seen for CF_3CFCl_2 and F^- is not seen for any molecule listed above, suggesting the energy from two supersonic beams is not enough to break the C-F bond (which is why Rb monomer does not produce $C_6F_5^-$). No signal is observed for the rest of the molecules, which agree that these molecules are not able to form thermodynamically stable negative ions. Even if the unstable negative ions were formed through the electron transfer of Rb atoms, their lifetime is apparently too short to become detectable in the current setup.

Reproduced with permission of the copyright owner. Further reproduction prohibited without permission.

Chapter 5. Conclusions

We have developed a heated supersonic source for producing atoms that are fast enough to cause collisional ionization in electron transfer collisions. This source is used to accelerate Rb atoms and the intensity near threshold is high enough that we could directly and accurately measure the speed distribution.

The fast atoms cross a beam of molecules inside a coincidence time of flight mass spectrometer that detects both positive and negative ions and uses the time difference between the ions as a signature of the mass. Again due to the high intensity of the Rb beam we are able to detect coincidence signals near reaction thresholds. Molecules such as SF_6 and CF_3Br give well-characterized ions. Using the measured speed distributions we can deconvolve the intensity from the nominal energy to determine the energetic threshold for ion pair formation, and thereby determine electron affinities for various species.

Collisions of Rb with C_2F_5Cl produced Cl^- and $C_2F_5^-$ and suggest that the electron affinity of C_2F_5 is greater than that for Cl^-. To further investigate this, C_2F_5I is examined, yielding a somewhat different value for C_2F_5 but in addition producing the parent negative ion, $C_2F_5I^-$. We believe the anomalous C_2F_5 results probably arise from $C_2F_5^-$ formed by minute amounts of Rb_2 in the beam. We also investigate hexafluorobenzene and a series of chlorine substituted ethene molecules. All parent ions of these unsaturated systems are formed, but are apparently in some excited states since the electron affinities are negative or smaller than previously reported. However, slip in He gas beam can shift the thresholds to lower values resulting in positive electron affinities.

Reproduced with permission of the copyright owner. Further reproduction prohibited without permission.

Our results have shown that we are able to make fragment ions and some parent negative ions near threshold. Since the coincidence detection is very sensitive, the reaction products of trace concentrations of Rb dimers are sometimes detected, complicating our results, especially when fragmentation occurs. Uracil was tested but not successfully because of its very low vapor pressure. We expect to use this Rb supersonic source to collide biological molecules if we can find a way to carry them into the gas phase. We have begun to develop methods for doing this.

Reproduced with permission of the copyright owner. Further reproduction prohibited without permission.

Appendix I

```
% Matlab program used to extract three parameters τ, v0 and Δv from ATD.
% the response time τ is calculated from tail signal, only v0 and Δv are
% extracted by Marquardt method

close all
clear

name=input('type in the file name:\n','s');   % name of the ATD file
st=load(name);
ot=st(:,1);   % original time

toffset=10e-6; % offset is 10μs for TDS 430A when triggered at 4V, fall
tsensormms=10; % time for the slit to move from sensor position to horizontal in μs
tsensor=tsensormms*1e-6;

%direction=input('CW? Looking through filament window. y or n\n','s');
direction='n';
disp('default direction is now CCW');

for off=1:length(ot)
   if direction=='y'
```

Reproduced with permission of the copyright owner. Further reproduction prohibited without permission.

```
    time(off)=ot(off)+toffset+tsensor;
  else
    time(off)=ot(off)+toffset-tsensor;   %
  end
end

time=time';  % offset and sensor position is taken into account
timestep=time(2)-time(1);
signal=st(:,2);   % original signal intensity

%%%%  Revert original signal into Peaks  %%%%
L=length(signal);            % number of points collected
last=signal((L-99):L);       % the last 100 points of signal
avg100=sum(last)/100;        % average of the last 100 points
first=signal(1:100);  % the starting 100 points of signal
favg100=sum(first)/100; % average of the first 100 points

if direction=='y'
  for i=1:L
        psignal(i)=avg100-signal(i);      % revert the signal to a peak
  end
else
  for i=1:L
```

Reproduced with permission of the copyright owner. Further reproduction prohibited without permission.

```
      psignal(i)=favg100-signal(i);
   end
end

psignalc=psignal';                % to a column vector
maxpsignalc=max(psignalc);

%%%% Truncation and normalization of the original signal %%%%

tmms=time*1e6;  % time in μs
plot(tmms, psignalc)
xlabel('Time mms')
ylabel('Signal')

for k=1:50;
   judge=input('satisfied? input y or n, always no the first time \n','s');
   if judge=='n'
      initialtimeindex=input('initial time index : ');
      initialtime=(initialtimeindex-1)*timestep;
      endtimeindex=input('end time index : ');
      endtime=(endtimeindex-1)*timestep;
      finaltime=time(initialtimeindex:endtimeindex);
 % this is the time for the signal we want to analyze
```

Reproduced with permission of the copyright owner. Further reproduction prohibited without permission.

```
        finaltimemms=finaltime*1e6;    % in μs
        finalsignal=psignalc(initialtimeindex:endtimeindex)/maxpsignalc;
 % Normalization of signal by peak value, this is the signal that we want to analyze
        plot(finaltimemms, finalsignal)
        xlabel('Final Time mms')
        ylabel('Final Signal')
    else
                break
    end
end

%%%% End of Truncation and normalization of the original signal  %%%%

%%%%%% Calculation of τ  %%%%

[maxpsignalc,maxindex]=max(finalsignal);      % find the peak index and value
tailstart=maxpsignalc*0.5;            % define where the tail starts
tailend=maxpsignalc*0.1;              % define where the tail ends

for j=1:length(finalsignal)
    if j<=maxindex
        ds(j)=100;
        de(j)=100;
```

Reproduced with permission of the copyright owner. Further reproduction prohibited without permission.

```
    else
        ds(j)=abs(finalsignal(j)-tailstart);
        de(j)=abs(finalsignal(j)-tailend);
    end
end

[dsv,dsindex]=min(ds);
[dev,deindex]=min(de);
% above loop is to find the index for tail starting point and tail ending point


figure
TailSignal=finalsignal(dsindex:deindex);    % this is the tail signal
Ltail=log(TailSignal);              % log of tail signal
TailTime=time(dsindex:deindex);             % this is the tail time
w=polyfit(TailTime,Ltail,1);
Tau=-1/w(1);
Taumms=Tau*1e6                      %  τ in μs


plot(TailTime,Ltail,'bd')
hold on
Fit=w(1)*TailTime+w(2);
plot(TailTime,Fit,'r')
```

Reproduced with permission of the copyright owner. Further reproduction prohibited without permission.

```
xlabel('tail Time')
ylabel('ln(tail Signal)')
text(nscale(TailTime,0.7),nscale(Ltail,0.8),sprintf('Tau=%g mms',Taumms))
hold off

%%%%%%  End of Calculation and plot of τ  %%%%%%%%%%

 % CCW gate function without dimple is used:
disp('motor reverted November');
dimple='n';
disp('dimple excluded as default');

if direction=='y' && dimple=='y'
   load('CWGateWd');
   elseif direction=='y' && dimple=='n'
      load('CWGateWOd');
   elseif direction=='n' && dimple=='y'
      load('CCWGateWd');
   else
      load('CCWGateWOd');
end

gatetimestepmms=gatetimemms(2)-gatetimemms(1);
```

Reproduced with permission of the copyright owner. Further reproduction prohibited without permission.

```
for p=1:length(gatetimemms)
   newgatetimemms(p)=gatetimemms(p)-gatetimemms(1);
   newgatetime(p)=newgatetimemms(p)*1e-6;
 % making gate function time start from 0, in sec
end

% Now use the equations of N(μ) and S(t) to calculate the signal. Then
% adjust the parameters v0 and Δv to get a close guess of the ATD. The
% original data points and the calculated curve are drawn together in a
% plot.

figure
Flightpath=56.294;      %  in cm, see lab notebook p178.
mid=round(length(finaltime)/2);
v0=Flightpath/finaltime(mid)*1.12      % initial guess of v0, in cm/s
dv=v0/10    % initial guess of Δv, in cm/s

mu = finaltime;
lambda=newgatetime';
dlambda=0.1*1e-6;   % in sec

N=Nmu(mu,lambda,gatesignalnorm,Flightpath,v0,dv);  % function to calculate N(μ)
```

Reproduced with permission of the copyright owner. Further reproduction prohibited without permission.

```
[NormS,maxS]=Response(mu,finaltime,N,Tau);
 % function to calculate normalized S(t) and max(S(t))

plot(finaltimemms,finalsignal,'*')
hold on
plot(finaltimemms,NormS,'r')
hold off

for g=1:50
   judge2=input('satisfied? input y or n\n','s');
   if judge2=='n'
      v0=input('new guess of v0, in cm/s \n');
      dv=input('new guess of dv, in cm/s \n');
      N=Nmu(mu,lambda,gatesignalnorm,Flightpath,v0,dv);
      [NormS,maxS]=Response(mu,finaltime,N,Tau);
      plot(finaltimemms,finalsignal,'*')
      hold on
      plot(finaltimemms,NormS,'r')
      plot(finaltimemms,N/max(N),'g')
      text(nscale(finaltimemms,0.8),nscale(NormS,0.9),sprintf('v0=%g cm/s',v0))
      text(nscale(finaltimemms,0.8),nscale(NormS,0.8),sprintf('dv=%g cm/s',dv))
      hold off
   else
```

Reproduced with permission of the copyright owner. Further reproduction prohibited without permission.

```
      break
   end
end

% Use the Marquardt method to find the optimal parameters to fit the curve.
% First compute InitialChisq

for sigmaindex=1:length(finaltime)
   sigma(sigmaindex)=1;
   InitialChisqElement(sigmaindex)=(1/sigma(sigmaindex)^2)*(finalsignal(sigmaindex)-
NormS(sigmaindex))^2;
end

InitialChisq=sum(InitialChisqElement);
text(nscale(finaltimemms,0.8),nscale(NormS,0.7),sprintf('InitialChisq=%g ',InitialChisq))
% End of computing InitialChisq.

% Now compute Δa

Mlambda=0.001;
Chisq(1)=InitialChisq;   % in order to make the following loop work
v02(1)=v0;
dv2(1)=dv;
```

Reproduced with permission of the copyright owner. Further reproduction prohibited without permission.

```
MaxIt=input('input max iteration number \n');
for M=2:MaxIt

   N=Nmu(mu,lambda,gatesignalnorm,Flightpath,v0,dv);
   [NormS,maxS]=Response(mu,finaltime,N,Tau);

[Normdydv0,Normdyddv]=dydv0_dyddv(mu,lambda,Flightpath,gatesignalnorm,finaltim
e,maxS,Tau,v0,dv);

   [beta,alpha]=AlphaBeta(finaltime,finalsignal,sigma,NormS,Normdydv0,Normdyddv);

   % alphap stands for alpha' on page 162 of Bevington, 3ed.
   alphap(1,1)=alpha(1,1)*(1+Mlambda);
   alphap(2,2)=alpha(2,2)*(1+Mlambda);
   alphap(1,2)=alpha(1,2);
   alphap(2,1)=alpha(2,1);

   invalphap=inv(alphap);
   da=beta*invalphap;

   % End of computing Δa
```

Reproduced with permission of the copyright owner. Further reproduction prohibited without permission.

```
v02(M)=v0+da(1);  % all the adjusted values of v0 is recorded in v02
dv2(M)=dv+da(2);  % all the adjusted values of dv is recorded in dv2

newN=Nmu(mu,lambda,gatesignalnorm,Flightpath,v02(M),dv2(M));
[newNormS,newmaxS]=Response(mu,finaltime,newN,Tau);


for sigmaindex=1:length(finaltime)
   sigma(sigmaindex)=1;
   newChisqElement(sigmaindex)=(1/sigma(sigmaindex)^2)*(finalsignal(sigmaindex)-
newNormS(sigmaindex))^2;
end

Chisq(M)=sum(newChisqElement);

if Chisq(M)==Chisq(1)
   status='Initial Chisq is final'
   break
end

if Chisq(M) >= Chisq(M-1)
   Mlambda=10*Mlambda;
   Mlambda;
```

Reproduced with permission of the copyright owner. Further reproduction prohibited without permission.

```
    else Mlambda=Mlambda/10;
        v0=v0+da(1);  % v0 is adjusted here!
        dv=dv+da(2); % dv is adjusted here!
    end
end

[FinalChisq,FinalChisqIndex]=min(Chisq);
v0=v02(FinalChisqIndex);
dv=dv2(FinalChisqIndex);

figure
N=Nmu(mu,lambda,gatesignalnorm,Flightpath,v0,dv);
[NormS,maxS]=Response(mu,finaltime,N,Tau);

plot(finaltimemms,finalsignal,'+')
xlabel('Time (mms)')
hold on
plot(finaltimemms,NormS,'r')
title('Fitting of ATD by v0 and dv')
text(nscale(finaltimemms,0.8),nscale(NormS,1.0),sprintf('Tau=%g mms',Taumms))
text(nscale(finaltimemms,0.8),nscale(NormS,0.9),sprintf('v0=%g cm/s',v0))
text(nscale(finaltimemms,0.8),nscale(NormS,0.8),sprintf('dv=%g cm/s',dv))
```

Reproduced with permission of the copyright owner. Further reproduction prohibited without permission.

```
text(nscale(finaltimemms,0.8),nscale(NormS,0.7),sprintf('Chisq=%g',FinalChisq))
text(nscale(finaltimemms,0.8),nscale(NormS,0.6),sprintf('min Chisq,
M=%g',FinalChisqIndex))
text(nscale(finaltimemms,0.8),nscale(NormS,0.5),sprintf(name))

hold off
figure
plot(Chisq)
xlabel('iteration number M')
ylabel('Chisq')
hold on
plot(Chisq,'bd')
hold off

v0mps=v0/100
dvmps=dv/100
Taumms
```

Reproduced with permission of the copyright owner. Further reproduction prohibited without permission.

%%%%%% **Functions used in the above Program** %%%%%%%

```
function   N=Nmu(mu,lambda,gatesignalnorm,Flightpath,v0,dv)
% this function is used to calculate N(μ)

for muindex=1:length(mu)

   for lambdaindex=1:length(lambda)
   %  lambda < mu, know max(lambda)=16mms << min(mu) >200mms,
   %  so let lambdaindex go to the length of lambda

   Arg=Flightpath/((mu(muindex)-lambda(lambdaindex))*dv)-v0/dv;
   denN=(mu(muindex)-lambda(lambdaindex))^5;
N_Element(lambdaindex)=(Flightpath^4)/denN*gatesignalnorm(lambdaindex)*exp(-
Arg^2);
   end
 N(muindex)=sum(N_Element);
 % sum is over lambda, which is equivalent to the first integral
end
```

Reproduced with permission of the copyright owner. Further reproduction prohibited without permission.

```
function [NormS,maxS]=Response(mu,finaltime,N,Tau)

% this function takes the response time into account, the result should be S(t)
% both mu and t are identical to finaltime

for tindex=1:length(finaltime)

   for muindex=1:tindex
      Arg2=(finaltime(tindex)-mu(muindex))/Tau;
      integrand2(muindex)=N(muindex)*exp(-Arg2);
   end

   S(tindex)=sum(integrand2);
% sum is over mu, which is equivalent to the second integral.
end

maxS=max(S);
NormS=S/maxS;    % Normalization of S(t) by the its peak value.
```

Reproduced with permission of the copyright owner. Further reproduction prohibited without permission.

```
function
[beta,alpha]=AlphaBeta(finaltime,finalsignal,sigma,NormS,Normdydv0,Normdyddv)

% this function is to calculate the elements of alpha matrix and beta vector. Here v0
% and dv are the two parameters to be adjusted. Thus there are two elements
% in the beta vector. First one is dChisq/dv0, second is dChisq/ddv. 1=v0, 2=Δv. The
% analytical formulae of these two derivatives are calculated manually.
% This function uses the formulae to find the values.

for exptindex=1:length(finaltime)

        dChisqdv0Element(exptindex)=(1/sigma(exptindex)^2)*(-
2)*(finalsignal(exptindex)-NormS(exptindex))*Normdydv0(exptindex);
        dChisqddvElement(exptindex)=(1/sigma(exptindex)^2)*(-
2)*(finalsignal(exptindex)-NormS(exptindex))*Normdyddv(exptindex);

        alpha11Element(exptindex)=(1/sigma(exptindex)^2)*Normdydv0(exptindex)*No
        rmdydv0(exptindex);
        alpha12Element(exptindex)=(1/sigma(exptindex)^2)*Normdydv0(exptindex)*No
        rmdyddv(exptindex);
        alpha21Element(exptindex)=(1/sigma(exptindex)^2)*Normdyddv(exptindex)*No
```

Reproduced with permission of the copyright owner. Further reproduction prohibited without permission.

```
        rmdydv0(exptindex);
        alpha22Element(exptindex)=(1/sigma(exptindex)^2)*Normdyddv(exptindex)*No
        rmdyddv(exptindex);

    end


    dChisqdv0=sum(dChisqdv0Element);
    dChisqddv=sum(dChisqddvElement);

    alpha11=sum(alpha11Element);
    alpha12=sum(alpha12Element);
    alpha21=sum(alpha21Element);
    alpha22=sum(alpha22Element);

    beta=[dChisqdv0,dChisqddv]*(-1/2);
    alpha=[alpha11, alpha12; alpha21, alpha22];
```

Reproduced with permission of the copyright owner. Further reproduction prohibited without permission.

```
function
[Normdydv0,Normdyddv]=dydv0_dyddv(mu,lambda,Flightpath,gatesignalnorm,finaltim
e,maxS,Tau,v0,dv)

% this function is to calculate the normalized dy/dv0 and dy/ddv.
% y(t)=S(t)

for muindex=1:length(mu)
        for lambdaindex=1:length(lambda)
        % lambda < mu, know max(lambda)=16mms << min(mu) >200mms,
        % so let lambdaindex go to the length of lambda
           ARG=Flightpath/((mu(muindex)-lambda(lambdaindex))*dv)-v0/dv;
           den=(mu(muindex)-lambda(lambdaindex))^5;

dNdv0Element(lambdaindex)=Flightpath^4/den*gatesignalnorm(lambdaindex)*exp(-
ARG^2)*ARG*2/dv;

dNddvElement(lambdaindex)=Flightpath^4/den*gatesignalnorm(lambdaindex)*exp(-
ARG^2)*ARG*(Flightpath/(mu(muindex)-lambda(lambdaindex))-v0)*2/(dv*dv);

        end
        dNdv0(muindex)=sum(dNdv0Element);
        dNddv(muindex)=sum(dNddvElement);
```

Reproduced with permission of the copyright owner. Further reproduction prohibited without permission.

```
    end

  for tindex=1:length(finaltime) % both t and mu are finaltime

    for muindex=1:tindex
      dydv0Element(muindex)=exp(-(finaltime(tindex)-
mu(muindex))/Tau)*dNdv0(muindex);
      dyddvElement(muindex)=exp(-(finaltime(tindex)-
mu(muindex))/Tau)*dNddv(muindex);
    end

    dydv0(tindex)=sum(dydv0Element);
    dyddv(tindex)=sum(dyddvElement);
  end

  Normdydv0=dydv0/maxS;
  Normdyddv=dyddv/maxS;
```

Reproduced with permission of the copyright owner. Further reproduction prohibited without permission.

Appendix II

```
% this program calculates
%  1) Energy and realtive speed distributions of crossed beams
%  2) Best nonlinear least square fit of coincidence signal, and thus the
%  threshold of reactions.

close all
clear

collisionjudge=input('load old collision energy data?\n','s');
if collisionjudge=='y'
   load('Collision');
else

%%%%%%% Calculate the range of vr and Ecm %%%%%%%%%

mh=input('mass of heavy gas molecules\n');
ml=input('mass of carrier gas molecules\n');
x=input('fraction of heavy gas\n');
TinC=input('temperature in C\n');

[s0,ds]=Abuaf(mh,ml,x,TinC);     %  in m/s
```

Reproduced with permission of the copyright owner. Further reproduction prohibited without permission.

```
Na=6.02e23;   % Avegadra's number
JtoeV=1/(1.60e-19);   % constant converts J to eV
eVtoJ=1.60e-19;   % constant converts eV to J

Rb=85.5;   %  atomic weight of Rb
rmass=Rb*mh/(Rb+mh)*(1e-3)/Na;   %  reduced mass in kg

smin=s0-3*ds;   %  min value of s,  Mar 19, 2004
smax=s0+3*ds;   %  max value of s


name=input('type in the file name for v0 and dv, in m/s\n','s');
% files are in txt format, only contains numbers, unit m/s
% first column is v0, second is dv.

v0anddv=load(name);
RC=size(v0anddv);
Row=RC(1);  % number of experimental points

for h=1:Row
   v0(h)=v0anddv(h,1);
```

Reproduced with permission of the copyright owner. Further reproduction prohibited without permission.

```
    dv(h)=v0anddv(h,2);
    vmax(h)=v0(h)+3*dv(h);  % max value of v
    vmin(h)=v0(h)-3*dv(h);  % min value of v

    vrmax(h)=sqrt(vmax(h)^2+smax^2+smax*vmax(h));  % max value of vr
    vrmin(h)=sqrt(vmin(h)^2+smin^2+smin*vmin(h));  % min value of vr
    vr0(h)=sqrt(v0(h)^2+s0^2+s0*v0(h));

    Emax(h)=1/2*rmass*vrmax(h)^2*JtoeV; % max value of collision energy, eV
    Emin(h)=1/2*rmass*vrmin(h)^2*JtoeV;  % min value of collision energy, eV
    E0(h)=1/2*rmass*vr0(h)^2*JtoeV;  % nominal center of mass energy, eV
    newE0(h)=round(E0(h)*100)/100;  % created to be convenient to print
    newvr0(h)=round(vr0(h)*100)/100; % created to be convenient to print
end
%%%%%%%%% End of calculating the limits of vr and E



%%%%%%% Calculate f(vr) and F(E) %%%%%%%%%%%%%%%%

Nvr=300;  % integration points for vr
color(1)='b';
color(2)='g';
```

Reproduced with permission of the copyright owner. Further reproduction prohibited without permission.

```
color(3)='r';
color(4)='c';
color(5)='m';
color(6)='y';
color(7)='k';
color(8)='b';
color(9)='g';
color(10)='r';
color(11)='c';
color(12)='m';
color(13)='y';
color(14)='k';
color(15)='b';
color(16)='g';
color(17)='r';
color(18)='c';
color(19)='m';
color(20)='y';
color(21)='k';
color(22)='b';
color(23)='g';
color(24)='r';    % color controls
```

Reproduced with permission of the copyright owner. Further reproduction prohibited without permission.

```
% eqE stands for equal intervals in energy domain, just used to compare with unequal
%  intervals in energy domain.
% The resulting f(E) should look identical.


for h=1:Row


   vrstep(h)=(vrmax(h)-vrmin(h))/Nvr;  % vr increment
   eqEstep(h)=(Emax(h)-Emin(h))/Nvr;  % equal step of E


   for vrindex=1:(Nvr+1)


      vr(vrindex,h)=vrmin(h)+(vrindex-1)*vrstep(h);
      E(vrindex,h)=1/2*rmass*vr(vrindex,h)^2*JtoeV;
      eqE(vrindex,h)=Emin(h)+(vrindex-1)*eqEstep(h);  % eV
   end
%%%%%%%%%%%%%%%%
   for Eindex=1:Nvr
      Estep(Eindex,h)=E(Eindex+1,h)-E(Eindex,h);
   end
   Estep(Nvr+1,h)=Estep(Nvr,h);    % unequal E step
%%%%%%%%%%%%%%%%


   fvr=Fvr(Nvr,v0(h),dv(h),s0,ds,vr(:,h));   %  fvr is a vector of dimension Nvr
```

Reproduced with permission of the copyright owner. Further reproduction prohibited without permission.

```
NormfvrFactor(h)=vrstep(h)*sum(fvr);
% area under f(vr) curve, serves as normalization factor for f(vr)
for vrindex=1:(Nvr+1)
   BTfvr(vrindex,h)=fvr(vrindex);
   % same as fvr, not normalized, but has one more index h for future use
   Normfvr(vrindex,h)=fvr(vrindex)/NormfvrFactor(h);    % Normalized f(vr)
   FE(vrindex,h)=Normfvr(vrindex,h)/(rmass*vr(vrindex,h))*1.60e-19;  % unit eV-1
   vrforE(vrindex,h)=sqrt(2*eqE(vrindex,h)*eVtoJ/rmass);
   % m/s. speed corresponding to equally spaced E
end

for vrindex=1:Nvr+1
   NormFE(vrindex,h)=FE(vrindex,h);
   % Since Normfvr is normalized in the right way, F(E) should already
   % be normalized if F(E)dE=f(vr)dvr and dE/dvr=mu*vr are used
end

fvrforE=Fvr(Nvr,v0(h),dv(h),s0,ds,vrforE(:,h));
% f(vr) corresponding to equally spaced E

for vrindex=1:Nvr+1
```

Reproduced with permission of the copyright owner. Further reproduction prohibited without permission.

```
    FeqE(vrindex,h)=fvrforE(vrindex)/(rmass*vrforE(vrindex,h))*1.60e-19;
    % unit eV-1
  end

  % fvrforE is not normalized, so FeqE is not normalized. Now normalize it:
  NormFeqEFactor(h)=sum(FeqE(:,h))*eqEstep(h);
  for vrindex=1:Nvr+1
    NormFeqE(vrindex,h)=FeqE(vrindex,h)/NormFeqEFactor(h);
  end

  plot(E(:,h),NormFE(:,h),color(h))
  hold on

end
% end of h

for h=1:Row
  for vrindex=1:Nvr+1
    Bfvr(vrindex,h)=BTfvr(vrindex,h)/mean(NormfvrFactor);
    % in SigcalcNum, f(vr) should be Non-mormalzed because the
    % normalization factors differ from experiment to experiment. But
    % it is ok to normalize all f(vr) with the SAME number because only
    % relative values matter. Here the mean of NormfvrFactor is chosen
```

Reproduced with permission of the copyright owner. Further reproduction prohibited without permission.

```
      % to "normalize" every f(vr).
   end
end

%%%%%%%  Now plot f(E) vs. E  %%%%%%%
for h=1:Row

   H(h)=1-0.1*h;
   minE=min(min(E));  % min value of all energy points
   maxE=max(max(E));  % max value of all energy points
   Erange=[minE,maxE];  % energy range of all points

   text(nscale(Erange,0.8),nscale(NormFE(:,h),H(h)),sprintf('E0=%g eV',newE0(h)))
end

xlabel('Collision Energy (eV)')
ylabel('F(E)')
title('Energy Distribution')

hold off
```

Reproduced with permission of the copyright owner. Further reproduction prohibited without permission.

```
%%%%%%  Now plot F(vr) vs. vr  %%%%%%
figure
for h2=1:Row
   plot(vr(:,h2),Normfvr(:,h2),color(h2))
   hold on
end

for h2=1:Row

   H(h2)=1-0.1*h2;
   minvr=min(min(vr));  % min value of all energy points
   maxvr=max(max(vr));  % max value of all energy points
   vrrange=[minvr,maxvr];  % energy range of all points

   text(nscale(vrrange,0.8),nscale(Normfvr(:,h2),H(h2)),sprintf('vr0=%g
m/s',newvr0(h2)))
end

xlabel('relative speed (m/s)')
ylabel('F(vr)')
title('Speed Distribution')

hold off
```

Reproduced with permission of the copyright owner. Further reproduction prohibited without permission.

```
% %%%%%%%  Now plot F(eqE) vs. E  %%%%%%%
figure
for h3=1:Row
   plot(eqE(:,h3),NormFeqE(:,h3),color(h3))
   hold on
end

for h3=1:Row
   H(h3)=1-0.1*h3;
   mineqE=min(min(eqE));  % min value of all energy points
   maxeqE=max(max(eqE));  % max value of all energy points
   eqErange=[mineqE,maxeqE];  % energy range of all points

   text(nscale(eqErange,0.8),nscale(NormFeqE(:,h3),H(h3)),sprintf('E0=%g
eV',newE0(h3)))
end

xlabel('Collision Energy (eV)')
ylabel('F(eqE)')
title('eq space Energy Distribution')
hold off

%%%%%%%% End of calculating and plotting f(vr) and F(E)  %%%%%%
```

Reproduced with permission of the copyright owner. Further reproduction prohibited without permission.

```
relative=input('Save collision energy data?\n','s');
if relative=='y'
   save Collision
end

end
% collisionjudge

%%%%% Calculate signal and compare with experimental results  %%%%%%%

ionname=input('type in the file name for Ion intensity\n','s');
% files are in txt format, only contains a vector, all numbers
ExptSignal=load(ionname);
STDname=input('type in the file name for standard deviation\n','s');
STD=load(STDname);
ATDfile=input('type in the name of ATD area: ','s');
SATD=load(ATDfile);      %  ATDfile in txt, only contains a volume vector
Nv=300;   % choose 300 points to calculate the denominator of signal

for guessnumber=1:100
   it=input('satisfied? input y or n, always n the first time\n','s');
      if it=='n'
```

Reproduced with permission of the copyright owner. Further reproduction prohibited without permission.

```
    Th=input('input the guess of threshold, in eV\n');
  else
    break
  end

model=input('choose models, linear is 1, Gray 2, step function 3\n');
% select excitation function models

for h=1:Row
  for vrindex=1:Nvr+1
    if E(vrindex,h) < Th
      cross(vrindex)=0;
      %  cross section below threshold, independent of experiment index h
    elseif model==1
        cross(vrindex)=E(vrindex,h)-Th;
    % cross section above threshold
    % linear model of excitation function, will be normalized
    % later, thus the slope is irrelavent
    elseif model==2
        cross(vrindex)=(E(vrindex,h)-Th)^(3/2);  % Gray model
    else
      cross(vrindex)=1;
      %  step function model,will be normalized
```

Reproduced with permission of the copyright owner. Further reproduction prohibited without permission.

```
        % later, thus the magnitude is irrelevant
    end
    SigcalcElementNum(vrindex)=vr(vrindex,h)*cross(vrindex)*Bfvr(vrindex,h);
end

SigcalcNum(h)=sum(SigcalcElementNum)*vrstep(h);  % signal numerator integral

vstep(h)=(vmax(h)-vmin(h))/Nv;
for vindex=1:(Nv+1)
    v(vindex,h)=vmin(h)+(vindex-1)*vstep(h);
    SigcalcDenElement(vindex)=v(vindex,h)^3*exp(-((v(vindex,h)-v0(h))/dv(h))^2);
end

SigcalcDen(h)=sum(SigcalcDenElement)*vstep(h);
% signal denominator integral, March 2004

Ratio(h)=SATD(h)/SigcalcDen(h);

end
% end of h

NormRatioFactor=max(Ratio);  % use the max value of ratio to normalize each ratio
NormRatio=Ratio/NormRatioFactor;
```

Reproduced with permission of the copyright owner. Further reproduction prohibited without permission.

```
for h=1:Row
   Sigcalc(h)=NormRatio(h)*SigcalcNum(h);
end

for h=1:Row
   NormSig(h)=Sigcalc(h)*NormSigFactor;
end

for exptindex=1:Row
   ChisqInitialElement(exptindex)=1/STD(exptindex)^2*(ExptSignal(exptindex)-
NormSig(exptindex))^2;
end
   ChisqInitial=sum(ChisqInitialElement)  % initial Chisq

figure
plot(E0,ExptSignal,'r*')
hold on
plot(E0,NormSig,'bd-')
text(nscale(E0,0.2),nscale(NormSig,0.8),sprintf('Initial Th=%g eV',Th))
text(nscale(E0,0.2),nscale(NormSig,0.7),sprintf('Initial Chisq=%g',ChisqInitial))
text(nscale(E0,0.2),nscale(NormSig,0.6),sprintf('Initial
NormSigfactor=%g',NormSigFactor))
```

Reproduced with permission of the copyright owner. Further reproduction prohibited without permission.

```
   xlabel('Nominal Energy (eV)')
   ylabel('Signal')

   hold off

end
% end of guessnumber
% above plots both experimental and calculated signals versus norminal energy

%%%%%%% End of comparison and initial guess %%%%%%

%%%%%%%%%% Try to minimize Chisq by simple scan %%%%%%%%%%
for Normi=1:Row
   NN(Normi)=ExptSignal(Normi)/Sigcalc(Normi);
end
NormFMax=max(NN)+(max(NN)-min(NN))*1;
NormFMin=min(NN)-(max(NN)-min(NN));

if NormFMin<0
   NormFMin=0;  % want NormFMin to be positive
end
```

Reproduced with permission of the copyright owner. Further reproduction prohibited without permission.

```
deltaTh=input('input max adjustment of Th\n');
dTh=[-deltaTh:0.05:deltaTh];  % 0.05 eV is the step
L=length(dTh);

time1=clock;

NormFN=100;  % number of steps for NormF
NormFStep=(NormFMax-NormFMin)/NormFN;
for NormIn=1:NormFN+1
   NormF(NormIn)=NormFMin+(NormIn-1)*NormFStep;

   for Thindex=1:L
      newTh(Thindex)=Th+dTh(Thindex);

[Chisq(NormIn,Thindex),NormSig]=CrossBeamChisquareMarch(Row,Nvr,model,ExptSi
gnal,newTh(Thindex),vr,vrstep,E,Bfvr,v0,dv,vmax,vmin,Nv,SATD,STD,NormF(NormIn
));
   end

end
time2=clock;
timeloop=time2-time1;
time_minute=timeloop(4)*60+timeloop(5)
```

Reproduced with permission of the copyright owner. Further reproduction prohibited without permission.

```
[finalChisq,finalChisqindex]=min(min(Chisq));
finalTh=newTh(finalChisqindex);

ChisqT=Chisq';
[finalChisqT,finalNindex]=min(min(ChisqT));
finalN=NormF(finalNindex);

[FinalChisq,finalNormSig]=CrossBeamChisquareMarch(Row,Nvr,model,ExptSignal,fina
lTh,vr,vrstep,E,Bfvr,v0,dv,vmax,vmin,Nv,SATD,STD,finalN);

check1=finalChisq-finalChisqT;
check2=finalChisq-FinalChisq;

if check1~=0 || check2~=0
   display('please check check1 and check2 !')
end

% find the corresponding signal
   figure
   plot(E0,ExptSignal,'r*')
   hold on
   plot(E0,finalNormSig,'bd-')
```

Reproduced with permission of the copyright owner. Further reproduction prohibited without permission.

```
text(nscale(E0,0.2),nscale(finalNormSig,0.7),sprintf('Chisq=%g',finalChisq))
text(nscale(E0,0.2),nscale(finalNormSig,0.8),sprintf('Th=%g eV',finalTh))
text(nscale(E0,0.2),nscale(finalNormSig,0.6),sprintf('finalN=%g ',finalN))

xlabel('Nominal Energy (eV)')
ylabel('Signal')
hold off
% above plots both experimental and calculated versus norminal energy

%%%%%%%%%%%%  End of minimizing Chisq %%%%%%%%%%%%
```

Reproduced with permission of the copyright owner. Further reproduction prohibited without permission.

%%% Functions used in the above Program %%%%%%

```
function [s0,ds]=Abuaf(mh,ml,x,TinC)

% this function calculates s0 and ds from the gas mixture
% equations used are from Abuaf's paper on
% Science, vol 155, Issue 3765 (Feb. 24, 1967), 997-999

R=8.314; % in J*K-1*mol-1
m_avg=mh*x+ml*(1-x);
Cvh=(3+3)/2*R;   %  3 translational, 3 rotational for nonlinear molecular
Cvl=3/2*R;   %  momatomic molecules, like He

Cv_avg=Cvh*x+Cvl*(1-x);
Cp_avg=Cv_avg+R;
T0=TinC+273; % in K

s0=sqrt(2*Cp_avg*T0/(m_avg*1e-3));      %  in m/s
ds=0.1*s0;      %  in m/s
```

Reproduced with permission of the copyright owner. Further reproduction prohibited without permission.

```
function  fvr=Fvr(Nvr,v0,dv,s0,ds,vr)

% this function calculates the relative speed distribution function f(vr)
% It is NOT normalized

Nb=300; % number of points for beta to integrate
a=2/3*pi; % angle alpha
bstep=(pi/3)/Nb;  % angle beta step
gamma=(v0/dv)^2+(s0/ds)^2;

for vrindex=1:(Nvr+1)

   for bindex=1:Nb

        omegasq(bindex)=((sin(a+bindex*bstep)/dv)^2+(sin(bindex*bstep)/ds)^2)*(1/sin(
        a))^2;
        phi(bindex)=2*(sin(a+bindex*bstep)*v0/(dv*dv)+sin(bindex*bstep)*s0/(ds*ds))*
        (1/sin(a));
        arg(vrindex,bindex)=omegasq(bindex)*vr(vrindex)^2-
phi(bindex)*vr(vrindex)+gamma;
```

Reproduced with permission of the copyright owner. Further reproduction prohibited without permission.

```
      bintegrand(vrindex,bindex)=(sin(a+bindex*bstep)*sin(bindex*bstep))^2*exp(-
arg(vrindex,bindex));


   end


   bintegral(vrindex)=sum(bintegrand(vrindex,:))*bstep;
   fvr(vrindex)=bintegral(vrindex)*(vr(vrindex)/sin(a))^5;
end
```

Reproduced with permission of the copyright owner. Further reproduction prohibited without permission.

```
function
[Chisq,NormSig]=CrossBeamChisquareMarch(Row,Nvr,model,ExptSignal,Th,vr,vrstep,
E,Normfvr,v0,dv,vmax,vmin,Nv,SATD,STD,NormFactor)

% calculates Chi square and normalized signal for cross beam based on
% different excitation function models

  for h=1:Row
    for vrindex=1:Nvr+1
      if E(vrindex,h) < Th
        cross(vrindex)=0;
        % cross section below threshold, independent of experiment index h
      elseif model==1
          cross(vrindex)=E(vrindex,h)-Th;
      % cross section above threshold
      % linear model of excitation function, will be normalized
      % later, thus the slope is irrelevant
      elseif model==2
          cross(vrindex)=(E(vrindex,h)-Th)^(3/2);   % Gray model
      else
        cross(vrindex)=1;
        % step function model,will be normalized
```

Reproduced with permission of the copyright owner. Further reproduction prohibited without permission.

```
        % later, thus the magnitude is irrelavent
      end
    SigcalcElementNum(vrindex)=vr(vrindex,h)*cross(vrindex)*Normfvr(vrindex,h);
    end

    SigcalcNum(h)=sum(SigcalcElementNum)*vrstep(h); % signal numerator integral

    vstep(h)=(vmax(h)-vmin(h))/Nv;
    for vindex=1:Nv+1
      v(vindex,h)=vmin(h)+(vindex-1)*vstep(h);
      SigcalcDenElement(vindex)=v(vindex,h)^3*exp(-((v(vindex,h)-v0(h))/dv(h))^2);
    end
    SigcalcDen(h)=sum(SigcalcDenElement)*vstep(h); % signal denominator integral
    Ratio(h)=SATD(h)/SigcalcDen(h);

  end
  % end of h

NormRatioFactor=max(Ratio);
NormRatio=Ratio/NormRatioFactor;

for h=1:Row
  Sigcalc(h)=NormRatio(h)*SigcalcNum(h);
```

Reproduced with permission of the copyright owner. Further reproduction prohibited without permission.

```
end

for h=1:Row
   NormSig(h)=Sigcalc(h)*NormFactor;
   ChisqElement(h)=1/STD(h)^2*(NormSig(h)-ExptSignal(h))^2;
end

   Chisq=sum(ChisqElement);
```

Reproduced with permission of the copyright owner. Further reproduction prohibited without permission.

Appendix III

Estimate of slip for the dimer

The heavy particles (H) in the beam are accelerated by having the light ones (L) bump into them. To a good approximation, these are elastic collisions, meaning there is no change of the internal states of the particles.

Consider a fast, light molecule H_2 hitting a slow heavy atom Rb. The velocity vectors in the lab and in the center of mass are shown below

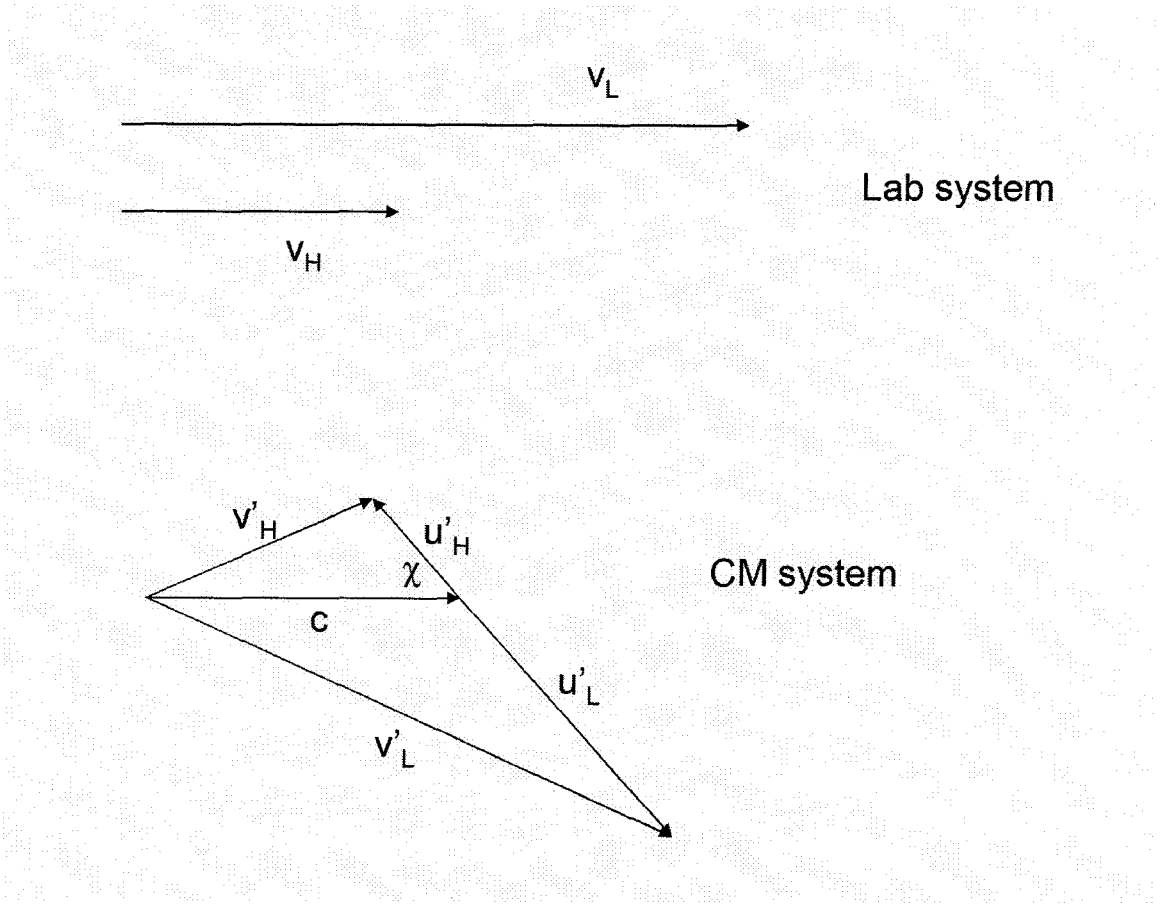

Reproduced with permission of the copyright owner. Further reproduction prohibited without permission.

In this picture, we assume v_L and v_H are directed in the x-direction, and

$$Mc = m_H v_H + m_L v_L$$
$$M = m_H + m_L$$
$$V_r = v_L - v_H = u_L - u_H$$
$$m_H u_H + m_L u_L = 0$$

where v and u refer to velocities in the lab and center of mass system, respectively. If the collision is elastic then the only consequence of a collision is that the relative vector is turned through a scattering angle χ , and it is most likely that χ is very small. It is exaggerated in the picture above.

As long as χ is very small the velocity of the heavy particle after collision is collinear with c and is given by

$$v_H' = c + u_H' \approx c + u_H' \cos\chi \approx c + u_H \cos\chi$$
$$u_H = -\frac{m_L u_L}{m_H} = -\frac{V_r}{1+\frac{m_H}{m_L}} = -\frac{m_L V_r}{M}$$
$$v_H' = \frac{m_H v_H + m_L v_L}{M} - \frac{m_L V_r}{M}\cos\chi$$
$$= \frac{m_L v_L(1-\cos\chi) + v_H(m_H + m_L\cos\chi)}{M}$$

If $\chi = 0$, then $\cos\chi = 1$ and $v_H' = v_H$ (effectively no collision). For very small values of χ, we approximate $\cos\chi = 1 - \chi^2/2$ and we have

$$v_H' = \frac{m_L v_L \frac{\chi^2}{2} + m_H v_H + m_L v_H\left(1-\frac{\chi^2}{2}\right)}{M} = v_H + \frac{m_L}{2M}(v_L - v_H)\chi^2$$

The Rb atoms and dimers are accelerated by a large number of small angle collisions. Omitting χ^4 and higher power terms, the speed of the heavy particle after n collisions of angle χ is

Reproduced with permission of the copyright owner. Further reproduction prohibited without permission.

$$v_H' = v_H + \frac{m_L}{2M}(v_L - v_H)[n\chi^2] = v_H + \frac{m_L}{2M}(v_L - v_H)\Omega \qquad (*)$$

The number of H_2 collisions with each Rb atom is the same as the number with Rb_2 and to a first approximation we can assume that χ^2 is the same for the monomer and the dimer. We have measured v_H'; v_L and v_H can be calculated from the temperature in the nozzle, so we can estimate Ω :

At 1000K,

$$v_{H_2} = \sqrt{\frac{3RT}{m_{H_2}}} = \sqrt{\frac{3\times 8.314\times 1000}{0.002}} = 3531\ (m/s)$$
$$v_{Rb} = 542\,(m/s)$$
$$v_{Rb_2} = 383\,(m/s)$$

If we measure, say 2500 m/s for the dominant monomer. Using equation (*), we calculate

$$2500 = 542 + \frac{2}{2\times(85+2)}(3531-542)\Omega$$
$$\Omega = 58$$

Using this value, we now estimate that for the dimer,

$$v_H' = v_H + \frac{m_L}{2M}(v_L - v_H)\Omega = 383 + \frac{2}{2\times(85\times 2+2)}(3531-383)\times 58$$
$$= 1444\,(m/s)$$

Reproduced with permission of the copyright owner. Further reproduction prohibited without permission.

Appendix IV

Reproduced with permission from *The Journal of American Chemical Society*, **124**, 13896 (2002). Copyright 2002 American Chemical Society

Evidence for Orbital-Specific Electron Transfer to Oriented Haloform Molecules

Beike Jia, Jonathan Laib, R. F. M. Lobo[a], & Philip R. Brooks*

Contribution from the Chemistry Department and Rice Quantum Institute, Rice University,
Houston, Texas 77251

Received July 15, 2002

Abstract

Beams of hyperthermal K atoms cross beams of the oriented haloforms CF_3H, CCl_3H, and CBr_3H, and transfer of an electron mainly produces K^+ and the X^- halide ion which are detected in coincidence. As expected, the steric asymmetry of CCl_3H and CBr_3H is very small and the halogen end is more reactive. But even though there are three potentially reactive centers on each molecule, the F^- ion yield in CF_3H is strongly dependent on orientation. At energies close to the threshold for ion-pair formation (≈5.5 eV), H-end attack is more reactive to form F^-. As the energy is increased the more productive end switches and F-end attack dominates the reactivity.

In CF_3H near threshold the electron is apparently transferred to the σ^*_{CH} antibonding orbital, and small signals are observed from electrons and CF_3^- ions

[a] Permanent address: Grupo de Nanotecnologia e Ciência à Nano-Escala, Departamento de Física, Faculdade de Ciência e Tecnologia, Universidade Nova de Lisboa, Monte Caparica, Portugal.
* to whom correspondence should be addressed.

Reproduced with permission of the copyright owner. Further reproduction prohibited without permission.

indicating "activation" of this orbital. In CCl_3H and CBr_3H the steric asymmetry is very small, and signals from free electrons and CX_3^- ions are barely detectable indicating that the σ^*_{CH} antibonding orbital is not activated. The electron is apparently transferred to the σ^*_{CX} orbital which is believed to be the LUMO. At very low energies the proximity of the incipient ions probably determines whether salt molecules or ions are formed.

Introduction

Direct experiments with oriented reagents show what had been surmised for a long time: chemical processes depend on the reagent orientation. These processes include chemical reaction[1,2], electron transfer[3,4], ionization[5], photodissociation[6-9], energy transfer[10,11], and surface scattering[10,12,13]. Relatively small molecules have been oriented by "brute force" techniques[14,15] and a number of small symmetric tops have been studied by selecting orientations using an inhomogeneous electric field[1,2].

Although the effects of orientation are real, the magnitude of the steric asymmetries observed so far has been comparatively small, especially since our mental picture of reaction is usually that of an "all-or-nothing" process. But our imagination paints a classical picture of a molecule fixed in space and fails to account for a quantal distribution of orientations that must result even from a single quantum state. Likewise, the experiments have failed to produce a highly oriented sample, either because hard-to-orient high J states are present in the brute force experiments, or because hard-to-orient prolate symmetric tops have been (mainly) used in the hexapole selection experiments.

We have chosen to study the haloform molecules, not only because of their role in atmospheric reactions[16] and their implication in global warming[17], but also for their

Reproduced with permission of the copyright owner. Further reproduction prohibited without permission.

intrinsic interest. Whereas most small molecules are near-prolate tops[18] which are difficult to spin about their symmetry axes, these molecules, CF_3H, CCl_3H, and CBr_3H, are all oblate tops and rotate like a bicycle wheel. They should produce a distribution of orientations closer to our mental picture than does a prolate top such as CH_3Br. But since they have three potentially reactive sites and since the H atom is usually considered insignificant, we expected that the steric asymmetry might still be small. This is true for CCl_3H and CBr_3H. To our great surprise, however, not only is the steric asymmetry of CF_3H larger than any molecule we have examined, but also the steric asymmetry changes sign as the collision energy is changed. At energies near the threshold for ion pair production (~ 5.5 eV) F^- is produced preferentially by attack at the H-end of the molecule. As the energy is raised the preference shifts to the CF_3 end and the asymmetry maximizes and then declines. This behavior appears to arise from a low-energy reaction channel favored by H-end attack and a higher-energy channel favored by CF_3-end attack. At low energies the electron is most likely transferred to the σ^*_{CH} orbital at the H end of the molecule but at higher energies the preference apparently shifts to the σ^*_{CX} at the F end of the molecule.

Experimental

The experimental apparatus has been previously described[19,20]. A beam of fast (4-30 eV) K atoms produced by charge exchange[21] intersects a beam of hexapole state-selected molecules between two small time-of-flight mass spectrometers identical except for polarity. The beams are continuous and the voltages on the mass spectrometers are constant so there is no time zero. Since the positive and negative ions are produced

Reproduced with permission of the copyright owner. Further reproduction prohibited without permission.

simultaneously, the *difference* in flight times provides mass analysis as long as the count rate is low enough to avoid confusing ions from different events.

Haloform beams were produced from 10% mixtures in helium except for bromoform, which was produced by passing 150 torr of helium over liquid CBr_3H at ≈ 22° C (vapor pressure ≈ 6 torr) making the beam about 4% in CBr_3H. Signal fluctuations apparently caused by variations in surface area at the liquid-gas interface were minimized with a fiberglass wick which increased the surface area and greatly stabilized the signal.

An inhomogeneous hexapole electric field selects molecules in well-defined quantum states. The beam is coaxial with the rods, and molecules are deflected in this field according to their rotational state described by the quantum numbers *J, K*, and M[22]. The interaction energy of the top with the electric field is given by

$$W = -\mu \cdot \boldsymbol{E} = -\mu EMK/(J(J+1)) = -\mu E\langle\cos\theta\rangle \qquad (1)$$

where θ is the angle between the top axis and the electric field. For molecules with $\langle\cos\theta\rangle > 0$, the energy decreases as the field increases, and molecules in these quantum states will be drawn towards the charged rods of the hexapole and are defocused. Molecules with $\langle\cos\theta\rangle < 0$ are *focused* by being forced towards the axis where the field is zero; the beam intensity increases when voltage is applied to the rods. Those with $\langle\cos\theta\rangle = 0$ are unaffected.

The beam of molecules leaves the state-selecting field, passes through an aperture and enters an ultra-high vacuum collision chamber where the molecules intersect the beam of fast K atoms. Collisions occur in a weak (~ 300 V/cm) electric field between the two time of flight mass spectrometers. (A weak electric field is present along the molecule flight to insure that the molecules remain in the same *J, K*, and *M* states.)

Reproduced with permission of the copyright owner. Further reproduction prohibited without permission.

Molecules in these selected quantum states are *oriented* with respect to the field between the mass spectrometers[23]. If the polarities of the mass spectrometers are reversed, the field direction between them is reversed, and the laboratory orientation of the molecules is also reversed. The molecules always remain in quantum states with $\langle\cos\theta\rangle < 0$, corresponding to the negative end of the molecule pointing towards the negatively charged field plate.

The polarities of the tof mass spectrometers determine whether the positive or negative end of the molecule is attacked, and data is taken for each of these polarities with the hexapole field energized and with the hexapole field off. The hexapole field does not have a beam stop so when the hexapole is not energized a weak, *totally random* beam is transmitted. The signals from symmetric top molecules increase when the high voltage is applied which helps to identify the mass peaks for calibration. The steric asymmetry is calculated from the HV_{on} - HV_{off} difference, $\Delta S_{\pm}$, ($\pm$ denotes positive- or negative-end attack) and the random beam signals are used to eliminate differences in collection efficiency or detection efficiency which arise when the detector polarities are reversed[24]. A computer turns the HV on and off for each orientation at a given collision energy in order to rapidly compare orientations. The collision energy sequence is chosen randomly and differs from day to day.

This coincidence time-of-flight mass spectrometer system collects ions from an extensive volume using the Wiley-McLaren[25] technique to space-focus the ions. But the flight time depends on the initial kinetic energy of the neutral reagents because the extraction field is nominally parallel or anti-parallel to the large relative velocity. There is thus a considerable shift between the flight times for positive-end or negative-end

Reproduced with permission of the copyright owner. Further reproduction prohibited without permission.

attack, and the spread in relative velocities limits the resolution[19] to about 2 amu at m/e =80, which is insufficient to distinguish between CF_3^- and CF_3H^-.

For CCl_3H only the $^{35}Cl^-$ signals were analyzed because simultaneous electrical interference impressed on both channels appears near mass 39. To a first approximation, this interference is identical with HV on and HV off and the difference is zero, but small fluctuations can swamp nearby real signals.

Results

Electron transfer to the various haloforms mainly produces the halide ion, although free electrons and anions with m/e near that of CX_3^- are formed in small abundance. Fig 1 shows representative relative ion signals at 10 eV for the three molecules. The relative cross section for CBr_3H is about 2.5 times larger than suggested by Fig 1 because, as previously described, helium passed over the liquid to form the CBr_3H beam. Although our mass resolution cannot distinguish between even CF_3^- and CF_3H^-, these ions (and those from CCl_3H and CBr_3H) are thought to be CX_3^- on the basis of their thresholds and electron affinities.[26,27] For CBr_3H an ion with m/e $\approx$ 172 appears which could be either CBr_2H^- or CBr_2^- resulting from loss of a Br atom or an HBr molecule. We are unable to distinguish between these ions.

Reproduced with permission of the copyright owner. Further reproduction prohibited without permission.

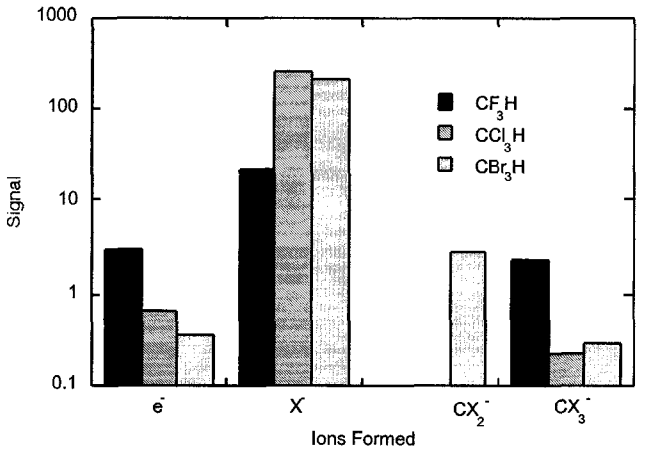

Figure 1. Comparison of ion signals among the haloforms studied at 10eV CM. The relative cross section of CBr_3H is about 2.5X larger than suggested in the figure.

Threshold Energies. Nominal threshold energies are shown in Table I. The energy scale was calibrated with SF_6.[28] These apparent thresholds are rather rough values, given our inability to account for the energy spread in the K atom beam and the spread in the data due to day-to-day fluctuations in absolute intensity. The X^- thresholds are comparable to those expected and are the same for both orientations. The electron thresholds seem uniformly high by more than about 2 eV. This suggests that the molecules may be intimately involved in a sequential process in which a transient molecular negative ion is formed for a short time before the electron is ejected, and that the molecule is left in a state excited by some two eV after the electron departs. The apparent threshold for "CBr_3" is ≈1.8 eV less than predicted [27,26], suggesting that either the *EA* for CBr_3 is much larger, or that this ion may correspond to the parent negative ion, $CHBr_3^-$ which has been predicted to be stable[29].

Reproduced with permission of the copyright owner. Further reproduction prohibited without permission.

Table I
Apparent thresholds. (Predicted[26,27,30])

Molecule	electrons	X^-	CX_2^-	CX_3^-
CF_3H	6.7 ± .4	5.8 ± .4		7.1 ± .4
	(4.34)	(5.6)		(6.9)
CCl_3H	6.7 ± .3	4.6 ± .2		6.0 ± .5
	(4.34)	(4.2)		(6.1)
CBr_3H	6.2 ± .3	4.0 ± .2	4.5 ± .3	5.2 ± 0.53
	(4.34)	(3.7)		(~7)
			(~5.3 $CHBr_2$-)	
			(~ 6 CBr_2-)	
			(~ 9.8 CBr_2- + H + Br)	

Steric Effects. The experimental signal rates for positive end and negative end attack depend strongly on energy because the K beam intensity and the cross section both increase strongly with energy[31]. In order to focus on the steric effects, this variation is removed by defining the *steric asymmetry G(E)* in terms of the cross sections for positive end attack, $\sigma_+(E)$ and negative end attack, $\sigma_-(E)$ as

$$G(E) = \left(\sigma_-(E) - \sigma_+(E)\right)/\left(\sigma_-(E) + \sigma_+(E)\right) \qquad (2)$$

This is obtained from the experimental signal differences $\Delta S_{\pm}(E)$ and ratios $R_{\pm}(E)$[24], where $S_{\pm}(E,V)$ is the experimental signal for positive or negative attack at energy E and hexapole voltage V. The steric asymmetry *G(E)* is zero if the positive end and negative end reactivities are the same and becomes ±1 if only one end is reactive, depending on the polarity of the reactive end.

Halide Ions. The steric asymmetry for formation of halide ions is shown in Fig 2. Even though there are three potentially reactive sites, *G* for CF_3H is the largest we have measured, and clearly reverses sign as the energy is changed. At low energies *positive* end attack favors the formation of F^-. The asymmetry changes sign near 6 eV whereupon negative end attack is more favorable. The asymmetry maximizes in the 7-9 eV range,

Reproduced with permission of the copyright owner. Further reproduction prohibited without permission.

and then declines. Chloroform might be similar, but the effect is far less dramatic. Bromoform reacts almost as if it were spherical, with only a slight preference for negative end attack. The asymmetry for CBr_3H is extremely small and appears to minimize near 15 eV.

Data were taken over many months and the absolute signal rates are subject to fluctuations from beam intensity variations. These fluctuations affect the threshold values, but are less severe for G values. As a consequence, a few G values are included for energies below the rough thresholds given in Table I. The G values are deemed more reliable than the thresholds.

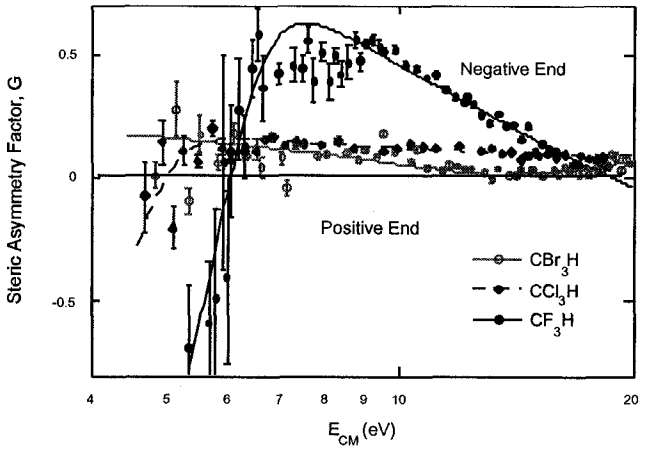

Figure 2. Steric asymmetry for formation of halide ions, X^- for the three haloforms. Error bars are ± 1σ, and curves are model fits to the data. A log scale is used to better display the low energy data.

Reproduced with permission of the copyright owner. Further reproduction prohibited without permission.

Electrons and CX_3^- ions. Other ions are formed in much lower abundance, as shown in Fig 1, and the steric asymmetry is more difficult to measure, especially at low energies. Fig 3 shows data for fluoroform. Electrons seem to be preferentially formed upon negative end attack. Although the data for CF_3^- is noisy at low energies, the trend is opposite to that for the electrons and formation of CF_3^- is favored for positive end attack.

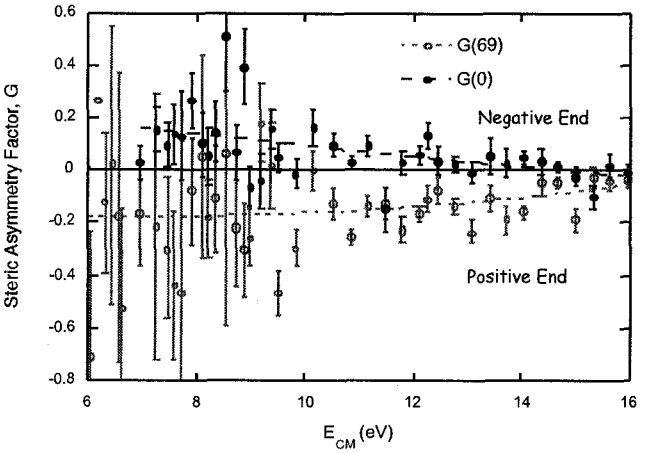

Figure 3. Steric asymmetry for electrons and CF_3^- ions formed after electron transfer to fluoroform. Least square quadratic fits are drawn to distinguish the electron asymmetry from the CF_3^- asymmetry.

Fig 4 shows the steric asymmetry for electrons and for CCl_3^- ions from chloroform. The data seems rather scattered, but very broadly speaking the steric asymmetry shows the same trend as for CF_3H. Negative end attack seems to produce more electrons and positive end attack more CCl_3^-. The analogous data for bromoform is highly scattered and is not shown.

Reproduced with permission of the copyright owner. Further reproduction prohibited without permission.

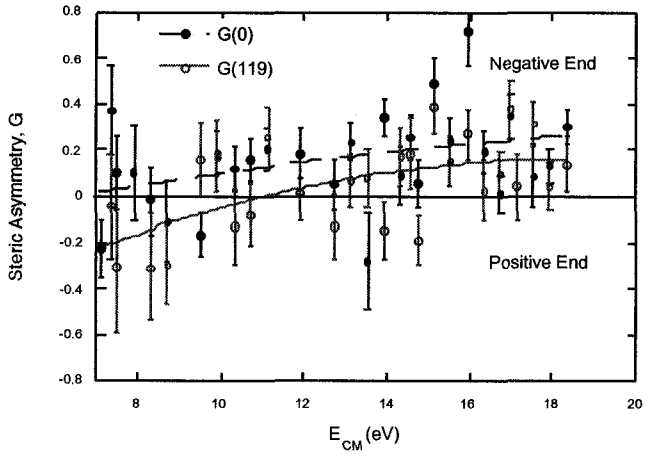

Fig 4. Steric asymmetry for electrons and CCl_3^- ions from CCl_3H. The curves are least square quadratic fits drawn to compare the behavior of the two ions.

Comparison of orientation distributions. Fig 2 shows not only an enormous steric effect for CF_3H but also a remarkable difference between the very asymmetric reactivity of CF_3H and the nearly spherical behavior of CCl_3H and CBr_3H. In order to determine if this is a result of an intrinsic difference in reactivity between CF_3H and the heavier haloforms, or a consequence of CF_3H being better oriented we compare the orientation distributions for the molecules.

Rather than being perfectly oriented, the molecules are distributed in an array of quantum states, each molecule having $\langle\cos\theta\rangle < 0$. The probability of the molecular axis being oriented within a narrow angular range is given by[32-34]

$$P(\cos\theta) = \sum_{J} \sum_{K=-J}^{J} \sum_{M=-J}^{J} P_{JKM}(\cos\theta) f_{JK}(T) F_{JKM}(V) \qquad (3)$$

which is the overall sum of the quantum probability distribution function, $P_{JKM}(\cos\theta)$, weighted by $f_{JK}(T)$, the fraction of molecules in states J, K at temperature T, and weighted by $F_{JKM}(V)$, the probability of being transmitted through the field at voltage V.

Reproduced with permission of the copyright owner. Further reproduction prohibited without permission.

The distribution calculated from Eq 3 accounts for molecules in states with $\langle\cos\theta\rangle < 0$ being focussed, for those in states with $\langle\cos\theta\rangle > 0$ being defocused, and for those in states with $\langle\cos\theta\rangle = 0$ being unaffected but in divergent trajectories. The distribution for a random beam, $P(\cos\theta) = 0.5$, is subtracted to give $P(\cos\theta)$ appropriate for $\Delta S_{\pm}$. Fig 5 shows the normalized difference distribution for $\Delta S_{\pm}$. Well-oriented molecules ($\langle\cos\theta\rangle \approx -1$) are enhanced and poorly oriented molecules ($\langle\cos\theta\rangle \approx +1$) are diminished in comparison to a randomly oriented sample (dotted horizontal line in Fig 5). The probability distributions are well fit by a truncated expansion in Legendre polynomials[33],

$$P(\cos\theta) = \sum_{i=0}^{3} a_i P_i(\cos\theta) \tag{4}$$

and these coefficients are given in Table IIFig 5 shows that the haloforms are oriented, that they are much better oriented than CH_3Br, and that the orientation distributions for the haloforms are qualitatively similar. But CF_3H is *not* as well oriented as CCl_3H or CBr_3H, even though Fig 2 shows that the steric asymmetry is much larger for CF_3H. We are thus forced to conclude that the intrinsic steric asymmetry for CF_3H is much larger than that for either CCl_3H or CBr_3H.

Reproduced with permission of the copyright owner. Further reproduction prohibited without permission.

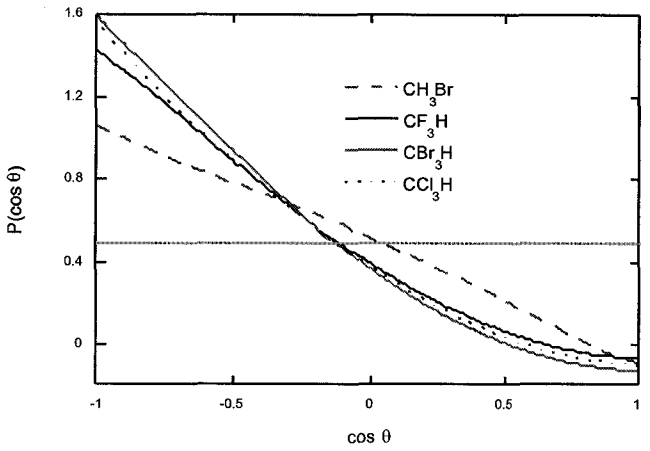

Fig 5. Calculated HV_{on} - HV_{off} probability distributions for CF_3H, CCl_3H and CBr_3H. The CH_3Br distribution is shown for comparison. The dotted horizontal line is obtained for a random sample. The HV_{on} - HV_{off} difference characterizes a sample richer in "correctly" oriented molecules (those with $\langle\cos\theta\rangle \approx -1$) and poorer in "wrongly" oriented molecules.

Table II
Legendre Coefficients for P(cos θ)

	a_1	a_2	a_3
CF_3H	-0.796	0.197	0.041
CCl_3H	-0.846	0.232	0.016
CBr_3H	-0.902	0.246	0.038
CH_3Br	-0.578	-0.034	-0.006
t-C_4H_9Br	-0.641	0.027	0.011

Models. Previous experiments[24,28] on CH_3Br and t-C_4H_9Br showed trends in the steric asymmetry similar to that shown here for CF_3H. That data could be represented by a model in which reaction occurred via two competing mechanisms, one at low energy favoring CH_3-end approach, and the other at higher energy favoring Br-end approach. A similar model fits the steric asymmetry of Fig 2. For energies greater than a high threshold, E_H the orientation-dependent cross section, $\sigma_{\pm}^{H}$ is (in relative units),

$$\sigma_{\pm}^{H} = 0 \qquad E \leq E_H$$

Reproduced with permission of the copyright owner. Further reproduction prohibited without permission.

$$\sigma_{\pm}^{H} = a_{\pm}^{H}(\mathrm{E} - \mathrm{E_H}) + b_{\pm}^{H}(\mathrm{E} - \mathrm{E_H})^2 \qquad E > E_H \tag{5}$$

The low energy cross section is assumed to have the same form with a lower threshold, E_L, but attenuated exponentially with constant c as a consequence of the opening of the higher energy channel,

$$\begin{aligned} \sigma_{\pm}^{L} &= 0 && E \le E_L \\ \sigma_{\pm}^{L} &= a_{\pm}^{L}(E - E_L) + b_{\pm}^{L}(E - E_L)^2 && E_H > E > E_L \\ \sigma_{\pm}^{L} &= \left(a_{\pm}^{L}(E - E_L) + b_{\pm}^{L}(E - E_L)^2\right) e^{-c(E - E_H)} && E > E_H \end{aligned} \tag{6}$$

where $a_{\pm}^{H}$ and $b_{\pm}^{H}$ are adjustable parameters for the positive and negative attack orientations, The overall cross section is $\sigma_{\pm} = \sigma_{\pm}^{L} + \sigma_{\pm}^{H}$.

The parameters shown in Table III have been chosen on a trial-and-error basis to fit the steric asymmetry shown in Fig 2, and show that a reasonable model can fit the CF_3H steric asymmetry. Although these parameters are too numerous to fit, we note that they also fit the *separate* measurements of positive-end and negative-end reactivity from which *G* is derived. Fig 6 shows $R_{\pm}(E)$, the ratio of signals in a specific (±) orientation divided by the signal from random molecules, $S_{\pm}(E,0)$. The model comparison is $\sigma_{\pm}/(\sigma_{+} + \sigma_{-})$ scaled vertically at *one* point to fit the experimental data since the random orientation is not modelled but is present experimentally. This agreement provides reasonable confirmation of the model and fit for CF_3H.

The asymmetry for CBr_3H in Fig 2 shows a small minimum near 15 eV. This minimum is probably due to a competition between reaction channels which both favor attack at the CBr_3 end, but this can not be confirmed by the present data.

Reproduced with permission of the copyright owner. Further reproduction prohibited without permission.

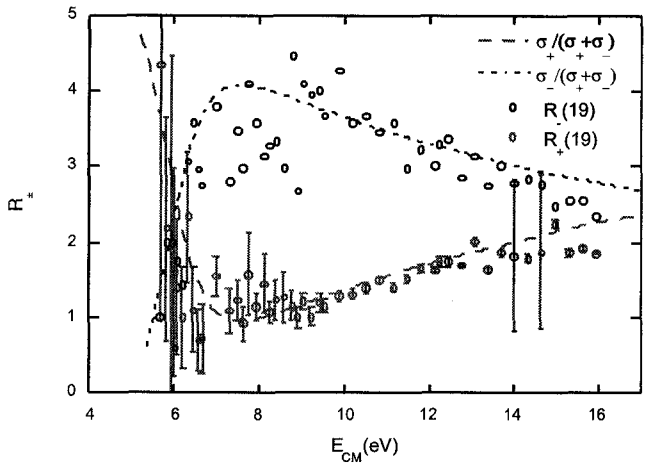

Fig 6. Experimental values of $R_{\pm}(E)$ for F^- ions from CF_3H compared with model fits using the parameters found by fitting the steric asymmetry, G. All experimental error bars are shown for positive end attack although some are smaller that the symbols. Error bars are comparable for negative end attack but are omitted for clarity.

Table III. Model Cross Section Parameters
E is measured in eV; others are (eV)-1 or (eV)-2 to make σ dimensionless

	Br (t-C_4H_9Br)[24]	CF_3H	CCl_3H	CBr_3H
E_H	4.35	5.2	3.0	11
E_L	4.05	4.05	1.5	1.5
a_-^H	250	2000	70	2.7
b_-^H	27	5	20	7
a_+^H	40	40	40	2.6
b_+^H	40	150	18	4
a_-^L	100	100	100	28
b_-^L	100	100	100	.05
a_+^L	1500	1500	1500	20
b_+^L	2000	2000	2000	0.8
c	5	2.2	3	0.01

Discussion

Orbital Differences. The data shown in Fig 2 demonstrate that there is an enormous steric effect for CF_3H. Attacking the positive end produces more F^- just above the ion production threshold, and this preference rapidly shifts to the negative end as the energy increases. On the other hand, the steric asymmetry for CCl_3H and CBr_3H is almost

Reproduced with permission of the copyright owner. Further reproduction prohibited without permission.

negligible. Any hindering effect of the hydrogen atom would be expected to be about equally effective in each of the haloforms, and hindrance cannot account for the H end reactivity in CF_3H. Clearly, factors other than shielding by the H atom are important here, and we believe that the electronic structure of the molecule plays a prominent role.

Fluoroform is known to be qualitatively different from the heavier haloforms. Although the CH bond is generally stronger than the CX bond, the opposite is true in CF_3H where the dissociation energy[30] of the CF bond is 4.8-5.4 eV compared to 4.67 for the CH bond. The optical spectra of fluoroform differs from that of the other haloforms in that the lower energy Rydberg transitions appear to originate from alkyl group orbitals rather than from the halogen lone pairs[35]. The HOMO in CF_3H is largely the σ_{CH} orbital[36], and the lowest lying σ* orbitals are largely centered on the C atom[29].

The steric data of Fig 2 and Fig 6 are fit reasonably well by the model suggesting that low energy reaction occurs mainly at the H end of the molecule. This channel is attenuated in favor of a more likely channel opening at higher energy but favoring the CF_3 end of the molecule. Similar, but less pronounced, behavior was previously observed for electron transfer to CH_3Br and t-C_4H_9Br[24,28] where it was suggested that the electron could be transferred into different orbitals of the molecule depending on the orientation and energy. Near the threshold for ion pair formation only the LUMO is energetically accessible, but higher-lying orbitals could become accessible as the energy is increased.

Thus for CF_3H at energies near threshold an electron will enter the LUMO which is most likely a σ^*_{CH} orbital with lobes extending in both directions along the C-H bond. The electron could be transferred into the LUMO at either lobe, to form a molecular

Reproduced with permission of the copyright owner. Further reproduction prohibited without permission.

negative ion with a charge distribution only partially described as σ^*_{CH}. The haloform negative molecular ions probably distribute the charge over the molecule in a state with σ^*_{CH} as well as σ^*_{CX} character. If a *free* electron were attached, the attachment process would be so rapid that the molecular ion would be formed in the geometry of the neutral. In contrast, transfer of a *bound* electron from a nearby atom introduces the possibility that the atomic ion could perturb the system during the process. Some aspect of the molecular geometry might change but a negative molecular ion is probably still born in the geometry close to that of the neutral. Since the stable negative molecular ion would be expected to have elongated C-F bonds, the incipient ion formed here is most likely born with compressed C-F bonds. The compressed negative molecular ion is thus likely to dissociate to give an F^- ion.

The K^+ and F^- ions will be easier to separate if they are far apart, suggesting that observation of the charges will be facilitated by attack of the σ^*_{CH} lobe at the H end of the molecule. This could produce the incipient charges as far apart as possible. On the other hand, attack at the σ^*_{CH} lobe inside the CF_3 umbrella would leave the incipient charges close to one another, making it difficult to separate the charges at the very lowest energies, and the more likely result would be the formation of the salt KF. Since we only detect ions, formation of salt molecules would be interpreted as a diminished reactivity. Transfer into the σ^*_{CH} lobe inside the umbrella becomes more likely to produce ions as the energy is raised. Also at higher energies the C-F $\sigma*$ orbitals become accessible[37], and since there are three such orbitals, transfer into these orbitals could be almost orientation-independent and the cross section would be much larger. The outcome of an

Reproduced with permission of the copyright owner. Further reproduction prohibited without permission.

electron transfer collision thus depends not only on the energy and the accessibility of an unoccupied orbital, but also on the relative proximity of the reagents.

For the heavier haloforms, exemplified by CCl_3H, the LUMO[38] is σ^*_{CX} and electron transfer is more likely to occur to a peripheral σ^*_{CX} lobe rather than at the σ^*_{CH} lobe as in CF_3H. Thus the cross section would be expected to be larger than that for CF_3H and the steric asymmetry smaller, as is observed. At energies near threshold, electron transfer to the σ^*_{CX} orbital located on one X atom would probably produce the salt KX and this was detected in earlier experiments[39] on CCl_3H where the energy was too low to produce ions. The intensity and angular distribution of the salt product was independent of orientation, showing that there was no steric asymmetry. In order to produce the ions observed in the present experiments, it may be that the electron is transferred to a σ^*_{CX} orbital located on one X atom, followed by near-instantaneous rearrangement of the charge distribution to producing X^- at a more distant X atom. The separation of charges would facilitate their escape as ions.

The σ^*_{CH} orbital in CF_3H manifests itself in yet another way. In addition to the large difference in steric asymmetry between CF_3H and the heavier haloforms, as shown in Fig 2, there is also a major difference in the fragmentation pattern as suggested in Fig 1. This difference is shown in detail in Fig 7, where we plot the fraction of CX_3^- ions vs energy above the X^- threshold. Fluoroform is nearly two orders of magnitude more likely to produce CX_3^- than is either of the other two molecules. The electron fraction is similar and shown in Fig 8. Again this fraction is about two orders of magnitude larger in fluoroform. As previously discussed, an electron entering the σ^*_{CH} orbital would form a temporary negative molecular ion in a geometry close to that of the neutral. Even though

Reproduced with permission of the copyright owner. Further reproduction prohibited without permission.

the most likely result is breaking a C-X bond, the CH bond could also break, or the electron could be ejected. Thus a competition arises between autodetaching the electron, and breaking either the C-F or C-H bond, and all of these processes occur in CF_3H. If the C-H bond were tempted to break the electron is more likely to be given to the CF_3 moiety, and CF_3^- ions are more likely to be formed if the alkali ion is far away at the H end of the molecule, as shown in Fig 3. Likewise, formation of the free electron is favored by attack at the CF_3 end. In the heavier haloforms the electron apparently does not enter the σ^*_{CH} orbital, the H end is not reactive, and according to the above mechanism doesn't produce either CX_3^- or electrons. Instead the electron likely enters the σ^*_{CX} orbital and the C-X bond breaks giving an X^- as the main product. In CBr_3H fission of the C-Br bond may also produce CBr_2H^- as shown in Fig 1.

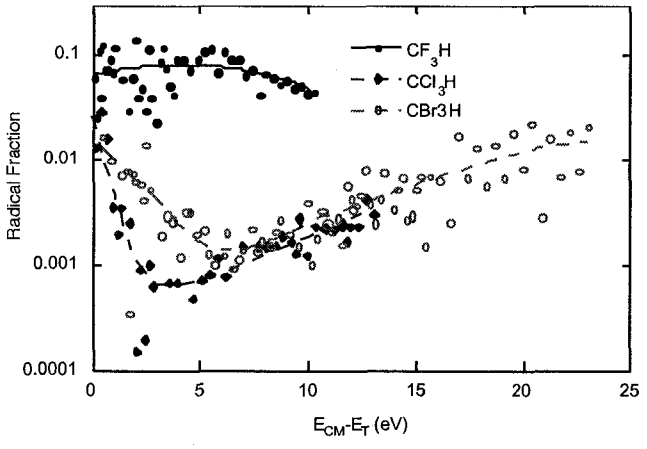

Fig 7. Fraction of signal due to CX_3^- ions for various haloforms as a function of energy above threshold for X^- formation. The curves are to guide the eye.

Reproduced with permission of the copyright owner. Further reproduction prohibited without permission.

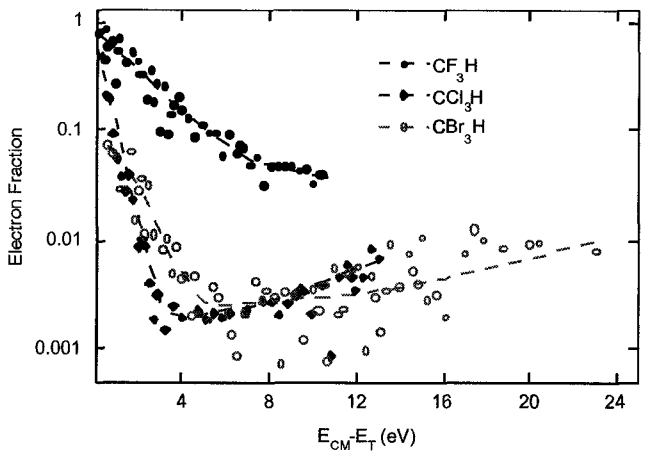

Fig 8. Fraction of electrons as a function of energy above threshold for X^- formation. The curves are to guide the eye.

Models and Steric Factors. The complex steric asymmetry shown in Fig 2 defies a simple interpretation with a customary cone-of-reactivity model. But it is instructive to focus on the high-energy portion of the steric asymmetry where this model might apply. If reaction probability is one for approach within a cone of angle χ_0 and zero otherwise[24], the calculated probability distributions of Fig 5 may be used to extract experimental estimates of χ_0.[3,4,24] For CF_3H near 8 eV this angle is near 120° and increases towards 180° as the energy is increased.

If χ_0 known, the reaction model may be convoluted with the uniform probability distribution for a randomly oriented sample to give the gas phase steric factor, ρ. This is the fraction of gas phase collisions that have enough energy to react. As expected, the steric factors for CBr_3H and CCl_3H are nearly one, but those for CF_3H are noticeably lower than one. The minimum steric factor for CF_3H is ≈ 0.7 which is similar to that for t-C_4H_9Br. (The steric asymmetry is larger for CF_3H but it arises from a better oriented ensemble of molecules.) At high energies the steric factors have an Arrhenius-type of energy dependence as shown in Fig 9. The apparent steric "activation energies" are 7.5

Reproduced with permission of the copyright owner. Further reproduction prohibited without permission.

and 0.5 eV for CF_3H and CCl_3H respectively, which can be compared to 2.2 and 3.9 eV for CH_3Br and t-C_4H_9Br.[24]

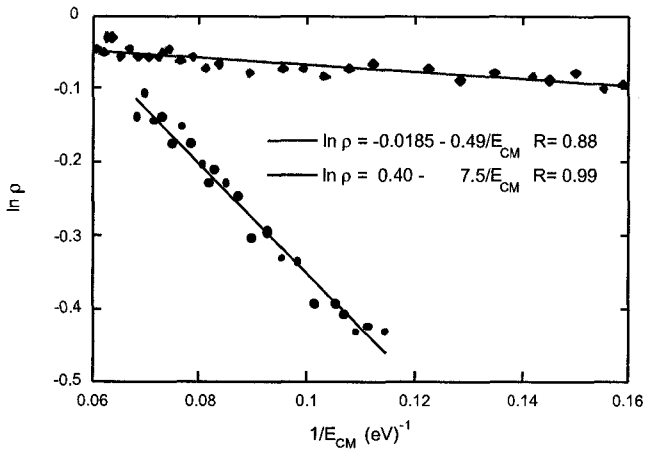

Fig 9. Arrhenius plot for the steric factor.

Summary

Electron transfer from K atoms to CF_3H, CCl_3H and CBr_3H molecules oriented in space produce mainly the X^- halide ion and K^+. The steric asymmetry for CCl_3H and CBr_3H is small as expected, and more X^- is produced by negative end attack. Contrary to expectations, the steric asymmetry of CF_3H is large and changes with energy: at energies near the threshold for ion formation the H end of the molecule is more reactive to form F^- and this preference shifts to the CF_3 end as the energy is increased.

The large differences between CF_3H and the two heavier haloforms is apparently a signature of different low lying σ* orbitals. The preference for H end attack in CF_3H apparently arises from a low lying σ^* orbital centered on the C or the CH bond, whereas the LUMO in the heavier haloforms is believed to be σ^*_{CX} resulting in almost no steric preference. Occupation of the σ^*_{CH} orbital in CF_3H is apparently responsible for the

Reproduced with permission of the copyright owner. Further reproduction prohibited without permission.

formation of significantly more CF_3^- ions and free electrons than for the heavier haloforms.

Once the electron is transferred, the products formed, either ions or salt, depend on the proximity of the reactants as well as the energy. Formation of ions at very low energies is favored by "backside" attack where the incipient ions could be formed as far apart as possible. Close proximity favors salt formation which probably explains the lack of ion-pair formation for attack inside the CF_3 umbrella.

Classical steric factors, ρ, based on a cone-of acceptance model are calculated from the experimental data and the theoretical distribution of orientations. The steric factors are close to one, and for CF_3H the minimum ρ is ~ 0.7. At the higher energies the steric "activation energies" for CF_3H and CCl_3H are ~ 7.5 and 0.5 eV.

Acknowledgements

We gratefully acknowledge support for this research that has been received from the National Science Foundation and from the Robert A. Welch Foundation. R. F. M. L. thanks the ICCTI-Portugal for a sabbatical grant.

1)Loesch, H. J. *Annu. Rev. Phys. Chem* **1995**, *46*, 555-94.

2)Parker, D. H.; Bernstein, R. B. *Ann. Rev. Phys. Chem* **1989**, *40*, 561-595.

3)Brooks, P. R. *Intl. Review of Phys.Chem* **1995**, ***14***, 327-354.

4)Brooks, P. R.; Harland, P. W. *Effect of Molecular Orientation on Electron Transfer and Electron Impact Ionization*; Adams, N. G. and Babcock, L. M., Ed.; JAI Press: Greenwich, CT, 1996; Vol. 2, pp 1-39.

Reproduced with permission of the copyright owner. Further reproduction prohibited without permission.

22)Townes, C. H.; Schawlow, A. L. *Microwave Spectroscopy*; Dover: New York, 1975.

23)Brooks, P. R.; Jones, E. M.; Smith, K. *J. Chem. Phys.* **1969**, *51*, 3073.

24)Brooks, P. R.; Harris, S. A. *J. Chem. Phys.* **2002**, *117*, 4220-32.

25)Wiley, W. C.; McLaren, I. H. *Rev. Sci. Instr.* **1955**, *26*, 1150.

26)Lias, S. G.; Bartmess, J. E.; Liebman, J. F.; Holmes, J. L.; Levin, R. D.; Mallard, W. G. *J. Phys. Chem. Ref. Data* **1988**, *17*, Supplement 1.

27)Deyerl, H. J.; Alconcel, L. S.; Continetti, R. E. *J. Phys. Chem* **2001**, *105*, 552-7.

28)Harris, S. A.; Brooks, P. R. *J. Chem. Phys.* **2001**, ***114***, 10569-72.

29)Modelli, A.; Scagnolari, F.; Distefano, G.; Jones, D.; Guerra, M. *J. Chem. Phys.* **1992**, *96*, 2061-70.

30)Kerr, J. A.; Stocker, D. W. *Handbook of Chemisty and Physics*; CRC Press:, 2000.

31)Xing, G.; Kasai, T.; Brooks, P. R. *J.Am.Chem.Soc.* **1995**, *117*, 2581-2589.

32)Stolte, S. *Ber. Bunsenges.Phys.Chem* **1982**, *86*, 413-421.

33)Stolte, S.; Chakravorty, K. K.; Bernstein, R. B.; Parker, D. H. *Chem Phys* **1982**, *71*, 353-361.

34)Choi, S. E.; Bernstein, R. B. *J. Chem. Phys.* **1986**, *85*, 150-161.

35)Robin, M. B. *Higher Excited States of Polyatomic Molecules*; Academic Press: New York, 1974; Vol. I.

36)Brundle, C. R.; Robin, M. B.; Basch, H. *J. Chem. Phys.* **1970**, *53*, 2196-2213.

37)Varella, M. T. N.; Winstead, C.; McKoy, V.; Kitajima, M.; Tanaka, H. *Phys. Rev. A* **2002**, *65*, 22702-18.

38)Ying, J. F.; Leung, K. T. *Phys. Rev. A* **1996**, *53*, 1476-86.

39)Marcelin, G.; Brooks, P. R. *J. Am. Chem. Soc.* **1973**, *95*, 7885-6.

Reproduced with permission of the copyright owner. Further reproduction prohibited without permission.

References

ABU 67 N. Abuaf, J.B. Anderson, R.P. Andres, J.B. Fenn, and D.G.H. Marsden, *Science* **155**, 997 (1967).

ALC 69 J. Alcalay and E. Knuth, *Rev. Sci. Instrum.* **40**, 438 (1969).

ALL 89 M. Allan, *J. Electron Spectrosc.*, **48**, 219 (1989).

ATE 75 J. Aten and J. Los, *J. Phys. E: Sci. Instrum.* **8,** 408 (1975).

BEV 03 P. Bevington, *Data Reduction and Error Analysis for the Physical Sciences*, 3rd edition, 161 (2003).

BRO 96 P. R. Brooks and P. W. Harland, in *Advances in Gas Phase Ion Chemistry*, edited by N. G. Adams and L. M. Babcock (JAI, Greenwich, CT, 1996), Vol. 2, pp. 1–39.

COM 78 R. Compton, P. Reinhardt and C. Cooper, *J. Chem. Phys.*, **68**, 4360 (1978).

CUR 99 L.A. Curtiss, P.C. Redfern, K. Raghavachari, V. Rassolov and J.A. Pople, *J. Chem. Phys.* **110,** 4703 (1999).

DAT 61 S. Datz, D. Herschbach and E. Taylor, *J. Chem. Phys.* **35**, 1549 (1961).

DIS 77 H. Dispert and K. Lacmann, *Chem. Phys. Lett.*, **47**, 533 (1977).

ERV 92 K. Ervin and W. Lineberger, *Advances in Gas Phase Ion Chemistry*, J AI Press: Greenwich, CT, Vol **1** (1992).

FRI 91 B. Friedrich and D. R. Herschbach, *Z. Phys. D: At., Mol. Clusters* **18**, 153 (1991).

GIS 79 E. Gislason, *Alkali Halide Vapours* ed P. Davidovits and D. McFadden, New York: Academic, p 415 (1979).

GIS 81 E. Gislason, A. Kleyn and J. Los *Chem. Phys.* **59,** 91 (1981).

GOO 73 J. Goodisman, *Diatomic Interaction Potential Theory*, Vol. 1, Academic Press, 1973.

HAR 57 R. Hart, E. Gray and W. Guier, *Phys. Rev.* **108**, 1512 (1957).

Reproduced with permission of the copyright owner. Further reproduction prohibited without permission.

HARL 72 P. Harland. and J. Thynne, *Int. J. Mass Spectrom. Ion Phys.* **9**, 253 (1972).

HARL 03 P. Harland and P. Brooks, *J. Am. Chem. Soc.* **125**, 13191 (2003).

HER 66 D.R. Herschbach, *Adv. Chem. Phys.* **10**, 319 (1966).

HIR 90 K. Hiraoka, S. Mizuse, S. Yamabe, *J. Phys. Chem.* **94,** 3689 (1990).

HUB 79 K. Huber and G. Herzberg, *Molecular Spectra and Molecular Strucure. IV. Constants of Diatomic Molecules* Van Nostrand Reinhold Company: New York, 1979.

KAN 51 A. Kantrowitz and J. Grey, *Rev. Sci. Instrum.* **22**, 328 (1951).

KIN 97 R. King, N. Pettigrew, and H. Schaefer. *J. Chem. Phys.* **107**, 8536 (1997).

LAN 66 J. Langer, S. Matejcik and E. Illenberger, *Intl. J. Mass Spect.* **220**, 211 (2002).

LAR 74 R. Larson, S. Neoh and D. Herschbach, *Rev. Sci. Instrum.* **45**, 1511 (1974).

LEO 85 D. Leopold, K. Murray, A. Stevens Miller and W. Lineberger, *J. Chem. Phys.* **83**, 4849 (1985).

LIF 73 C. Lifshitz, T. Tiernan and B. Hughes, *J. Chem. Phys.* **59**, 3182 (1973).

LOE 90 H. J. Loesch and A. Remscheid, *J. Chem. Phys.* **93**, 4779 (1990).

LOE 95 H. J. Loesch, *Annu. Rev. Phys. Chem.* **46**, 555 (1995).

LOU 03 Yu-Ran Luo, *Handbook of Bond Dissociation Energies in Organic Compounds*, CRC Press, 2003.

MAM 73 B. Mamyrin, V. Karatajev, D. Schmikk, V. Zagulin, *Sov. Phys. JETP* **37**, 45 (1973).

MAS 76 H. Massey, *Negative Ions*, Cambridge, NY, 1976.

MCM 82 D. McMillen and D. Golden, *Annu. Rev. Phys. Chem.* **33**, 493 (1982).

MIL 04 T. Miller, J. Van Doren and A. Viggiano, *Int. J. Mass Spectrom.* **233**, 67 (2004).

MOU 87 A. Moutinho, M. Maneira, A. Praxedes and R. Lobo *Rev. Port. Qu´ımica* **29,** (1987).

Reproduced with permission of the copyright owner. Further reproduction prohibited without permission.

NIK 68 E. Nikitin, *Chemische Elementarprozesse* ed Hartmann (Berlin: Springer) p 43 (1968).

NIS 03 *NIST Chemistry WebBook, NIST Standard Reference Database Number 69*; Linstrom, P. J.; Mallard, W. G., Eds.; National Institute of Standards and Technology: Gaithersburg MD, 20899, 2003.

OST 89 T. Oster, A. K hn and E. Illinberger, *Int. J. Mass Spectrom. Ion Processes*, **89**, 1 (1989).

PAR 89 D. H. Parker and R. B. Bernstein, *Annu. Rev. Phys. Chem.* **40**, 561 (1989).

PAU 00 H. Pauly, *Atom, Molecule, and Cluster Beam*, Vol. 1, Springer, 2000.

REC 77 G. Reck, B. Mathur and E. Rothe, *J. Chem. Phys.*, **66**, 3847 (1977).

SHC 83 L.N. Shchegoleva, I.I. Bilkis and P.V. Schastnev, *Chem. Phys.* **82**, 343 (1983).

SMA 77 R. Smalley, L. Wharton and D. Levy, *Spectroscopy with Supersonic Jets*, Vol **10**, 139, 1977.

SMA 75 R. Smalley, L. Wharton and D. Levy, *J. Chem. Phys.*, **63**, 4977 (1975).

SNA 81 D. Snavely, S. Colson and K. Wiberg, *J. Chem. Phys.*, **74**, 4977 (1981).

SUL 76 S. Sullivan and J. Beauchamp, *J. Am. Chem. Soc.* **98**, 1160 (1976).

TAN 76 S. Tang, B. Mathur, E. Rothe and G. Reck, *J. Chem. Phys.* **64**, 1270 (1976).

VON 29 J. von Neumann and E. Wigner, *Phys. Z.* **30**, 467 (1929).

WEL 80 G. Wells, G. Reck and E. Rothe, *J. Chem. Phys.*, **73**, 1280 (1980).

WIG 48 E. Wigner, *Phys. Rev.* **73**, 1002 (1948).

WIL 55 W. Wiley and I. McLaren, *Rev. Sci. Instrum.* **26**, 1150 (1955).

YOU 73 W. Young, *Rev. Sci. Instrum.* **44**, 715 (1973).

Reproduced with permission of the copyright owner. Further reproduction prohibited without permission.